



Physik-Institut der Universität Zürich

# Mie resonance spectroscopy of single levitated particle

Master's Thesis at University of Zürich in Physics departement

by Yiea-Funk Te

Supervision:

Prof. Andreas Schilling, Institute of Physics, University of Zürich  
Prof. Thomas Peter, Institute for Atmospheric and Climate Science, ETH Zürich  
Dr. Ulrich Krieger, Institute for Atmospheric and Climate Science, ETH Zürich

September 2011



# Contents

<b>Contents</b>	<b>2</b>
<b>Abstract</b>	<b>4</b>
<b>1 Introduction</b>	<b>5</b>
1.1 Aerosols: Overview and atmospheric implications . . . . .	5
1.2 Glassy aerosols and their atmospheric implications . . . . .	5
1.3 Preliminary results . . . . .	7
1.4 Aim of this work . . . . .	10
<b>2 Theoretical background</b>	<b>11</b>
2.1 Glass formation . . . . .	11
2.1.1 Thermodynamic considerations . . . . .	11
2.1.2 Viscosity and relaxation time . . . . .	12
2.2 Mie Scattering . . . . .	13
2.2.1 Mie theory . . . . .	14
2.2.2 Polarisation of the scattered light . . . . .	16
2.2.3 Angular distribution of the scattered light . . . . .	17
2.2.4 Morphology dependent resonances . . . . .	17
<b>3 Electrodynamic Balance (EDB)</b>	<b>21</b>
3.1 Experimental setup . . . . .	21
3.1.1 Particle injection . . . . .	22
3.1.2 Electrodynamic trapping . . . . .	23
3.1.3 Cooling system . . . . .	24
3.1.4 Gas phase regulation . . . . .	26
3.1.5 Relative humidity measurement . . . . .	28
3.2 Experimental methods . . . . .	30
3.2.1 $U_{DC}$ mass determination . . . . .	30
3.2.2 Radius determination by Mie phase function analysis . . . . .	30
3.2.3 Liquid-solid phase identification by analysing the Light-scattering intensity fluctuations . . . . .	31

3.2.4	White light Mie resonance spectroscopy . . . . .	32
3.3	High resolution Mie resonance spectroscopy . . . . .	33
3.3.1	TDL Mie resonance spectrum . . . . .	35
<b>4</b>	<b>Michelson interferometer (MI)</b>	<b>39</b>
4.1	Theoretical Background of the Michelson Interferometer . . . . .	39
4.1.1	Basic concept of an interferometer . . . . .	39
4.1.2	Principle of Michelson interferometer . . . . .	40
4.2	Experimental setup . . . . .	42
4.2.1	Design and operational principle of MI . . . . .	42
4.2.2	Design of the detectors . . . . .	45
4.3	Characteristics of the Michelson Interferometer . . . . .	47
4.3.1	Wavelength determination . . . . .	48
4.3.2	Accuracy and precision . . . . .	49
4.3.2.1	Rubidium Spectroscopy . . . . .	49
4.3.2.2	Accuracy and precision determination: results . . . . .	51
4.3.3	Analysis of Tunable Diode Laser wavelength measurements at dif- ferent scan-speeds . . . . .	54
4.3.3.1	Fringe formation depending on the directional motion of the cart . . . . .	54
4.3.3.2	Analysis of $\Delta$ <i>fringes</i> at different cart speeds and TDL scan speeds . . . . .	57
<b>5</b>	<b>Glassy sucrose experiment</b>	<b>59</b>
5.1	Preparation . . . . .	60
5.2	LED spectra analysis . . . . .	62
5.3	TDL spectra analysis . . . . .	67
5.4	Summary of the sucrose experiment . . . . .	71
<b>6</b>	<b>Conclusions and outlook</b>	<b>73</b>
<b>7</b>	<b>Acknowledgements</b>	<b>74</b>
	<b>Bibliography</b>	<b>75</b>

## Abstract

Atmospheric aerosols are suspensions of small solid and/or liquid particles in air with a negligible terminal fall speed. They often consist of water, an inorganic and an organic fraction. The abundance of these constituents in aerosol particles depends on the geographic location, altitude and time. Depending on their concentration and composition, they affect different atmospheric properties and processes, such as atmospheric chemistry and Earth's radiative budget [1]. Tropospheric aerosol particles are of particular importance due to its impact on cloud formation, atmospheric chemistry and atmospheric radiation budget [2]. Despite its importance for the climate the physical state of tropospheric aerosol particles still remains ambiguous. Our gap in the understanding of the physical state arises primarily from the large organic fraction, whose individual chemical species remain mostly unidentified.

In a previous study, Zobrist *et al.* have developed and corroborated the scientific hypothesis that aerosol particles with large organic fraction and medium to large molecular weight tend to form glasses at low relative humidities at room temperatures, or up to high relative humidities at upper tropospheric temperatures [1]. Subsequently, Zobrist *et al.* investigated the impedance of water uptake of model aerosol particles (binary sucrose/water system) over the whole tropospheric temperature range. From these experiments a new parameterization of  $D_{H_2O}$ , the translational diffusion coefficient of water molecules, could be derived. The new parameterization can be applied to simulate the water uptake of atmospheric aerosols, with possible implications on ice nucleation [3]. From these experiments it can be shown that sucrose particles under upper tropospheric conditions need more than a day to liquefy when initially in the glassy state and therefore they are not expected to participate in relevant atmospheric processes such as water uptake, ice nucleation and heterogeneous chemistry. Under strongly non-equilibrium conditions the concentration (and therefore the refractive index) within the particle is expected to be radial inhomogeneous, leading to a particle with a core-shell structure, i.e. with a shell of high water concentration compared to the core of mainly pure sucrose upon humidification. However, direct experimental evidence for these radial diffusion profiles are still missing. High resolution Mie resonance spectroscopy may offer a way to detect the core-shell structure unambiguously.

Experiments on single micrometer-sized aqueous sucrose particles were performed in an electrodynamic balance (EDB), in which levitated micrometer-sized droplets can be stored without wall contact over days in a controlled humidity and temperature environment [4]. Optical techniques were employed to follow the minute changes of the particle's size. To obtain a deeper understanding of such microparticle in glassy state, several improvements of the current EDB are necessary, which is the main part of this master thesis. Therefore, a new method to characterize a particle is developed based on Mie resonance spectroscopy with high resolution. For this purpose a Michelson interferometer based wavemeter is built and its characteristics are analysed. Furthermore, first measurements with glassy sucrose particle are presented to demonstrate the benefits of the improved setup of the EDB.

# 1 Introduction

## 1.1 Aerosols: Overview and atmospheric implications

Atmospheric aerosols are suspensions of small solid and/or liquid particles in air with a negligible terminal fall speed. Their size varies between few nano- and micrometers. Primary aerosol particles are of biological (seeds, pollen, spores, bacteria, algae, fungi and viruses), geological (mineral dust, sea salt particles from bubble bursting and volcano particles) and anthropogenic origin (road and industrial dust, wind erosion of tilled land, biomass burning, fuel combustion). Secondary aerosol particles are formed from condensation of gas phase molecules. Thus, the composition of atmospheric aerosols depends on their origin, the diffusion of molecules into particles from the gas phase and internal transformations [5].

Aerosols affect different atmospheric properties and processes, such as atmospheric chemistry and Earth's radiative budget. For example, the aerosol climate forcing can be divided into a direct and an indirect aerosol effect [6], which is illustrated in Fig. 1. The direct aerosol effect is due to scattering and absorption of sunlight by aerosols, and it depends on aerosol properties such as physical state, size, absorption cross section and chemical composition. Depending on ambient relative humidity, aerosol particles grow or shrink by taking up or releasing water vapor thus enhancing or reducing the scattering intensity of the aerosol [7]. In the aerosol indirect effect, the presence of particles alters cloud properties and behaviour. Due to the availability of anthropogenic aerosols, the cloud droplet number concentration (CDNC) increases, which leads to a higher cloud albedo (see Fig. 1; cloud albedo effect). Subsequently the cloud droplets are smaller, causing suppressed rain formation, drizzle formation and increased liquid water content (LWC) in the atmosphere. The clouds thus reside longer and higher in the atmosphere (see Fig. 1; cloud lifetime effect). In the semi-direct effect, the absorption of shortwave radiation by aerosols heats the troposphere, which may influence the relative humidity, the stability and thereby again cloud formation lifetime [8].

Besides the above mentioned effects, aerosols play an important role in heterogeneous and multiphase chemistry [9]. The particles provide surface and liquid phase for reactions which are kinetically hindered in the pure gas phase [10]. Furthermore, atmospheric aerosols play a central role in the health effects of air pollution. They are associated with lung cancer, asthma and cardiovascular disease [11].

## 1.2 Glassy aerosols and their atmospheric implications

A detailed explanation of glass formation can be found in section "3.1 Glass formation". In general, glasses are disordered amorphous (non-crystalline) substances that behave mechanically like solids. Glasses are ubiquitous in nature and are widely applied in bioengineering, food technology, pharmaceutical industries or cryobiology [13]. They are formed when a liquid is cooled without crystallization until the viscosity increases

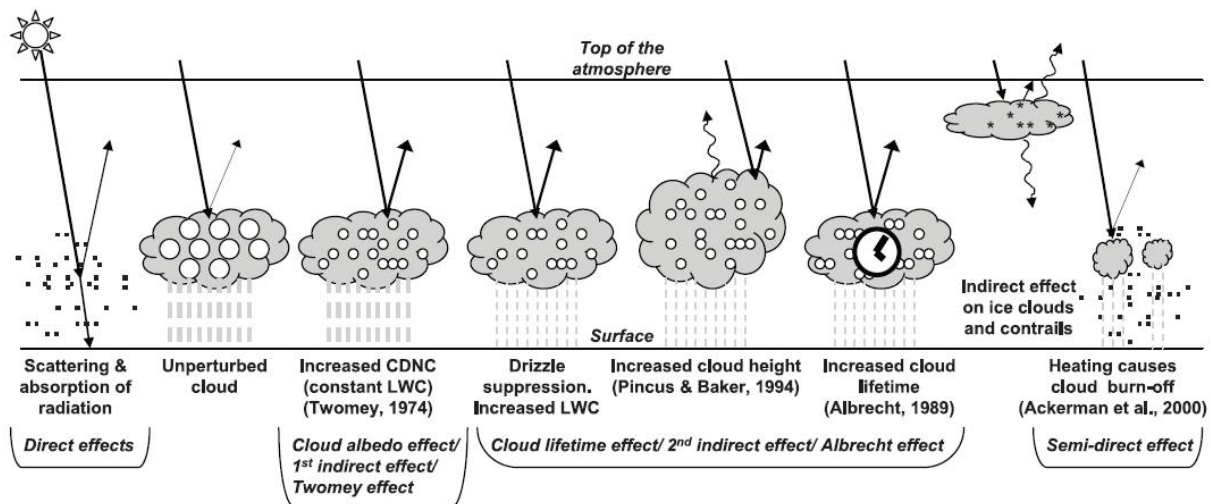


Figure 1: Overview of direct and indirect aerosol effects. The small black dots represent aerosol particles, the larger open circles represent cloud droplets. Straight lines represent the incident and reflected solar radiation, and waved lines represent terrestrial radiation. The filled white circles indicate cloud droplet number concentration (CDNC). Unperturbed clouds contain larger cloud drops as only natural aerosols are available. Perturbed clouds contain a greater number of smaller cloud droplets since both natural and anthropogenic aerosols are available as cloud condensation nuclei (CCN). The vertical grey dashes represent rainfalls, and LWC refers to liquid water content [12].

exponentially. When the viscosity of such a glassy particle reaches a value in the order of  $10^{12}$  Pa s, the molecular motion becomes so slow, that it vitrifies within few seconds to minutes at the glass transition temperature  $T_g$  [14].

The ability to form a glass depends strongly on the chemical and physical properties of a given substance and its mixing state [15]. Marcolli *et al.* (2004) found that an assemblage of a large number of components is prone to adapt liquid or amorphous state even in absence of a solvent (usually water) [16]. This means that the melting temperature  $T_m$  of a mixture decreases with increasing number of components. Crystallization is suppressed in such liquids as the continuation of the formation of the crystal structure is interrupted by a lack of appropriate molecules. In addition, Marcolli *et al.* specified the liquid as the thermodynamically stable state the more components the mixture consists of, valid for both organic and inorganic salts [16]. This means that particles, which consist of many different chemical substances, tends to form a solution. The discovery of Marcolli *et al.* (2004) make the formation of glassy aerosols accessible, since particles emitted in a wood burning site might indeed contain a large number of components. Thus, aerosol particles would preferentially be liquid. When reaching higher altitudes, glass formation might occur at sufficiently low temperatures.

If aerosol particles were really present as glasses, this would influence several physical and

chemical processes in the atmosphere significantly. In highly viscous or glassy aerosol particles, chemical reactions are impeded in viscous solutions, thereby leading to an extended aerosol lifetime with respect to chemical decomposition. The slow molecular diffusion of water within glassy aerosol particle can drastically retard or even entirely prevent water uptake from the gas phase and inhibit ice nucleation and ice growth. Water uptake by an aerosol increases its scattering intensity and, hence, affects climate forcing by the direct aerosol effect. Moreover, water uptake is an essential process that precedes and accompanies cloud formation and may therefore also influence cloud properties and occurrences. Therefore, it is essential to study the formation of glassy organic substances to improve our understanding of ice cloud formation and upper tropospheric humidity.

### 1.3 Preliminary results

Previous experiments performed by Zobrist *et al.* (2011) showed, that organic aerosol particles upon drying may transform into a glassy state, and this transition may cause water uptake of these particle to be impeded or completely inhibited, in particular under upper tropospheric conditions [3]. For highly viscous liquids or glasses, the diffusion to the particle is not limited by the gas-phase diffusion since it always exceeds liquid-phase diffusion. Therefore, the liquid phase diffusion coefficient  $D_{liq}$  is of particular interest for modeling the water uptake of highly viscous particles. Furthermore, gaining knowledge of  $D_{liq}$  might aid in optimizing spray-drying and freeze-drying technology and allows calculating the growth of ice particles which might help to avoid mechanical rupture of cellmembranes in cryo-storage.

Recently, experiments on aqueous sucrose particles were performed as a good representative of the water-soluble organic fraction in the atmosphere since sucrose is a component of biomass burning aerosols [3]. Single micrometre-sized aqueous sucrose particles were stored contact-free in an electrodynamic balance (see section "4.1 Electrodynamic Balance (EDB)") under temperature and humidity control for several days.

The diffusion of water molecules within the sucrose droplet is modelled by using the spherical non-linear diffusion equation:

$$\frac{\partial n}{\partial t} = \nabla(D_{H_2O}\nabla n) = \frac{1}{r^2} \frac{\partial}{\partial r} \left( r^2 D_{H_2O} \frac{\partial n}{\partial r} \right) \quad (1)$$

where  $n$  is the number density of water molecules in the particle,  $t$  is time and  $r$  is the distance from the particle's centre (*i.e.*,  $r \leq R_p$ , particle radius). The  $n$ -dependence of  $D_{H_2O}$  transforms eqn (1) into a non-linear diffusion problem. This leads to steep diffusion "fronts" or "waves" instead of creeping diffusion tails [17].

In order to model numerically the highly non-linear diffusion process, a spherical shell diffusion model is developed. The diffusion coefficient  $D_{H_2O}$  depends both on temperature and composition. Water-activity is used to describe the composition dependence

and the temperature dependence is parameterized with an expression of the form of the Vogel-Fulcher-Tammann equation [14, 18]. Thus,  $D_{H_2O}$  is parameterized as [3]:

$$\log_{10}[D_{H_2O}(T, a_w)] = - \left( A(a_w + \frac{B(a_w)}{T - T_0(a_w)}) \right) \quad (2)$$

$A$ ,  $B$  and  $T_0$  are fit functions that all depend on the water activity of the aqueous sucrose solution. The numerical model treats the particle as consisting of up to several thousand individual shells and simulates the growth or shrinkage of the particle resulting from water diffusion between the shells.

As mentioned above, Zobrist *et al.* (2011) performed experiments using an aqueous sucrose particle levitated in a electrodynamic balance. Fig. 2 shows experimental data of a sucrose particle that was investigated for 9 days at 291 K. Fig. 2a and 2b shows the relative humidity (RH) and the particle's radius as a function of time (coloured solid lines). As the relative humidity increases (decreases), the particle's radius increases (decreases) as well due to water uptake (water release). The black dashed line in Fig. 2b shows the calculated radius for particle in thermodynamic equilibrium with the surrounding humidity. However, the observed radius remains systematically larger than the calculated equilibrium radius in all humidifying cycles, indicating that the particle retains more water than expected under equilibrium conditions. As the RH is kept constant at 2% RH for a long time, the deviation becomes smaller, indicating a slow continued release of water from the particle. However, equilibrium was rapidly established when RH was increased again to about 63% RH in the last humidifying cycle. These measurements indicate that the release and uptake of water by particle is controlled by water diffusion within the particle at lower RH, which corresponds to larger sucrose concentrations. This concludes that the diffusion coefficient of water molecules  $D_{H_2O}$  is a function of the concentration of water molecules in the droplet. This can be more clearly seen in Fig. 2c, where the radius is plotted *versus* RH. A readily equilibrating particle exposed to changing RH would follow the black dashed line. This is only achieved for RH larger than about 40% in this experiment at 291 K and  $RH/t \approx 0.05\% \text{ min}^{-1}$  (marked by the dark grey area in Fig. 2c). At low RH all data in humidifying cycles remain below the equilibrium curve (dashed black line) indicating retarded water uptake into the particle, while in drying cycles all data remain above the equilibrium line indicating retarded water release. The particle is assumed to be in a non-equilibrium state (light grey area in Fig. 2c) as it approaches the glassy state below 31% RH at 291 K. The experimental radius data (coloured solid lines in Fig. 2b) can be accurately modelled (red dotted line in Fig. 2b) by using the liquid-phase diffusion model. Fig. 2d shows the modelled radial concentration profile of the particle as a function of time. One can see time periods of non-equilibrium conditions (concentration gradients with sloping blue and green contour lines, *e.g.* at  $1 \times 10^5$  s and  $3 \times 10^5$  s) and periods of equilibrium conditions within the particle (even concentration throughout the particle with vertical yellow and red contour lines, *e.g.* at  $2.2 \times 10^5$  s and  $6.5 \times 10^5$  s). Time periods of non-equilibrium conditions corresponds to a particle with radial inhomogeneous composition and periods of equilibrium conditions to a homogeneous particle.

The experiments by Zobrist *et al.* (2011) conclude that the concentration (and therefore the refractive index) within the sucrose particle under non-equilibrium conditions (*e.g.* upper tropospheric conditions) is expected to be radial inhomogeneous. However, direct experimental evidence for these radial diffusion profiles are missing.

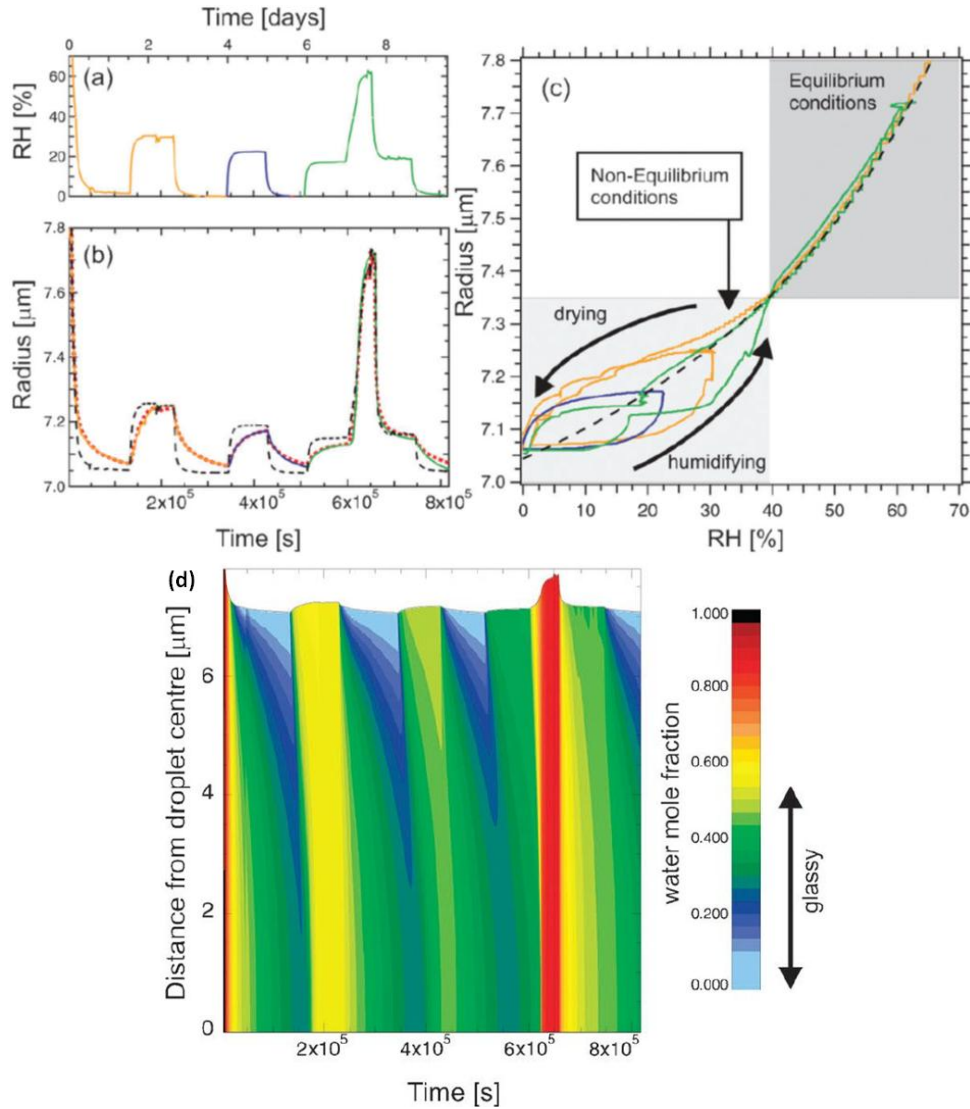


Figure 2: Panels (a) and (b) show the chamber relative humidity (RH) and the particle's radius as a function of time (coloured solid lines). The dashed black line in (b) and (c) shows the calculated radius for a particle in thermodynamic equilibrium with the surrounding humidity. The red dotted line in (b) shows the calculated radius using eqn (2). Panel (d) shows the particle concentration profile as a function of time calculated with the liquid-phase diffusion model.

## 1.4 Aim of this work

As mentioned above, experiments performed by Zobrist *et al.* (2011) lead to the assumption that sucrose particle under non-equilibrium conditions might be radial inhomogeneous [3]. However, direct experimental evidence are still missing. High resolution Mie resonance spectroscopy should allow determining the particle's radius and refractive index with high precision (see section "3.3 Mie Scattering" for a detailed explanation). Furthermore, it should be possible to detect the expected core-shell structure unambiguously.

The main focus of this thesis is to upgrade the present setup of the EDB to perform Mie resonance spectroscopy with higher resolution. Therefore a high resolution Tunable Diode Laser (TDL) (New Focus High-Power 6300 Velocity Tunable Diode Laser, model 6308, tuning range: 765 nm - 781 nm) is used instead of a conventional broadband light source - spectrograph combination to perform Mie resonance spectroscopy with high resolution. In principle, the narrowest resonance peaks should be observable by using the TDL (which is not possible with LED). In order to assign the measured resonance peaks to wavelength and compare them to Mie calculations, a Michelson interferometer based wavemeter is built to determine the wavelength of the TDL with a precision better than 0.05 nm [19]. This increases the resolution of the current setup by a factor 10. Furthermore, Rubidium spectroscopy is performed to test the accuracy of the Michelson interferometer wavemeter [20].

A critical component for successful analysis of the EDB data is the measurement of relative humidity (RH). Up to now, a capacitive thin film relative humidity sensor (MiniCap 2, Panametrics, USA) is used. The sensor is calibrated directly in the EDB using the deliquescence relative humidity of different salts. It shows significant hysteresis at high RH which becomes worse with decreasing temperature. Therefore a capacitance RH sensor with superior design (Type G-TUS.13, UPSI, France) showing significantly lower hysteresis, faster time response and superior performance at higher humidity and lower temperatures will be tested. This sensor is intended to be incorporated in addition to Minicap 2 into the present setup. Several calibration experiments with different salts such as sodium chloride are performed. With the new sensor G-TUS 13, the accuracy of the RH determination is increased, which is a crucial component of EDB experiments.

The Michelson interferometer, the TDL and the new humidity sensor are integrated into the EDB setup. Furthermore as the second part of this thesis, first experiments on glassy sucrose particle are performed to demonstrate the benefit of the newly upgraded setup. By using high resolution Mie resonance spectroscopy, first experimental data of sucrose particles under atmospheric conditions are provided for further study of the core-shell structure of sucrose particles.

## 2 Theoretical background

### 2.1 Glass formation

#### 2.1.1 Thermodynamic considerations

Glasses are amorphous, supercooled liquids with respect to the crystalline state. In contrast to crystallization, vitrification or glass formation is a continuous process since it is not associated with heat uptake, heat release or volume discontinuities.

Fig. 3 depicts schematically the entropy  $S$  change (Fig. 3a) and isobaric heat capacity  $c_p$  change (Fig. 3b) as a function of temperature for a liquid-to-solid phase transition and a glass transition. The correlation between  $S$  and  $c_p$  can be derived via the enthalpy  $H$  for a closed system [21]:

$$c_p = \left( \frac{\partial H}{\partial T} \right)_{p,N} = T \cdot \left( \frac{\partial S}{\partial T} \right)_{p,N} \quad (3)$$

The entropy  $S$  is given by the Boltzmann formula

$$S = k_B \cdot \ln \Omega \quad (4)$$

where  $k_B$  is the Boltzmann constant and  $\Omega$  is the number of quantum states corresponding to a given energy, volume and mass. The entropy  $S$  can be split into distributions of different kind of entropies such as the vibrational  $S^{vib}$ , rotational  $S^{rot}$ , translational  $S^{trans}$  and configurational  $S^{conf}$  entropy. Therefore, eqn (4) can be written as [22]:

$$S = k_B \cdot \ln \Omega^{vib} + k_B \cdot \ln \Omega^{rot} + k_B \cdot \ln \Omega^{trans} + k_B \cdot \ln \Omega^{conf} + \dots \quad (5)$$

As shown in Fig. 3a, cooling a stable liquid results in a decrease in entropy  $S$  (light blue line). The liquid may crystallize when it reaches  $T_m$ . However, this is an idealized case, since crystallization is kinetically hindered and requires a nucleation process. Therefore, the liquid enters the supercooled range (dark blue line), in which the liquid is not in the thermodynamically preferred state. In this case,  $S$  decreases continuously even below  $T_m$ . In such a supercooled (metastable) liquid nucleation can occur at any given moment, in which case  $S$  would drop abruptly to their crystal values at the nucleation temperature. This is associated with an instantaneous loss of  $S^{rot}$ ,  $S^{trans}$  and  $S^{conf}$ . Therefore, eqn (3) implies that  $c_p$  nominally becomes infinite at crystallization temperature  $T_{cry}$  (see Fig. 3b). The remaining entropy of the crystal is approximately equal to its vibrational entropy [23],

$$S \approx k_B \cdot \ln \Omega^{vib} \quad (6)$$

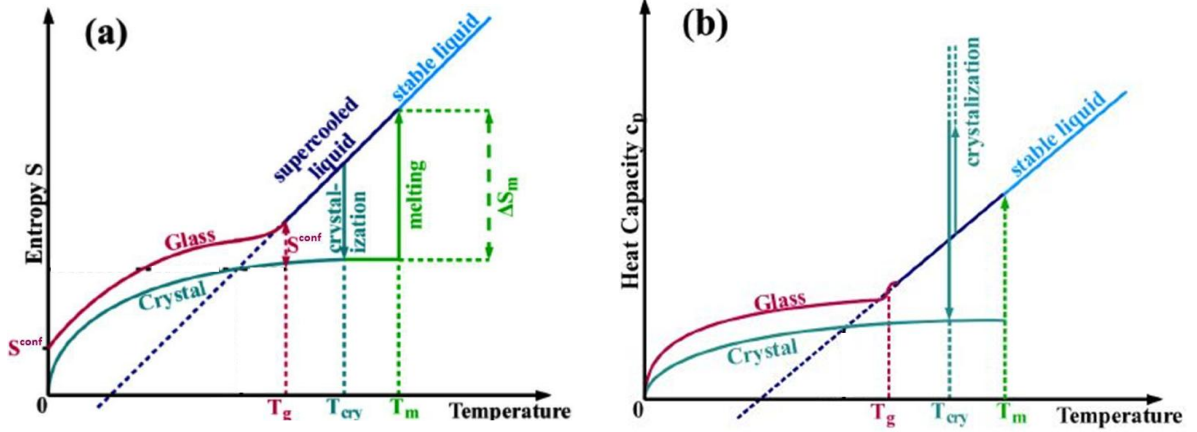


Figure 3: Thermodynamic representation of crystallization and glass transition showing the (a) Entropy  $S$  and the (b) isobaric heat capacity  $c_p$  versus temperature [1, 14].

which vanishes as the temperature approaches 0 K. According to eqn (3),  $c_p$  also decreases to zero (see Fig. 3b).

Besides crystallization, the liquid can convert to the glass phase at glass temperature  $T_g$ . In this phase, the liquid is in a non-crystalline amorphous state that behaves mechanically like a solid [14]. Since the viscosity increases exponentially upon cooling, molecular diffusion is practically ceased (see section "3.1.2 Viscosity and relaxation time"). But in contrast to a crystal, a glass can not adapt a long range order during the glass formation process. Because translational and rotational degrees of freedom are frozen on experimental timescales below  $T_g$ , the entropy in the glassy state  $S^g$  decreases upon cooling with a slope similar to that of the crystal. However, the entropy of a glass  $S^g$  has still a configurational part:

$$S^g = S^{vib} + S^{conf} \quad (7)$$

Therefore, it exceeds the one of a crystal by  $S^{conf}$  (see Fig. 3a). As a glass does not adapt other configurations in experimentally realistic timescales,  $S^{conf}$  stays constant until 0 K. Consequently, the isobaric heat capacity of a glass  $c_p^g$  exceeds the one of a crystal  $c_p^{cry}$  (see Fig. 3b). Eqn (3) implies that both  $c_p^g$  and  $c_p^{cry}$  vanish when temperature approaches 0 K. As the glass transition is not associated with a sudden release of entropy,  $c_p^g$  smoothly adapts to lower value of the glass. However, the slope of  $c_p$  is different at  $T_g$  and indicative of the glass transition.

### 2.1.2 Viscosity and relaxation time

Viscosity  $\eta$  is a measure of the resistance of a fluid which is being deformed by either shear or tensile stress. The viscosity can be described by the Vogel-Tamman-Fulcher (VTF) equation [5]:

$$\eta = \eta_{T\infty} \cdot \exp\left(\frac{D \cdot T_0}{T - T_0}\right) \quad (8)$$

where  $\eta_{T\infty}$  denotes the viscosity at  $T \gg T_g$ ,  $D$  and  $T_0$  are temperature-independent constants. The viscosity can be turned into relaxation time  $\tau$  by using the Maxwell relation [18]:

$$\eta = G_\infty \cdot \tau, \quad (9)$$

where  $G_\infty$  is the instantaneous shear modulus. When a liquid is cooled rapidly from a temperature above the glass transition to the region below the glass transition, it retains some properties of the higher temperature, and those properties “relax” to those characteristic of the lower temperature as a function of time. This period of time is characterized by the relaxation time  $\tau$ .

Adam and Gibbs (1965) described the relaxation time in terms of cooperative rearrangements of the melt in mutually independent regions. Their minimum size is given by

$$z^* = N_A \cdot s^{conf} / S^{conf}, \quad (10)$$

which decreases with increasing temperature.  $s^{conf}$  is the configurational entropy of the subsystem in consideration and  $N_A$  the Avocadro constant. The probability  $\omega$  of these rearrangements is derived as

$$\omega = \omega_{T\infty} \cdot \exp\left(\frac{-z^* \cdot \Delta\mu}{k_B \cdot T}\right), \quad (11)$$

where  $\Delta\mu$  is the potential energy hindering the cooperative rearrangement per monomer and independent of  $T$  and  $z^*$ .  $\omega_{T\infty}$  is the probability of a rearrangement event at an infinite temperature. Since the relaxation time  $\tau$  is inversely proportional to  $\omega$ ,  $\tau$  can be expressed as an exponential function as well depending on  $z^*$ ,  $\Delta\mu$  and  $T$ :

$$\tau = \tau_{T\infty} \cdot \exp\left(\frac{z^* \cdot \Delta\mu}{k_B \cdot T}\right). \quad (12)$$

With eqn (9) and (10), both the relaxation time  $\tau$  and the viscosity  $\eta$  depend exponentially of the configurational entropy  $s^{conf}$  and temperature  $T$ .

## 2.2 Mie Scattering

It is crucial to study the behaviour of aerosol particles under atmospheric conditions to understand their impact on different atmospheric properties such as atmospheric

chemistry and Earth's radiative budget. Fundamental factors are size and refractive index of an aerosol particle, since a change in composition due to evaporation or absorption of molecules from the ambient can be deduced from these factors. If the aerosol particle is liquid (*i.e.* spherical) and in the micrometer range, the scattered light by this particle contains essential information about the particle. The scattering of light by a spherical particle is described by Mie theory [24]. A short introduction to the Mie theory should show the particular characteristics of the scattered light by a micrometer sized spherical particle. A detailed explanation can be found elsewhere [25].

### 2.2.1 Mie theory

The Mie theory describes the scattering of an electromagnetic wave by a homogeneous sphere of arbitrary radius. Posing the right boundary conditions at the sphere's surface and at infinity, Maxwell's equations can be solved. Using the spherical symmetry of the problem the fields inside and outside the sphere are expanded in spherical harmonics. The fields are expressed as a series of Legendre polynomials and spherical Bessel functions. The scattering properties of the sphere depend on the size of the sphere and the refractive indices of the sphere and the surrounding medium. In a homogeneous medium both  $\vec{E}$  and  $\vec{H}$  satisfy the vector Helmholtz equation:

$$\nabla^2 \vec{\psi} = -k^2 m^2 \vec{\psi} \quad (13)$$

where  $\vec{\psi}$  is a vector function,  $k = 2\pi/\lambda$  is the vacuum wavenumber and  $m$  is the (complex) refractive index of the medium.

Posing the right boundary conditions one obtains the solution for an incoming plane wave being scattered by a sphere of radius  $r$  and (complex) refractive index  $m$ . The following boundary conditions apply at the surface of the sphere:

$$\vec{n} \times (\vec{E}_2 - \vec{E}_1) = \vec{0} \quad (14)$$

$$\vec{n} \times (\vec{H}_2 - \vec{H}_1) = \vec{0} \quad (15)$$

where the subscript 1 denotes the sphere and 2 the surrounding medium and  $\vec{n}$  is the unit vector normal to the surface of the sphere. Eqn (14) and (15) demand that the tangential component of the field at the surface of the sphere is continuous. In addition the field at infinity needs to go to zero. By solving eqn (13) in spherical coordinates and posing these boundary conditions the fields far from the sphere can be derived as:

$$E_\theta^{sca} = H_\phi^{sca} = \frac{-i}{kr} e^{-im_0kr+i\omega t} \cos(\phi) S_2(\theta) \quad (16)$$

$$-E_\phi^{sca} = H_\theta^{sca} = \frac{-i}{kr} e^{-im_0kr+i\omega t} \sin(\phi) S_1(\theta) \quad (17)$$

$$E_r^{sca} = H_r^{sca} = 0 \quad (18)$$

with  $S_1(\theta)$  and  $S_2(\theta)$  being the scattering amplitude functions:

$$S_1(\theta) = \sum_{n=1}^{\infty} \frac{2n+1}{n(n+1)} [a_n \pi_n(\cos\theta) + b_n \tau_n(\cos\theta)] \quad (19)$$

$$S_2(\theta) = \sum_{n=1}^{\infty} \frac{2n+1}{n(n+1)} [b_n \pi_n(\cos\theta) + a_n \tau_n(\cos\theta)] \quad (20)$$

where  $n$  is the mode number.

The angle dependent functions  $\pi_n$  and  $\tau_n$  are functions of the  $P_n^l$  Legendre polynomials:

$$\pi_n(\cos\theta) = \frac{1}{\sin\theta} P_n^l(\cos\theta) \quad (21)$$

$$\tau_n(\cos\theta) = \frac{d}{d\theta} P_n^l(\cos\theta) \quad (22)$$

The coefficients  $a_n$  and  $b_n$  are the scattering coefficients:

$$a_n = \frac{\psi_n(x)\psi_n'(mx) - m\psi_n(mx)\psi_n'(x)}{\zeta_n(x)\psi_n'(mx) - m\psi_n(mx)\zeta_n'(x)} \quad (23)$$

$$b_n = \frac{m\psi_n(x)\psi_n'(mx) - \psi_n(mx)\psi_n'(x)}{m\zeta_n(x)\psi_n'(mx) - \psi_n(mx)\zeta_n'(x)} \quad (24)$$

$\psi_n$  and  $\zeta_n$  in eqn (23) and (24) are the Ricatti Bessel functions defined as

$$\psi_n(x) = \sqrt{\frac{\pi x}{2}} I_{n+1/2}(x) \quad (25)$$

$$\zeta_n(x) = \sqrt{\frac{\pi x}{2}} H_{n+1/2}^{(2)}(x) \quad (26)$$

where  $I_{n+1/2}(x)$  is the Bessel function and  $H_{n+1/2}^{(2)}(x)$  the Hankel function.

The prime in eqn (23) and (24) denotes differentiation with respect to the argument.  $m$  is the (complex) refractive index and  $x$  the so-called Mie parameter which solely depends on the wavelength  $\lambda$  of the scattered light and the diameter  $d$  of the particle:

$$x = \frac{\pi d}{\lambda} \quad (27)$$

As one can see, the scattering coefficients  $a_n$  and  $b_n$  of a spherical particle can be unambiguously described by the refractive index  $m$  and Mie parameter  $x$ . This concludes that by observing the scattered light from a spherical particle, it is possible to obtain informations about the size and refractive index by comparing the measured scattered light with Mie calculations. This will be discussed in the subsequent sections.

If the scattered light is measured at a fixed angle (*i.e.*  $\phi$  and  $\theta$  fixed), it is possible to obtain informations about size and refractive index by comparing the measured scattered light with Mie calculations.

### 2.2.2 Polarisation of the scattered light

The direction of the incoming light and the scatter direction defines the scattering plane. The polarisation of the scattered light is referred to the scattering plane. Therefore, the incoming ( $E^{inc}$ ) and the scattered wave ( $E^{sca}$ ) can be splitted into a parallel ( $\parallel$ ) and a perpendicular ( $\perp$ ) polarized part. This is schematically illustrated in Fig. 4

The relation between the polarisation of the scattered wave and the incoming wave is described by the so-called T-Matrix [26]:

$$\begin{pmatrix} E_{\parallel}^{sca} \\ E_{\perp}^{sca} \end{pmatrix} = \frac{i \exp(-ikr)}{kr} \begin{pmatrix} S_2(\theta) & 0 \\ 0 & S_1(\theta) \end{pmatrix} \begin{pmatrix} E_{\parallel}^{inc} \\ E_{\perp}^{inc} \end{pmatrix} \quad (28)$$

Since the T-Matrix is diagonal, absolute parallel ( $E_{\perp}^{inc} = 0$ ) or perpendicular ( $E_{\parallel}^{inc} = 0$ ) polarized incoming wave will not be depolarized after scattering. In any other cases, the polarisation can be changed since  $S_1(\theta) \neq S_2(\theta)$ .

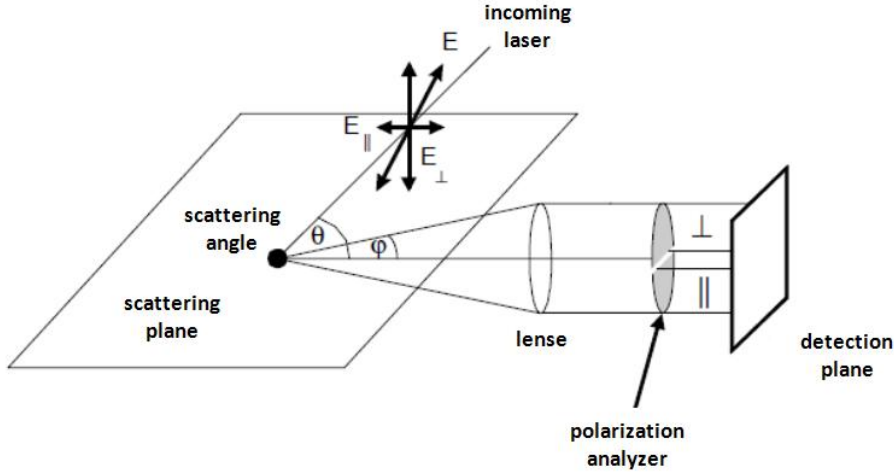


Figure 4: Schematic representation of the scattering geometry: The scattering plane is defined by the directions of the incoming light and the detection of the scattered light. The electric field vector  $E$  is split into its parallel ( $E_{\parallel}$ ) and its perpendicular ( $E_{\perp}$ ) component with respect to the scattering plane.

### 2.2.3 Angular distribution of the scattered light

By using eqn (19), (20) and (28), the angular distribution of the scattered light in the scattering plane (*i.e.*  $\phi = \theta$ ) can be calculated as a function of the scattering angle  $\theta$ . Fig. 5 shows the angular distribution of the scattered light for  $\theta = 0...360^\circ$  for three different Mie parameter in a logarithmic scale.  $\theta = 0^\circ$  corresponds to forward scattering and  $\theta = 180^\circ$  to backward scattering. Using light of wavelength with  $\lambda = 514.5$  nm,  $x = 5$  corresponds to a diameter of the sphere of  $0.82 \mu\text{m}$ ,  $x = 25$  to  $4.09 \mu\text{m}$  and  $x = 100$  to  $16.38 \mu\text{m}$ . For these calculations the refractive index was set to  $m = 1.40$ . Each calculation shows the angular distribution of parallel (grey curve) and perpendicular (black curve) polarized light with respect to the scattering plane.

For very small particles (see example for  $x = 5$ ) where the size of the particle is in the same magnitude of the wavelength of the light, there are only weak modulations of the scattered light, in particular of the parallel polarized component (grey curve). However, the forward scattering is strongly favoured and more than two magnitudes higher than the backward scattering. Such scattering from very small particles is called the Rayleigh limit of the Mie scattering.

Spherical particles with bigger diameter ( $x = 25$  and  $x = 100$ ) show a significant stronger modulated angular distribution of the scattered light. The intensity of the scattered light at  $\theta = 0^\circ$  and  $180^\circ$  are particular high. They are known as the so-called "hot spots" or "glare spots" [27]. As mention above, the angle-dependent modulation of the scattered light is characteristic for the spherical particle and strongly depends on its size and refractive index. Therefore, these parameter can be deduced from measuring the angular distribution of the scattered light. Another way to obtain informations of a spherical particle from the scattered light is to measure the scattered light at a fixed angle (*i.e.*  $\phi$  and  $\theta$  fixed). This possibility will in the next subsection.

### 2.2.4 Morphology dependent resonances

Fig. 6a shows the scattering efficiency  $Q_{sca}$  as a function of the Mie parameter.  $Q_{sca}$  is defined as the ratio of cross section  $C$  and cross sectional area:  $Q = C/\pi a^2$ . For Mie parameter  $x \geq 14$ , one can clearly see small sharp maxima of  $Q_{sca}$  at certain Mie parameter. These sharp maxima occur if the incoming light of a certain wavelength steps into resonance with the spherical cavity of the particle. The part of the incoming light, which hits the spherical particle at very small angle, is trapped near the surface by total internal reflection and travels around the surface of the sphere. After multiple internal reflection, the light beam might hit the starting-point and interfere constructively. This is illustrated in Fig. 6b, where the incoming light hits the particle tangentially. The caused resonances strongly depends on the size and refractive index of the particle. They are known as "morphology dependent resonances" (MDRs).

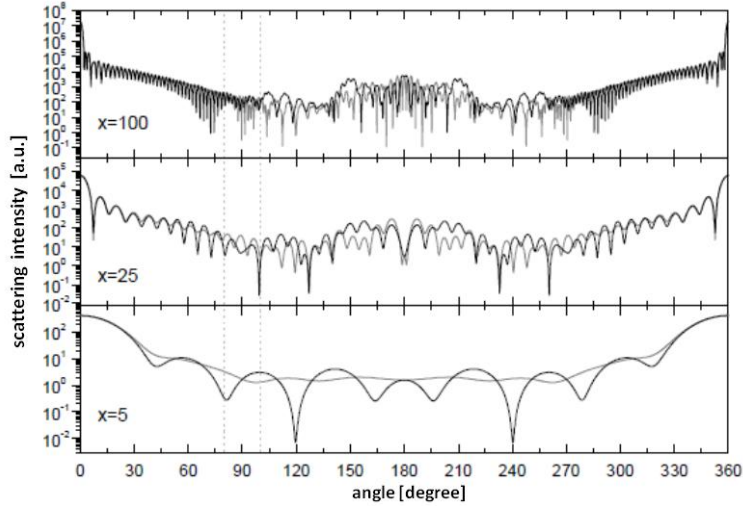


Figure 5: The angular distribution of the scattered light in the scattering plane (*i.e.*  $\phi = 0$ ) for different Mie parameter  $x$  in a logarithmic scale. The refractive index is  $m = 1.40$ . The grey lines show the scattered light with parallel polarization, the black lines with perpendicular polarization [27].

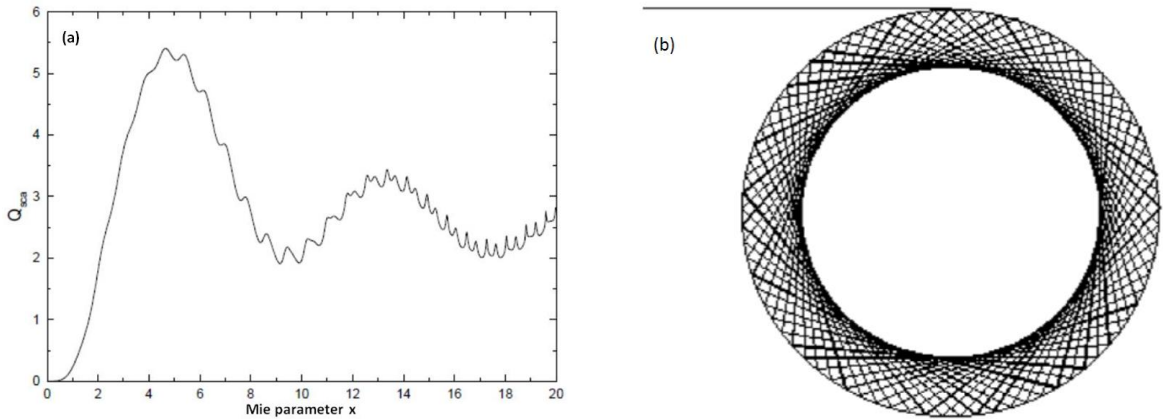


Figure 6: (a) The scattering efficiency  $Q_{sca}$  as a function of the Mie parameter  $x$  (refractive index  $m = 1.40$ ). Small sharp maxima of  $Q_{sca}$  appear for Mie parameter  $x \geq 14$ , known as "morphology dependent resonances" (MDRs). (b) The occurrence of MDRs is illustrated using geometric optics. A light beam hits the spherical particle tangentially and undergoes 400 internal reflections near the surface (refractive index  $m = 1.40$ ) [27].

The MDRs are natural frequencies of the electrical field within the spherical sphere, which acts as a resonator. In Mie theory they formally correspond to the poles of the scattering coefficients  $a_n$  and  $b_n$  (eqn (23) and (24)). The poles appear if the denominator of  $a_n$  and  $b_n$  are equal to zero. The poles of the scattering coefficients always appear in

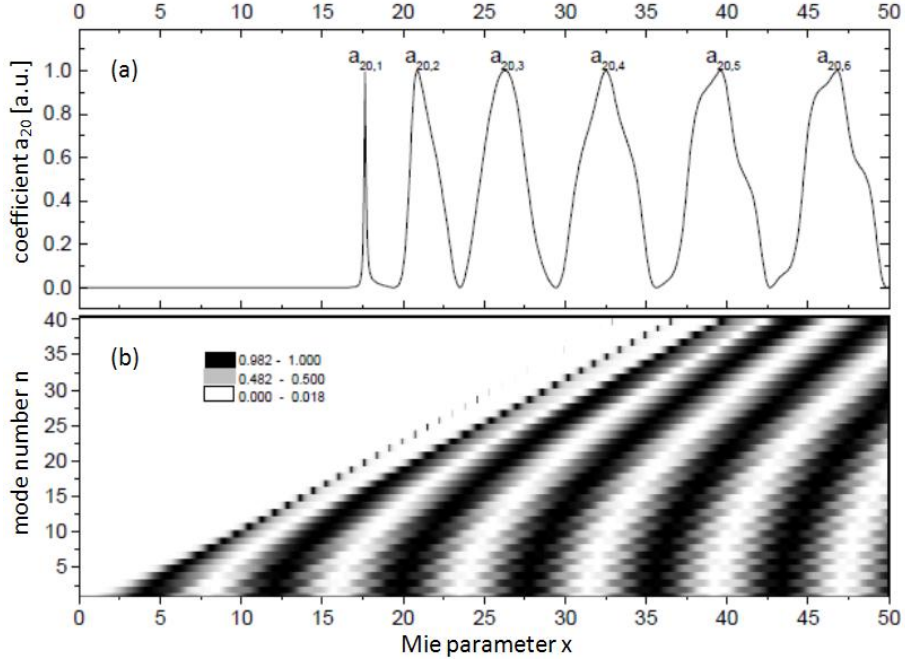


Figure 7: (a) The first six poles (order number  $l = 1..6$ ) of the scattering coefficient  $a_{20}$  are shown as a function of the Mie parameter  $x$ . (b) The coefficients from  $a_1$  to  $a_{40}$  are shown as a function of the Mie parameter  $x$ . The values of  $a_n$  ( $\in [0, 1]$ ) are encoded in different gray tones. White corresponds to the value 0, black to the value 1 [27].

pairs of the order  $\{b_n, a_n\}$ , which is characteristic for MDRs. Furthermore,  $a_n$  and  $b_n$  exhibit an unlimited number of poles. This is illustrated in Fig. 7a, where the scattering coefficient  $a_n$  (with  $n = 20$ ) is plotted *versus* Mie parameter  $x$ . The poles of a certain scattering coefficient are denoted with a second index  $l$  called order number, *i.e.*  $a_{n,l}$ . The maximas corresponding to the poles become broader and the distance between them larger as the order number  $l$  increases. Moreover, the shape of the maximas changes from a simple Lorentz line to a complicated curve. Maximas with a low number of  $l$  are called low-order MRDs and maximas with a high number of  $l$  are called high-order MRDs.

With growing index  $n$ , the first pole ( $l = 1$ ) of each  $n$  appears at increasing Mie parameter  $x$ . This is illustrated in Fig. 7b where the index  $n$  of coefficient  $a_n$  is plotted *versus* Mie parameter  $x$ . For example, Fig. 7a ( $n = 20$ ) corresponds to a horizontal cut through Fig. 7b at  $n = 20$ . The maximas with the same index  $l$  and increasing  $n$  are shifting along the dark traces to bigger Mie parameter  $x$  and become more narrow.

Fig. 8 shows an exemplary Mie resonance spectrum, where the Mie resonance intensities are plotted *versus* Mie parameter  $x$ . The Mie spectrum is calculated with a fixed wavelength  $\lambda = 514.5$  nm and refractive index  $m = 1.40$  for changing diameter  $d$  of the particle. Resonances caused by poles of  $b_{n,l}$  are called TM (transversal magnetic) and by poles of  $a_{n,l}$  are called TE (transversal electric) mode. TE modes have no radial

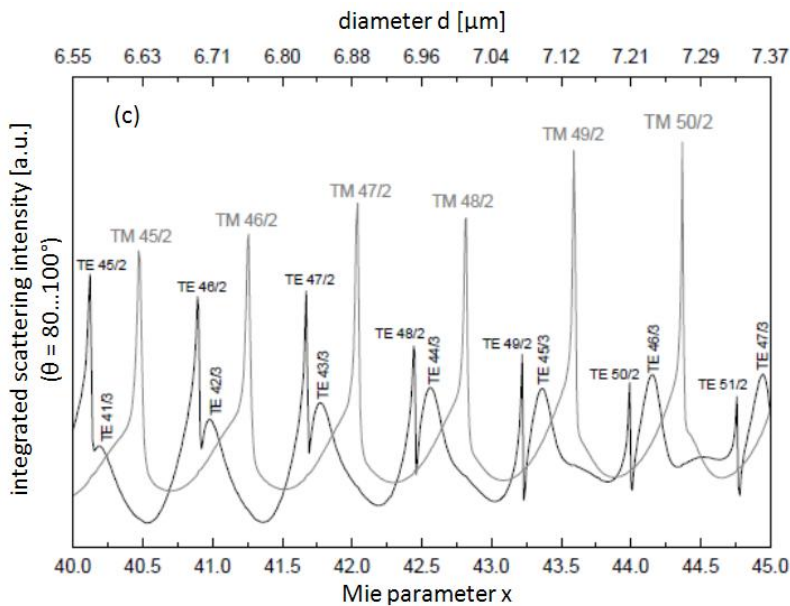


Figure 8: The intensity of MDRs is illustrated as a function of the Mie parameter for a fixed integrated angle  $\theta = 80\dots 100^\circ$  ( $\phi = 0^\circ$ ). The MDRs are calculated with a fixed wavelength  $\lambda = 514.5$  nm and refractive index  $m = 1.40$ . The grey line corresponds to scattered light of parallel polarization, dark line to scattered light of perpendicular polarization [27].

electric component thus, the electric field vector is parallel to the surface of the sphere. TM modes have no radial magnetic field component. This is due to the fact, that one always measures the far field of the scattered light, *i.e.* at distances much bigger than the diameter of the spherical particle. Since the radial component of the electric and magnetic field decreases with  $1/r^2$ , and the component perpendicular to the radial component only with  $1/r$ , one would only measure the transversal component of the electric and magnetic field in the far field [27]. As mention above, the TE and TM modes appear as pairs with the order  $\{\text{TE}, \text{TM}\}$ , respective  $\{a_{n,l}, b_{n,l}\}$ .

As mention above, the characteristics of a spherical particle can be determined by measuring the angular distribution of the scattered light and compare it with Mie calculations. However, measuring the scattered light over a wide range of angle is hard to realize experimentally, for example due to the spatially restriction of a experimental setup such as the electrodynamic balance (EDB). Furthermore, precise measurement and reproducibility of an angle are difficult to achieve. Therefore, the most simple experimental way to determine the characteristics of a spherical particle is to observe the MRDs at a fixed angle of  $\theta$  and  $\phi$  with either variable wavelength  $\lambda$  (by using a tunable laser) or changing diameter  $d$  of the particle. A method to associate the experimental measured resonances with the correct mode number  $n$  and mode order  $l$  is to determine the full width at half maximum (FWHM) of the measured resonances and compare them with the calculated resonances.

### 3 Electrodynamic Balance (EDB)

An electrodynamic balance (EDB) is used for accurate investigations of the microphysical and optical properties of single levitated aerosol particles under atmospheric conditions. A particle of the size between 5 - 30  $\mu\text{m}$  can be trapped in a temperature and humidity controlled chamber over several days to investigate its aggregate state and chemical compound.

This chapter treats the experimental setup of the EDB and the methods to characterize the aerosol. The experimental setup and its special characteristics of the EDB are explained in section "4.1 Experimental setup". Up to now, four independent methods are employed to characterize the aerosol particle in the EDB, which are described in section "4.2 Experimental methods". As a newly built feature and main work of this thesis, a high resolution Tunable Diode Laser is used to perform Mie resonance spectroscopy with high resolution. This method is explained in section "4.3 High resolution Mie spectroscopy".

#### 3.1 Experimental setup

A schematic representation of the EDB is shown in Fig. 9. The EDB is placed in a three wall glass chamber with a cooling agent flowing between the inner walls and the insulation vacuum between the outer walls (see section "4.1.3 Cooling system"). By using a constant AC voltage with accurate frequency control and a regulated DC voltage, an electrically charged particle with radius between 2 - 15  $\mu\text{m}$  (represented as a blue sphere in Fig. 9) is levitated in the EDB chamber. The aerosol particle can be selectively illuminated by a He-Ne laser ( $\lambda = 633 \text{ nm}$ ) or a Ar-Ion laser ( $\lambda = 488 \text{ nm}$ ) with a motorised tiltable mirror. Thereby, the particle can be made visible for two CCD cameras (CCIR TV cameras, FTM 800, Phillips), which are denoted as CCD 1 and CCD 2 in Fig. 9. CCD 1 records the near field video image of the particle to adjust the DC voltage for compensating the gravitational force and to determine the mass change of the particle (see section "4.2 Experimental methods",  $U_{DC}$  mass determination), whereas CCD 2 records the far field scattered light to determine its aggregate state (solid or liquid) and size (see section "4.2 Experimental methods", radius determination by Mie phase function analysis). Furthermore as a newly built feature, the aerosol particle can be illuminated by a high resolution Tunable Diode Laser (New Focus High-Power 6300 Velocity Tunable Diode Laser, model 6308, tuning range: 765 nm - 781 nm) and the scattered light is measured by a photodiode and fed to a computer to obtain Mie resonance spectra with high resolution (see section "4.3 High resolution Mie resonance spectroscopy"). The whole experiment is built on a vibration isolated optical table to provide experiments under stable conditions.

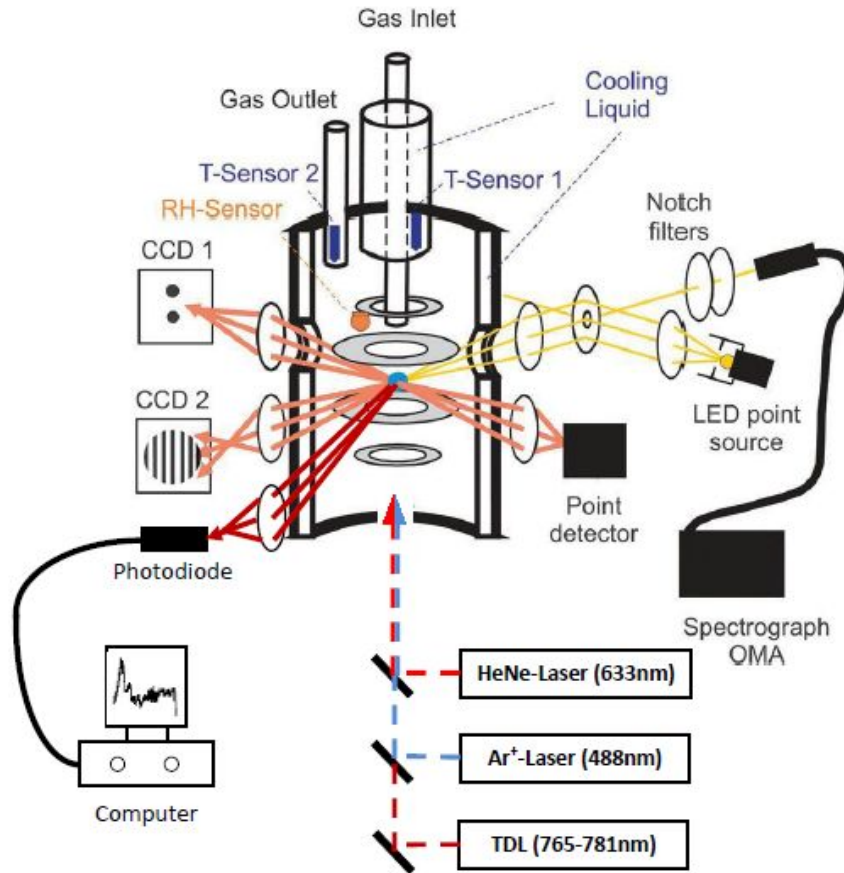


Figure 9: Schematic of the EDB. A three-wall glass chamber hosts four metal rings which supply the electric field needed for particle levitation. The particle is illuminated by two laser beams (488 nm and 633 nm) from below and by the LED from aside. The scattered light is collected in the near and far field by two CCD cameras, and fed to a spectrograph via an optical fiber. Furthermore, the particle is illuminated by a Tunable Diode Laser (765 - 781 nm) and the scattered light is measured by a photodiode and fed to a computer. Two temperature sensors, specified as T-sensors, are located at the gas inlet and outlet tube. The humidity sensor, specified as RH-sensor, is placed in the EDB. [3]

### 3.1.1 Particle injection

A liquid containing particles of interest is produced (solution of typically 5 weight percent) and injected into the EDB with a single particle generator (Hewlett-Packard 51633A ink jet cartridge). The droplets are accelerated into the chamber via short voltage pulses. The droplet is inductively charged as it detaches from the cartridge. To amplify this process, a ring electrode with same AC voltage applied to the electrode rings of the EDB is attached at the outlet of the cartridge. The high voltage ring electrode

causes a spatial separation of the positive and negative charges within the droplet. As the liquid detaches from the outlet of the cartridge either the positive or the negative charges of the droplet remain at the outlet of the cartridge and thus, the droplet is charged.

A droplet typically contain 10 000 charges, which can be positively or negatively charged depending on the sign of the electrical phase of the AC voltage at the detachment process. The injection can be observed with a CCD camera. If a droplet is successfully trapped in the alternating field, the required DC voltage can be applied to keep the particle in a stable levitation (see section "4.1.2 Electrodynamic trapping").

### 3.1.2 Electrodynamic trapping

The principle of the electrodynamic trapping is described in this section. A detailed description can be found in different literatures [28, 29]. The dynamics of a particle with mass  $m$  trapped in an electrodynamic balance is governed by the vectorial equation of motion [30]:

$$m\ddot{\vec{X}} = q\vec{E} - K_d\dot{\vec{X}} + m\vec{g} + \vec{F}_{ext} \quad (29)$$

$\vec{X}$  is the position of the particle with respect to the center of the balance, the double dot indicates the second derivative with respect to time, and the single dot indicates the first derivative. The forces acting on the particle include the electrostatic force  $q\vec{E}$  with particle charge  $q$  and total electrical field strength  $\vec{E} = \vec{E}_{AC} + \vec{E}_{DC}$ , the aerodynamic drag force  $K_d\dot{\vec{X}}$  with the drag coefficient  $K_d$ , gravity  $m\vec{g}$ , and any other external forces  $\vec{F}_{ext}$ , which may include photophoretic, thermophoretic and radiophoretic forces [30]. By solving the equation of motion (29), one obtains the conditions for setting the AC and DC voltage to keep a charged particle in a stable position within a electrodynamic trap.

Fig. 10 shows the trapping of a aerosol in a electromagnetic trap consisting four ring electrodes. The trap used in the current EDB setup is a modification of a classical Paul trap [32] with DC voltage applied to the outer ring electrodes. By applying an AC voltage  $U_{AC}$  to the inner ring electrodes made of stainless steel, an inhomogeneous electric field with a potential minimum  $U_{min}$  is formed due to the superposition of the AC and DC field [30]. The potential minimum  $U_{min}$  strongly depends on the geometrical shape of the trap (*i.e.* diameter of the trap  $d_{AC}$  and the distance  $z$  between the ring electrodes). When a charged particle is injected into the trap, it will be hold in this potential minimum. According to Davis *et al.*, one can determine the stability regions as a function of the applied AC voltage  $U_{AC}$  and the frequency  $\omega$  by solving eqn (29) for a specific trap geometry.

The amplitude of the AC voltage is kept constant during an experiment typically between values of 3 - 5 kV. The frequency can be adjusted at any time of the experiment and takes value between 50 - 200 Hz. By applying a DC voltage to the outer ring electrodes,

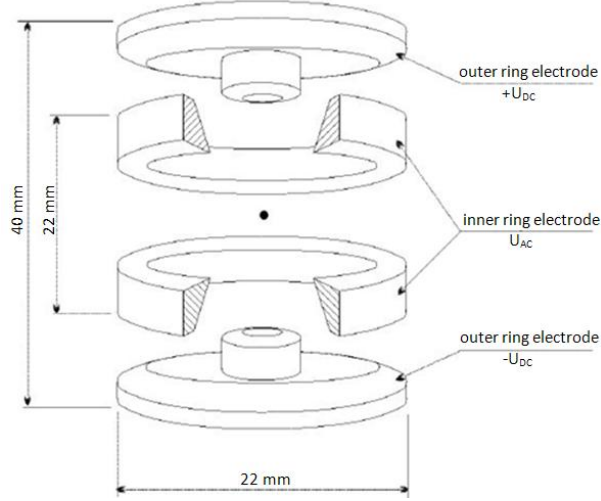


Figure 10: Schematic representation of the EDB trap, which consists of four ring electrodes [31].

a equilibrium between the (homogeneous) electrical force  $\vec{F}_{E,DC}$  exerted on the charged aerosol and its gravitational force  $F_G$  is established to keep the aerosol levitating in the trap:

$$F_{E,DC} = F_G \quad (30)$$

$$\Rightarrow q \cdot E = q \cdot \frac{U_{DC}}{d} = m \cdot g \quad (31)$$

$$\Rightarrow U_{DC} = \frac{m}{q} \cdot d \cdot g, \quad (32)$$

where  $m$  is the mass,  $q$  is the charge of the aerosol particle and  $d$  is the distance between the outer ring electrodes. Eqn (32) shows, that the DC voltage is direct proportional to the mass-to-charge  $m/q$  ratio of the particle. This feature can be used to detect a change in mass of the particle due absorption of molecules from ambient or evaporation (see section "4.1.2.1  $U_{DC}$  mass determination").

### 3.1.3 Cooling system

Fig. 11 shows schematically the setup of the glass cryostat to cool the EDB down to atmospheric temperature. Therefore, a three wall glass chamber with four optical ports is constructed. A insulation vacuum is applied between the outer walls (black painted area) to avoid a heating of the system from outside. A cooling agent is flowing between the inner walls (black hatched area) to cool the chamber, where the EDB is located

(dotted area). The first optical port located at the bottom side of the cryostat is used to illuminate a trapped aerosol in the EDB with a laserbeam. Three optical ports are located on the side of the cryostat, whereof two of the three ports are used for the CCD cameras to record the near field video image (see section "4.2.1  $U_{DC}$  mass determination") and the far field scattered light of the aerosol (section "4.2.2 Radius determination by Mie phase function analysis"). The third optical port is used to perform Mie resonance spectroscopy by using a ball lens type point source LED as a "white light" source (see section "4.2.4 White light Mie resonance spectroscopy"). The gas inlet and outlet are cooled with a integrated cooling vessel.

To cool the glass cryostat, one can optionally use a circulation thermostat (F25-series, Julabo company) to cool the experiment down to 283 K, or a circulation thermostat (Unistat 420W, Huber company) for experiments at subfreezing temperatures using methylcyclohexane as cooling agent. The EDB can be continuously thermostated between 158 K and 305 K.

Currently, the temperature in the EDB is determined by a calibrated Pt-500 sensor close to the gas inlet and a NTC thermistor close to the upper end cap of the EDB trap. The NTC thermistor is an integrated feature of the humidity sensor G-TUS.13, which is described in section "3.1.5 Relative humidity measurement". Alternatively, the temperature in the EDB can be determined by two calibrated Pt-500 sensors, which are placed at the coldest and warmest place in the chamber, *i.e.* close to the gas inlet and outlet. It is assumed that the EDB exhibits an averaged temperature. The absolute temperature accuracy is  $\pm 0.2$  K, which arises from the temperature difference between the measured locations [31].

The pressure in the EDB can be continuously adjusted between 150 mbar and 850 mbar. Experiments are typically performed between 500 mbar and 800 mbar. Performing experiments above 850 mbar leads to long response times of the air-humidity despite continuous humidification and performing experiments below 150 mbar may lead to voltage breakdowns.

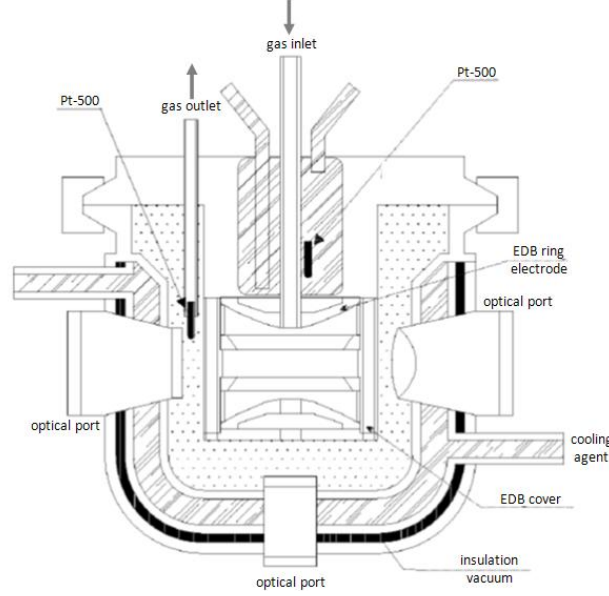


Figure 11: Setup of the glass cryostat to cool the electrodynamic balance [31].

### 3.1.4 Gas phase regulation

To perform measurements with the EDB successfully it is crucial to control partial pressure of water and the total pressure. This is accomplished by a dynamic gas flow system, which is illustrated in Fig. 12. Nitrogen as inert carrier gas is enriched with  $H_2O$  in the tubular overflow and subsequently diluted and pumped through the glass cryostat. In this process, the carrier gas flow  $f_1$  and the gas flow in the tubular overflow  $f_2$  is adjusted by a commercial gas flow controllers (MKS company) with 20 respective 50 sccm total flow with  $\pm 0.5$  sccm accuracy [31].

In the tubular overflow the carrier gas is saturated with water vapor. Therefore, thermostated 2.5 wt% sulphuric acid with known water vapour pressure for tubular overflow temperature  $T_{overflow}$  between  $0^\circ C$  and  $20^\circ C$  is used [33]. Aqueous sulphuric acid is used instead of pure water to prevent contamination (*e.g.* with  $NH_3$ ). Subsequently, the saturated gas flow is heated with a heating wire to avoid unintended condensation. Afterwards, the partial pressure of water is tuned precisely by removing excessive  $H_2O$  in the vapor and aerosol separator.

The volume mixing ratio ( $VMR_{H_2O}$ ) at the end of the tubular overflow is given by the formula

$$(VMR)_{H_2O} = p_{H_2O}^{vap}(c_{H_2SO_4}, T_{overflow})/p_{gas}, \quad (33)$$

where  $p_{H_2O}^{vap}(c_{H_2SO_4}, T)$  denotes the temperature-dependent water vapour pressure of 2.5 wt%  $H_2SO_4$  and  $p_{gas}$  denotes the total pressure in the gas mixing system. To attain

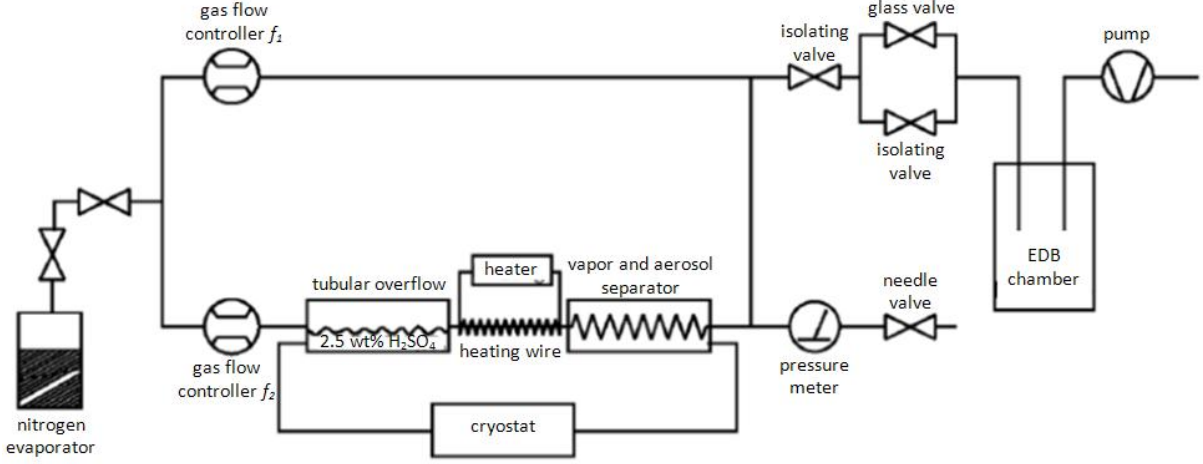


Figure 12: Schematical setup of the gas phase regulator of the electrodynamic balance. See the text above for explanation.

small water partial pressures, this gas flow  $f_2$  is diluted with pure carrier gas nitrogen. The resulting volume mixing ratio is given by

$$(VMR)_{H_2O}^{end} = (VMR)_{H_2O} \cdot f_2 / (f_2 + f_1). \quad (34)$$

A part of the gas flow is pumped through the EDB chamber with a glass valve. The total pressure  $p_{EDB}$  can be varied with a control computer. Therefore, the partial pressure of water in the EDB chamber  $p_{H_2O,EDB}$  is given by

$$p_{H_2O,EDB} = (VMR)_{H_2O}^{end} \cdot p_{EDB} \quad (35)$$

$$= p_{H_2O}^{vap}(CH_2SO_4, T) \cdot \frac{f_2}{f_2 + f_1} \cdot \frac{p_{EDB}}{p_{gas}}. \quad (36)$$

The relative humidity (RH) of the system is given as the ratio of partial pressure of water in the EDB chamber  $p_{H_2O,EDB}$  and the saturated vapour pressure of pure water in the EDB chamber at temperature  $T_{EDB}$   $p_{H_2O}^{vap}(T_{EDB})$ :

$$RH = \frac{p_{H_2O,EDB}}{p_{H_2O}^{vap}(T_{EDB})} \quad (37)$$

where  $T_{EDB}$  denotes the temperature in the EDB chamber. With the technically prescribed specifications one can adjust the partial pressures of water between 0.05 mbar and 15 mbar, which allows a RH range from 0% to 100% in the EDB chamber. Experiments are typically performed with a gas flow of 30 sccm.

Characterisic performance	MiniCap 2	G-TUS.13
Operating humidity range	0 to 100% RH	0 to 100% RH
Operating temperature range	-40° to 180° C	-90° to + 85° C
Response time for 90% total range	40 sec.	0.3 sec.
Hysteresis	2% RH	≤1.5% RH
Thermal stability from 5° to 60° C	negligible	±5% RH

Table 1: The most important characteristics of the RH sensors MiniCap 2 and G-TUS.13 are compared. Major advantages of G-TUS.13 is its stability, faster time response and its superior performance at lower temperatures [39, 40].

### 3.1.5 Relative humidity measurement

A critical component for successful analysis of the EDB data is the measurement of the relative humidity (RH). Up to now, a capacitive thin film relative humidity sensor (MiniCap 2, Panametrics, USA) is used. The sensor is calibrated directly in the EDB using the deliquescence relative humidity of different salts. It shows significant hysteresis at high RH which becomes worse with decreasing temperature. Therefore, a capacitance RH sensor with superior design (Type G-TUS.13, UPSI, France) showing a significantly lower hysteresis, faster time response and superior performance at higher humidity is recently installed in the EDB. Table 1 compares the most important characteristics of the MiniCap 2 and the G-TUS.13 sensors.

The G-TUS.13 sensor is calibrated directly in the EDB at room temperature (290 K) using different salts, for which the deliquescence points are known very accurately from the literature [34-38]. Table 2 shows the used salts and their deliquescence RH at 290 K. The calibration of the G-TUS.13 sensor is illustrated in Fig. 13, which shows the relative humidity RH plotted versus the measured output frequency of the RH sensor. Between 0% and 80% RH, the sensor exhibits a linear behaviour. Therefore, the following linear fit is used to relate RH (0% - 80% RH) to the measured output frequency  $x$ :

$$RH[\%] = 632.109 - 337.082 \cdot 10^{-2}x \quad (38)$$

Between 80% and 98% RH, a quadratic function is used to fit the measured output frequency  $x$  to the literature deliquescence RH of NaF and KCl:

$$RH[\%] = -5325.575 + 0.701x - 226.990 \cdot 10^{-5}x^2 \quad (39)$$

By using these two fit equations, the relative humidity in the EDB can be determined accurately at room temperature (290.65 K) for the entire RH range. However, the calibration presented in this work doesn't cover the entire experimental temperature range, since the RH measurement of the sensor depends on temperature. Therefore,

further calibrations (especially at subzero temperatures) are required, if experiments at low temperatures are performed.

Salt	Deliquescence RH at 290 K
Ammonium chloride $\text{NH}_4\text{Cl}$	77.0% RH
Potassium chloride KCl	85.4% RH
Potassium fluoride KF	17.7% RH
Sodium bromide NaBr	45.0% RH
Sodium chloride NaCl	75.3% RH
Sodium fluoride NaF	97.0% RH
Sodium sulfate $\text{Na}_2\text{SO}_4$	84.5% RH

Table 2: Seven different salts with known deliquescence RH are used to calibrate the RH sensor G-TUS.13 at room temperature (290.65 K). The deliquescence RH of the salts are taken from different sources [34-38].

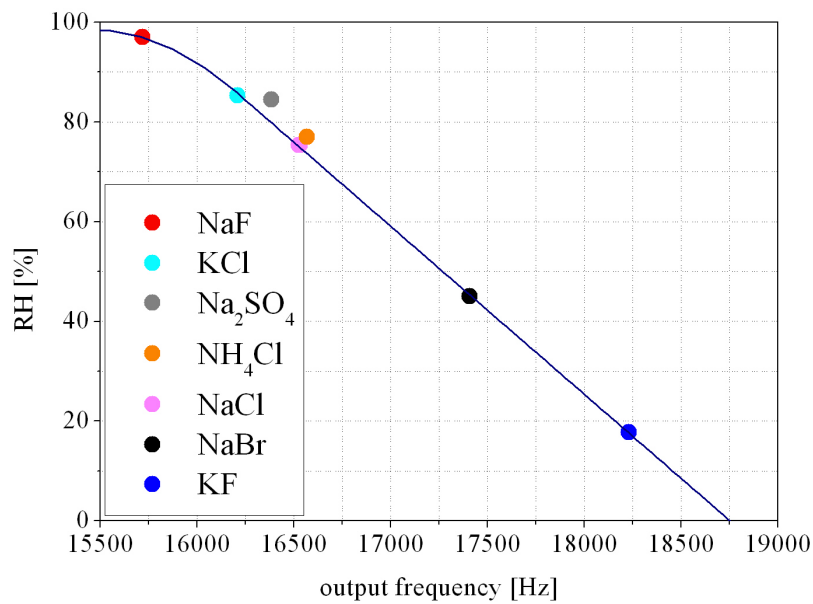


Figure 13: Calibration of the UPSI G-TUS.13 relative humidity sensor using different salts. The calibration is performed directly in the EDB at room temperature (290.65K).

## 3.2 Experimental methods

The EDB contains four independent methods to characterize a trapped aerosol, which will be briefly summarised in this section. A detailed explanation of the methods can be found in different sources [?].

### 3.2.1 $U_{DC}$ mass determination

The particle is illuminated by two collinear laser beams (HeNe laser, 633 nm; Ar(+) laser, 488 nm) from below. The near field video image of the particle is recorded on CCD sensor 1, which is exemplary shown in Fig. 14. A liquid particle is recorded as two points with an approximate distance of the particle's diameter (so-called "hot spots", section "3.2.3 Angular distribution of the scattered light"), whereas a solid particle will be seen typically as an irregular shaped patch. Only a single crystal of sufficient size shows its characteristics habit (right panel of Fig. 14). A control computer is used to adjust the DC voltage for compensating the gravitational force by using an automatic feedback loop, which holds the particle steadily in the middle of the monitor [41]. According to eqn. (32), the particle's mass is direct proportional to the applied DC voltage  $U_{DC}$ . Hence a change in DC voltage is a direct measure of the particle's change in mass.

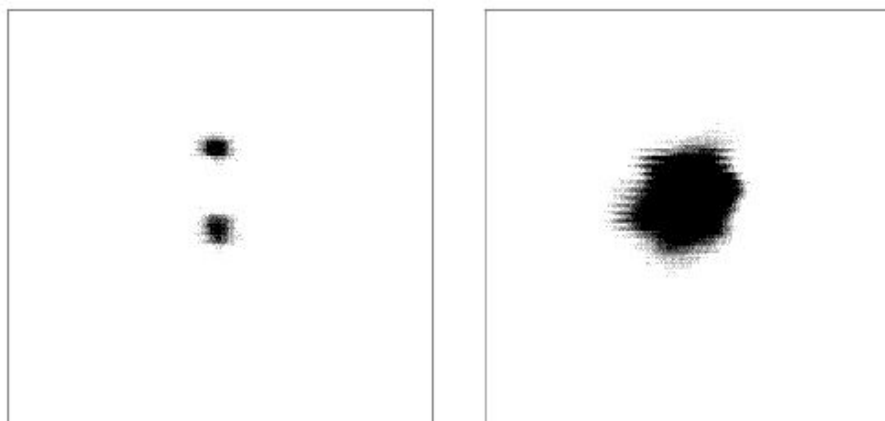


Figure 14: Near field image of a illuminated particle: (left) of a liquid and (right) of a solid particle [31].

### 3.2.2 Radius determination by Mie phase function analysis

The particle is illuminated by two collinear laser beams (HeNe laser, 633 nm; Ar(+) laser, 488 nm) from below (see Fig. 9). The two dimensional angular scattering pattern is recorded with CCD sensor 2 by measuring the elastically scattered light from the laser. If the particle is of spherical shape the scattering pattern is regular and the mean distance between the fringes is a good measure of the particle's radius (to an accuracy of

5%) by analyzing the Mie phase functions [42]. Furthermore a liquid-to-solid transition can be deduced from the fringe pattern, which is regular for a liquid spherical particle and irregular for a crystalline non-spherical one [43]. This is shown in Fig. 15.

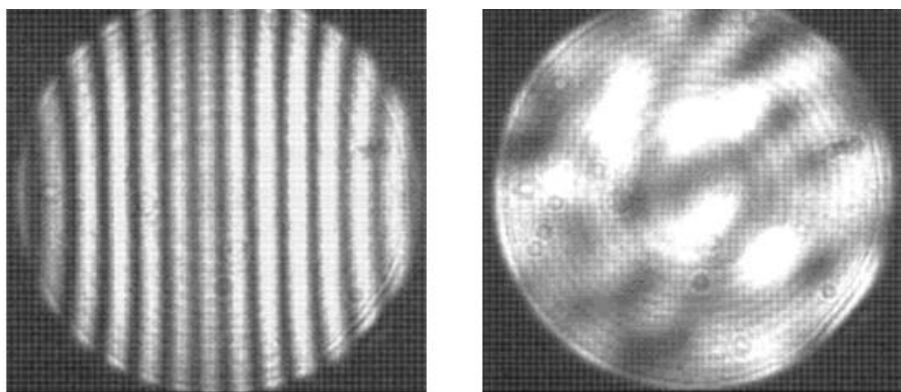


Figure 15: Far field image of a illuminated particle: (left) Regular pattern of a liquid and (right) irregular pattern of a solid particle [31].

### 3.2.3 Liquid-solid phase identification by analysing the Light-scattering intensity fluctuations

A photomultiplier (as point detector in Fig. 9) is used to measure the scattering intensity at  $90^\circ$  to the incident beam. The signal is fed to an analogue lock-in amplifier to measure the intensity fluctuations. A homogeneous spherical particle will show a constant scattering intensity and hence a very small temporal fluctuation amplitude. In contrast a non-spherical particle will scatter light with different intensities into the photomultiplier depending on its orientation relative to the incoming laser beam due to Brownian rotational motion in an EDB [44]. This results in intensity fluctuations that are larger by at least one order of magnitude than those of a spherical homogeneous particle [45].

This is illustrated in an experiment with an NaCl particle performed by Krieger and Braun (2001) [45]. Fig. 16 shows the raw data of a typical experiment with an NaCl particle performed at a temperature of 274 K. Panel (a) shows the change in relative humidity during the experiment, panel (b) the corresponding DC voltage compensating the gravitational force. It is obvious that the initially dry NaCl particle deliquesces at a relative humidity of roughly 75%. Panel (c) shows the radius data obtained by analyzing the Mie phase functions of the elastically scattered light. Only if the particle is liquid the analysis as described above works correctly, if the particle is solid then the analysis yields an arbitrary number for the radius. Panel (d) shows the scattering intensity measured with the photomultiplier. It can be seen that this value drops about two order of magnitude when the solid to liquid transition occurs. Whereas the scattering intensity of the deliquesced, liquid particle is the same for every deliquescence-efflorescence cycle, the scattering intensity of the consecutively dried NaCl particle varies from cycle to

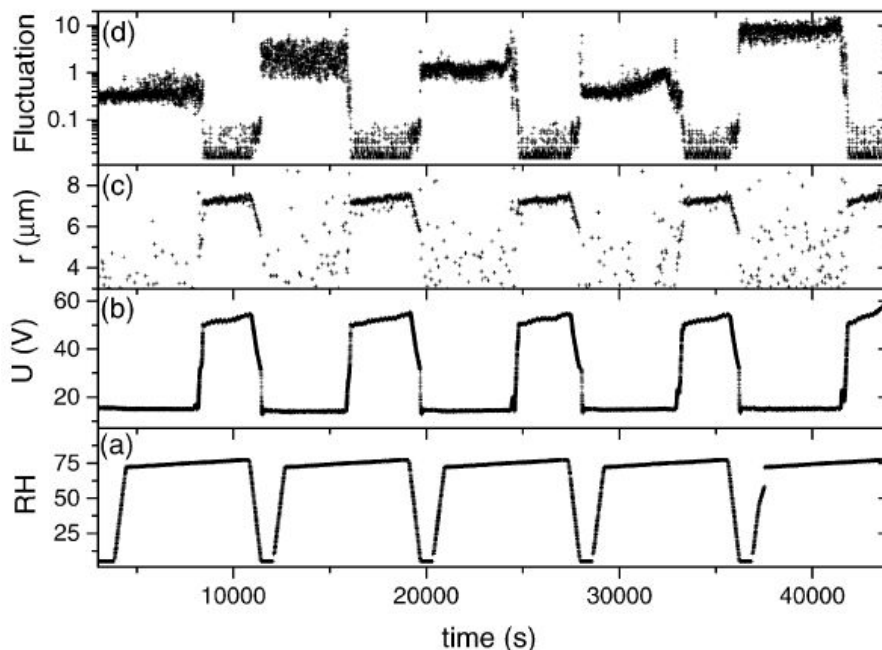


Figure 16: Rawdata of typical NaCl deliquescence–efflorescence cycles, for explanation see text [45].

cycle by almost one order of magnitude. The reason may be a different morphology, depending on whether a single crystal or a polycrystalline material crystallizes during the efflorescence [45].

### 3.2.4 White light Mie resonance spectroscopy

A ball lens type point source LED is used as a "white light" source with high spatial coherence ( $50 \mu\text{m}$  source diameter, peak wavelength  $\approx 589 \text{ nm}$ , spectral bandwidth at 50%  $\approx 16 \text{ nm}$ ) to focus the light on the levitated particle and a pierced mirror to collect the Mie resonance spectra in a backscattering geometry [46] (as shown in Fig. 9). An optical fibre is employed to deliver the backscattered light from the particle to a 150 mm spectrograph with a slow scan back-illuminated CCD array detector as an optical multichannel analyzer (OMA). The resolution of the spectrograph-OMA combination is about 0.5 nm, which excludes the observation of the narrowest resonances in the backscatter spectrum. From Mie resonance spectra analysis one can deduce the change in particle's radius with a sensitivity of 0.2 nm [3].

As explained in section "3.2 Mie Scattering", the extinction and scattering spectra of dielectric spheres with small absorption show a ripple structure, *i.e.* irregularly spaced sharp peaks (modes) as a function of the size parameter  $x$ :

$$x = \frac{2\pi r}{\lambda} \quad (40)$$

where  $r$  is the sphere radius, and  $\lambda$  is the wavelength. In principle, the radius and refractive index of a spherical particle can be deduced by analyzing the Mie resonance spectra, given that the resonance peaks can be determined accurately. But since the resolution of the spectrograph-OMA combination is limited, only modes of high order number are detected, which does not allow unambiguous assignment of the modes. This limits the radius determination to about 5% precision if the refractive index is known. However, the radius change can be determined without identifying the exact mode of the resonances by considering that it will be reflected in a shift of the resonance spectrum given that the particle is homogeneous [47]. If one tracks only the position of one arbitrary distinct mode,  $\lambda_0$ , during its shift, the resonance size parameter of the mode,  $x$ , remains constant:

$$r(t) = \frac{\lambda(t)r_0}{\lambda_0} \quad (41)$$

This property allows the calculation of the radius with time once an initial radius  $r_0$  has been determined from the analysis of the Mie phase functions (see section "4.2.2 Radius determination by Mie phase function analysis") [47].

Fig. 17 illustrates how a LED spectrum is obtained. The red curve in panel (a) shows the intensity measured when the particle is removed from the illuminated region by applying an additional DC voltage to the outer ring electrodes of the EDB. This is the emission spectrum of the LED originating from reflections from the walls of the chamber, which serves as reference in the following. The black line in panel (a) shows the backscattered intensity when the particle is moved back into the center of the balance. Dividing this spectrum by the reference leads to the spectrum of panel (b), which is further processed with a smoothing FFT filter employing the bandwidth of the spectrograph-OMA combination. The resulting Mie resonance spectrum is plotted in panel (c), showing the typical double-peak structure. By tracking a certain peak (*e.g.* peak at 600 nm) during its shift to lower or higher wavelength due to shrinking or growing of the particle, one can determine the radius change accurately by using eqn (41).

### 3.3 High resolution Mie resonance spectroscopy

As the main focus of this thesis, a method to characterize the aerosol in the EDB is developed in addition to the previous ones mention above and is presented in this section. A high resolution Tunable Diode Laser (TDL) of very small bandwidth (New Focus High-Power 6300 Velocity Tunable Diode Laser, model 6312, tuning range: 765 nm - 781 nm, bandwidth:  $\leq 300$  kHz) is used to perform Mie resonance spectroscopy with high resolution, which in principle should allow the observation of the narrowest resonance peaks (*i.e.* lowest-order TE and TM modes). Furthermore, in order to assign the measured resonance peaks to wavelength and compare them to Mie calculations, a Michelson interferometer based wavemeter is used to determine the wavelength of the TDL steadily.

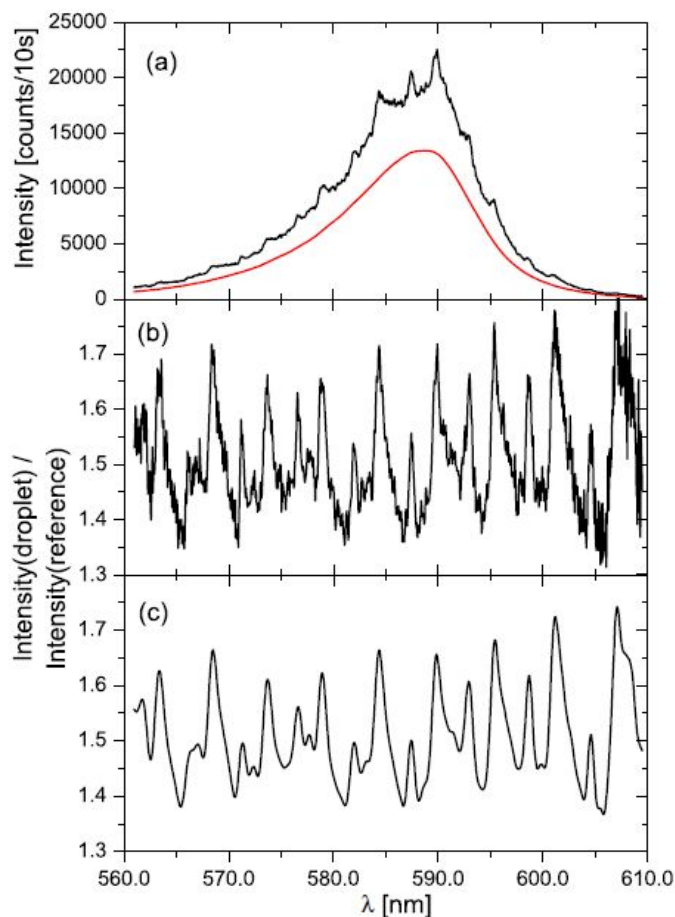


Figure 17: Example of a LED spectrum taken from a liquid spherical particle. Panel (a) shows the LED reference spectrum (red curve) and the original intensity of light scattering by the particle. The latter is plotted in panel (b) after background correction and dividing by LED reference. The signal is smoothed by application of an FFT filter and shown in panel (c) [46].

Fig. 18 shows the schematical setup of the high resolution Mie resonance spectroscopy. The tunable linear polarized laser from the TDL is splitted into 2 beams with a beam splitter. One laser beam is led to the Michelson interferometer wavemeter, which allows a steady determination of the wavelength of the TDL with precision lower than to 0.01 nm every few seconds (see section "Michelson interferometer"). The other laser beam is led to the EDB and used to illuminate the aerosol. The scattered light is measured by a photodetector (New Focus Visible Femtowatt Photoreceiver, model 2151; denoted as PD 1 in Fig. 18) over observation angles ranging from about  $78^\circ$  to  $101^\circ$ . Another photodetector (New Focus Visible Femtowatt Photoreceiver, model 2151; denoted as PD 2 in Fig. 18) is placed close to the EDB to measure the reflections from the wall of the EDB, which serves as a reference (see section "4.3.1 TDL Mie resonance spectrum"). Furthermore, a half-wave plate (polarization rotator) is used to change the

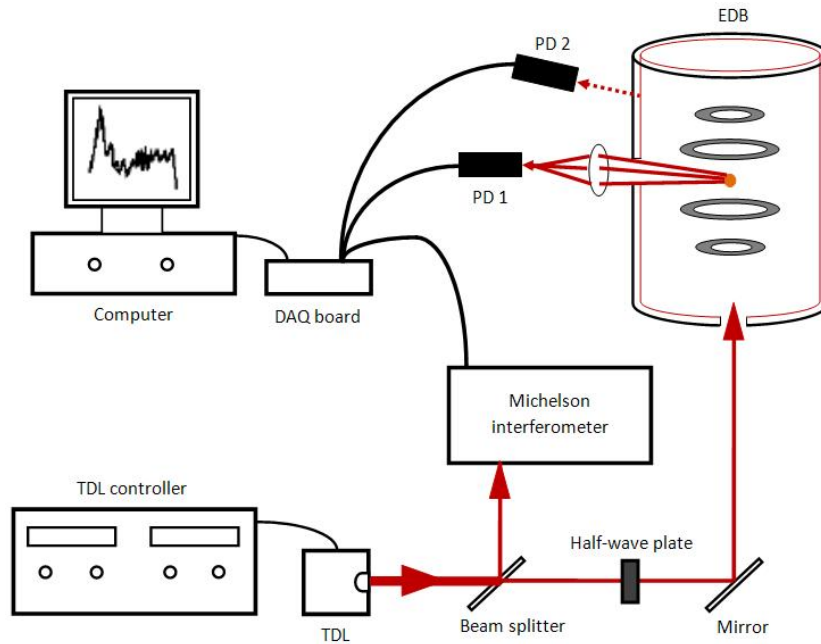


Figure 18: Experimental setup of the High resolution Mie resonance spectroscopy. A Tunable Diode Laser (TDL) is used to illuminate the aerosol in the EDB. A photodetector (PD 1) measures the scattered light from the aerosol, whereas another photodetector (PD 2) measures the reflections from the wall of EDB caused by the laser. A beam splitter is used to deflect a part of the initial laser into the Michelson interferometer wavemeter to perform steady wavelength measurements every few seconds. The measurements are fed to a computer using a multifunction data acquisition board (DAQ) for further data processing.

polarisation of the linear polarized laser from parallel to perpendicular to the scattering plane, which allows performing measurements of pure TE and TM modes of the Mie resonances (see section "3.2.2 Polarisation of the scattered light"). According to the setup of the experiment, tuning the polarization rotator to  $90^\circ$  allows measurement of pure TE modes, whereas  $45^\circ$  provides pure TM modes and  $67.5^\circ$  both (TE and TM) modes. The measured reflections and scattered light from the photodetectors and the wavelength measurements of the Michelson interferometer wavemeter are fed to a computer by means of multifunction data acquisition (DAQ) board (National instruments, model PXI-6220) for further data processing, which is described in the next section.

### 3.3.1 TDL Mie resonance spectrum

Fig. 19 show a raw TDL Mie resonance spectrum of a sucrose particle at subzero temperature (233.6 K) and dry condition (0% RH). The red line shows the scattered light intensity and the green line shows the reflected light from EDB walls as a function

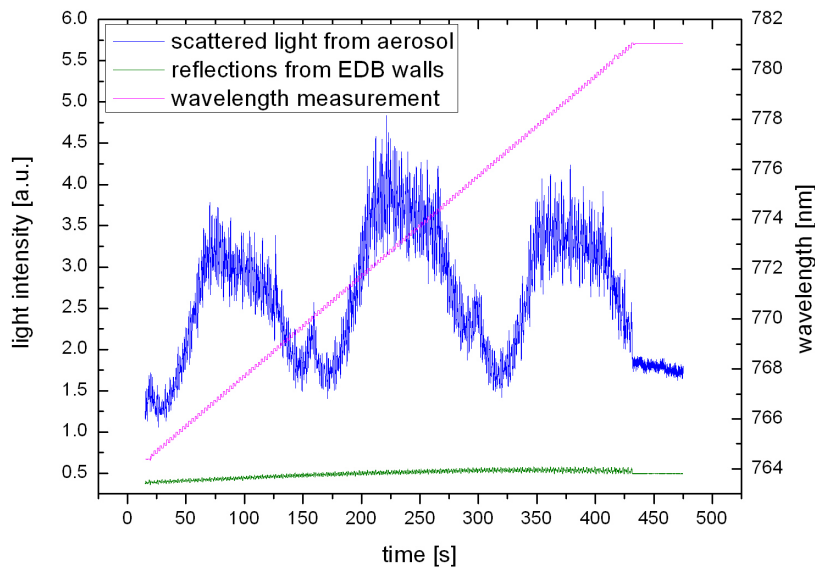


Figure 19: Raw TDL Mie resonance spectrum of a glucose particle taken at  $-39.5^{\circ}$  C and dry condition (0% RH). The TDL is tuned from 765 nm to 781 nm with 0.04 nm/s scan speed. Only pure TE modes are measured (half-wave plate at  $45^{\circ}$ ). The scattered light intensity (red line), reflected light from EDB walls (green line) and the wavelength measurement from the Michelson interferometer (pink dots) are plotted versus time.

of time. The violet points shows the wavelength measurement in nanometer obtained by the Michelson interferometer wavemeter. The spectrum is recorded by tuning the TDL from 765 nm to 781 nm with a scan speed of 0.04 nm/s and a constant diode current of 70 mA. Therefore, it takes about 6 minutes to take a TDL Mie resonance spectrum with the selected scan speed.

As one can see, the reference signal increases as the TDL is tuned to higher wavelength at constant diode current. This is due to the tuning characteristic of the TDL. As the TDL is tuned to higher wavelength, the power of the TDL and thus, the measured signal increases. The scattered light signal (red line) shows a typical ripple structure, i.e. irregularly spaced sharp and broad peaks (corresponding to resonances of different orders) as the TDL is tuned from 765 nm to 781 nm. Moreover, the intensity of the ripple structure increases overall as well due to the increased power of the TDL at higher wavelength. This undesired effect can be removed by taking the reference into account, which is described below.

Both the reference and the scattered light signal exhibits a strong noise with a periodic behavior. This "noise" may arise from the scanning of the TDL or from unintentional residual etaloning from the optical elements of the setup. In addition there is a periodic

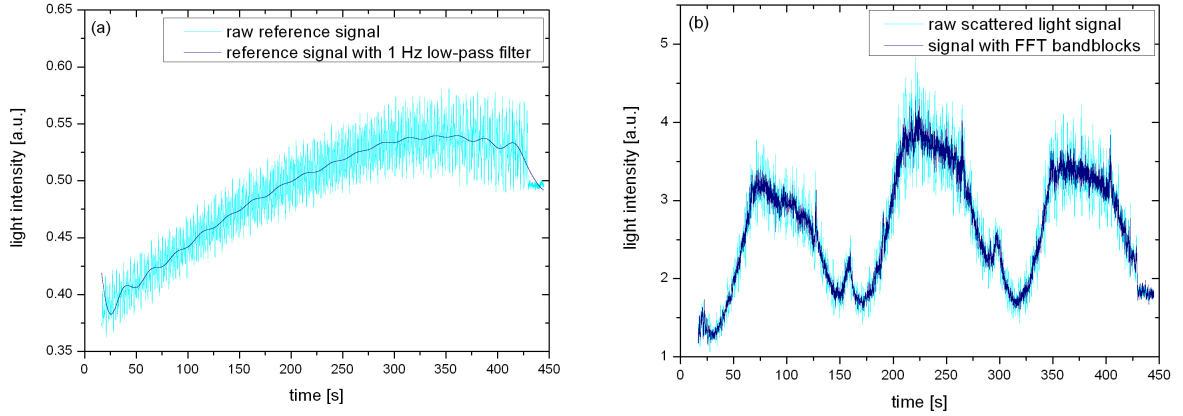


Figure 20: Panel (a) shows the smoothing of the reference signal with a 1 Hz low-pass filter. Panel (b) shows the noise-suppressed scattered light signal.

residual movement of the particle in the trap with the AC frequency, causing additional periodic variations in the scattered intensity. In order to reduce the noise, a rectangular window function is applied to the signal to cut off several frequency ranges to reduce the noise (9.9 to 11.5 Hz, 12.8 to 14.4 Hz and 17.2 to 18.7 Hz FFT bandblocks). Fig. 20b) shows the raw scattered light signal and the signal after applying FFT bandblock, which exhibits clearly a damped noise signal and thus, more distinct Mie resonance peaks.

The reference signal is smoothed by using a 1 Hz low-pass filter, which is shown in Fig. 20a). The processed scattered light signal (Fig. 20b) is divided by the smoothed reference signal to obtain a normed Mie resonance spectrum independent of the output power of the TDL.

The Michelson interferometer wavemeter measures the wavelength of the TDL steadily every few seconds (violet dots in Fig. 19) while the Mie resonance spectrum is recorded. Therefore, the time axis can be easily converted into a wavelength axis by a linear fit of the Michelson interferometer data (see section "Michelson interferometer"). At the end of the data processing, one obtains TDL Mie resonance spectra, where the intensity of the resonances are plotted versus the wavelength. This is shown in Fig. 21.

In principle, it should be possible to observe the Mie resonances of lowest order with this method. Therefore, this method is a huge improvement of the Mie resonance spectroscopy compared to the method using the LED, which doesn't allow the observation of narrow resonance peaks due to its lower resolution (0.5 nm) (see section "XXX"). Since the measured resonances can be assigned very precisely to wavelength ( $\leq 0.01$  nm) by means of the Michelson interferometer wavemeter, it should be possible to gain information about the size and refractive index of a particle by comparing the spectral locations of the measured TE and TM modes with Mie calculations for spheres. Moreover, informations about the radial refractive index change of a inhomogeneous particle

(*e.g.* glassy particle) can be obtained by comparing the measured Mie resonances with Mie calculations for spheres with a radial gradient in refractive index. First experiments using this newly developed method are performed in this thesis and can be found in section "7 Glassy sucrose particle").

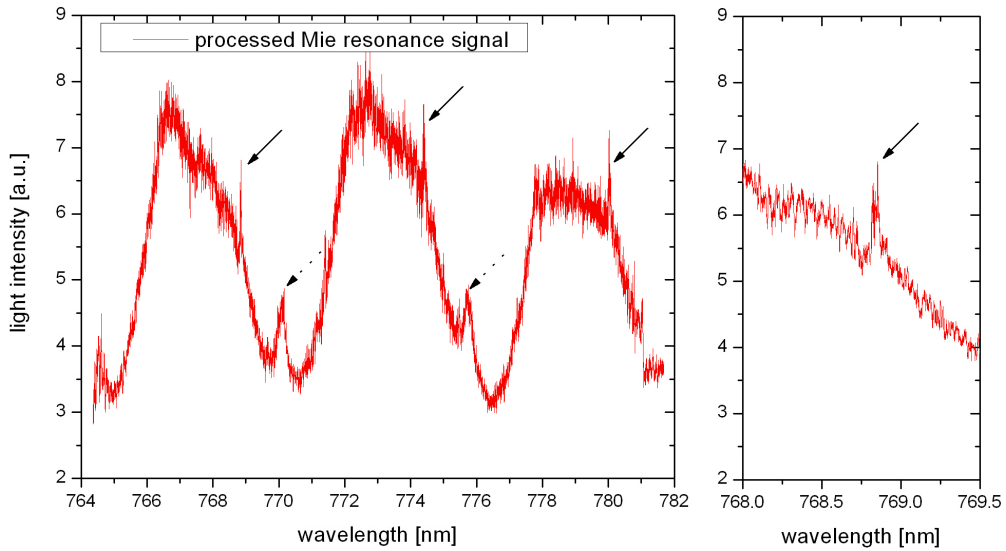


Figure 21: A processed TDL Mie resonance spectrum, where the light intensity is plotted versus wavelength. The spectrum shows resonances of two different orders (solid and dashed arrow). They are more distinct than the raw signal (compare with Fig. 19). Right panel shows the narrow peak at 769 nm in an enlarged size.

## 4 Michelson interferometer (MI)

The Michelson interferometer (MI) is one of the most common configuration for optical interferometry and was invented by Albert Abraham Michelson. Michelson, along with Edward Morley, used this interferometer in the famous Michelson-Morley experiment (1887) to show the constancy of the speed of light across multiple inertial frames, which removed the conceptual need for a luminiferous aether to provide a rest frame for light ([?]ichelsonmorley). The principle of the MI became the basis of numerous interferometry devices (*e.g.* interference comparator and interference microscopy). It can be used to perform measurements on wavelength, distance, index of refraction, and temporal coherence of optical beams. For our purposes, a Michelson interferometer is constructed to measure the wavelength of a tunable laser with high precision, which will be discussed in this chapter.

The principle of the MI is discussed in section "4.1 Theoretical Background of the Michelson Interferometer". The design and operational principle of the newly developed Michelson interferometer is discussed in section "4.2 Experimental setup". The precision of the MI and other important characteristics of the MI are analysed and discussed in section "4.3 Characteristics of the Michelson Interferometer".

### 4.1 Theoretical Background of the Michelson Interferometer

#### 4.1.1 Basic concept of an interferometer

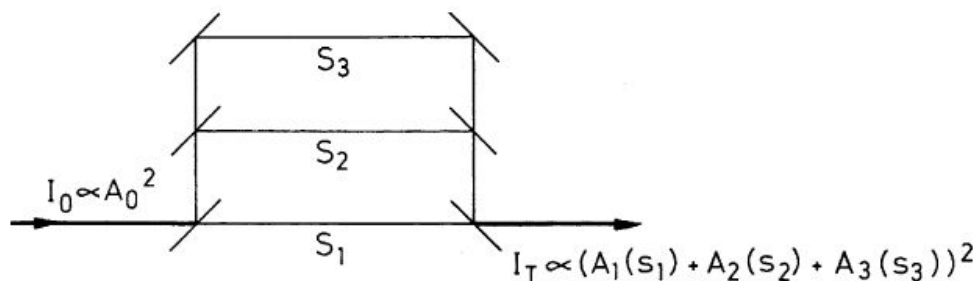


Figure 22: Schematic illustration of the basic principle for all interferometers.

The basic principle of all interferometers may be summarized as follows. The incident lightwave with intensity  $I_0$  is divided into two or more partial beams with amplitudes  $A_k$ , which pass different optical path lengths  $s_k = nx_k$  (where  $n$  is the refractive index) before they are again superimposed at the exit of the interferometer (see Fig. 22). Since all partial beams come from the same source, they are coherent as long as the maximum path difference does not exceed the coherence length of the light source [49]. The total amplitude of the transmitted wave, which is a superposition of all partial waves, depends on the amplitudes  $A_k$  and on the phases  $\phi_k = \phi_0 + 2\pi s_k/\lambda$  of the partial

waves. Therefore, it depends sensitively on the wavelength  $\lambda$ . The maximum transmitted intensity is obtained when all partial waves interfere constructively. This condition is fulfilled if the optical path difference  $\Delta s$  is an integer multiple of the wavelength  $\lambda$ :

$$\Delta s = m\lambda \quad (42)$$

In general, the mathematical treatment of the interferometer is carried out by using plane waves. The electric field  $\vec{E}$  of the incident plane wave is given as

$$\vec{E} = \vec{E}_0 \cos(\omega t - Kx), \quad (43)$$

where  $\omega$  is the angular frequency and  $K$  the wavenumber. In its complex form, it is given as

$$E = A_0 e^{i(\omega t - Kx)} + A_0^* e^{-i(\omega t - Kx)}. \quad (44)$$

The intensity of the plane wave is given as

$$I = c\epsilon_0 E^2 \quad (45)$$

and its time-averaged value is

$$\bar{I} = \frac{1}{2} c\epsilon_0 A_0 A_0^*, \quad (46)$$

where  $c$  is the speed of light in vacuum and  $\epsilon_0$  is the vacuum permittivity.

The Michelson interferometer is a device in which only two partial beams interfere.

#### 4.1.2 Principle of Michelson interferometer

The basic principle of the Michelson interferometer is illustrated in Fig. 23. The incident plane wave

$$E = A_0 e^{i(\omega t - kx)} \quad (47)$$

is split by the beam splitter S (with reflectivity  $R$  and transmittance  $T$ ) into two waves

$$E_1 = A_1 e^{i(\omega t - kx + \phi_1)} \quad (48)$$

$$E_2 = A_2 e^{i(\omega t - kx + \phi_2)}. \quad (49)$$

If the beam splitter has negligible absorption ( $R + T = 1$ ), the amplitudes  $A_1$  and  $A_2$  are determined by  $A_1 = \sqrt{T}A_0$  and  $A_2 = \sqrt{R}A_0$  with  $A_0^2 = A_1^2 + A_2^2$ .

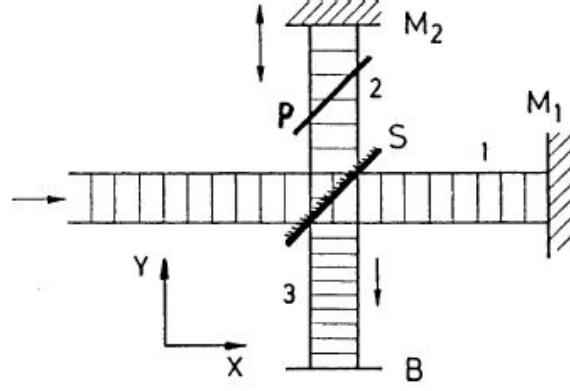


Figure 23: Two-beam interference in a Michelson interferometer.

After being reflected at the plane mirrors  $M_1$  and  $M_2$ , the two waves are superimposed in the plane of observation  $B$ . In order to compensate for the dispersion that beam 1 suffers by passing twice through the glass plate of beam splitter  $S$ , often an appropriate compensation plate  $P$  is placed in one side arm of the interferometer. The amplitudes of the two waves in the plane  $B$  are  $\sqrt{RTA_0}$ , because each wave has been transmitted and reflected once at the beam splitter surface  $S$ . The phase difference  $\phi$  between the two waves is given by

$$\phi = \frac{2\pi}{\lambda} 2(SM_1 - SM_2) + \Delta\phi \quad (50)$$

where  $\Delta\phi$  accounts for additional phase shifts, which may be caused by reflection at the beam splitter. The total complex field amplitude in the plane  $B$  is then

$$E = \sqrt{RT}A_0 e^{i(\omega t + \phi_0)} (1 + e^{i\phi}). \quad (51)$$

According to eqn (46), the time-averaged intensity  $\bar{I}$  in the observation plane  $B$  is given by

$$\bar{I} = 2c\epsilon_0 A_0 A_0^* = c\epsilon_0 A_0^2 (1 + \cos\phi) = \frac{1}{2} I_0 (1 + \cos\phi). \quad (52)$$

If mirror  $M_2$  moves along a distance  $\Delta y$ , the optical path difference changes by  $\Delta s = 2n\Delta y$  ( $n$  is the refractive index between  $S$  and  $M_2$ ) and the phase difference  $\phi$  changes by  $2\pi\Delta s/\lambda$ . Fig. 24 shows the intensity  $I_T(\phi)$  in the plane  $B$  as a function of  $\phi$  for a monochromatic incident plane wave. For the maxima at  $\phi = 2m\pi$  ( $m = 0, 1, 2, \dots$ ), the transmitted intensity  $I_T$  becomes equal to the incident intensity  $I_0$ , which means that the transmission of the interferometer is  $T_I = 1$  for  $\phi = 2m\pi$ . In the minima for  $\phi = (2m+1)\pi$  the transmitted intensity  $I_T$  is zero.

The Michelson interferometer can be used for absolute wavelength measurements. As the mirror M2 is moved along a distance  $\Delta y$ , the number  $N$  of maxima counted in the detection plane B is given by

$$N = \frac{2\Delta y}{\lambda}. \quad (53)$$

The operational principle of the Michelson interferometer is described in the next section.

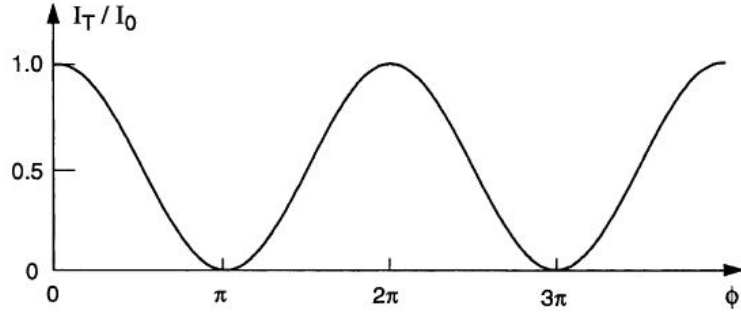


Figure 24: Intensity transmitted through the Michelson interferometer as a function of the phase difference  $\phi$  between the two interfering beams for  $R = T = 0.5$

## 4.2 Experimental setup

The Michelson interferometer wavemeter developed in this thesis is based on the version of P. J. Fox *et al.* [19]. It is a simple, compact, and cost effective wavemeter with picometer accuracy. The essential concept behind this type of wavemeter is simple: a Michelson interferometer is arranged to simultaneously detect interference fringes from two overlapping and copropagating laser beams, one of which has a known wavelength. The relative lengths of the interferometer arms are varied while interference fringes of both the known and unknown lasers are counted. The ratio of the two fringe counts gives the ratio of the wavelengths. A detailed explanation of the design and operational principle can be found in section "4.2.1 Design and operational principle of MI". The configuration of the detectors used to observe and count the fringes are described in section "4.2.2 Design of the detectors".

### 4.2.1 Design and operational principle of MI

As mentioned above, a MI is basically composed of two mirrors and a beamsplitter (see Fig. 23). As mirror M2 is moved, the path difference between the two arms changes, resulting in changes in the interference pattern. The number of fringes counted as the mirror is moved distance  $\Delta y$  is given by equation (53). For a reference laser it is  $N_R = 2\Delta y/\lambda_R$ , where  $\lambda_R$  is the wavelength of the reference laser. For a different (unknown)

laser, at some wavelength  $\lambda_U$ ,  $N_U = 2\Delta y/\lambda_U$  fringes would be counted. If both lasers propagate through the interferometer simultaneously, then the distance moved by the mirror must be the same for each. Thus, the ratio of fringes counted gives the wavelength of the unknown laser, provided that the wavelength of the reference laser is well defined:

$$\lambda_U = \frac{N_R}{N_U} \lambda_R. \quad (54)$$

Resolution of 1 in  $10^6$  is achieved if one million fringes are counted. For a HeNe laser ( $\lambda = 632.8$  nm), the mirror M2 in the Michelson interferometer must be moved about 30 cm according to eqn (53). This can be halved by using an arrangement whereby the mirrors in both arms of the interferometer are moved simultaneously. The schematical setup is illustrated in Fig. 25a) and the built Michelson interferometer in Fig. 25b). The entire wavemeter, including the HeNe reference laser, is built on an aluminium plate (300 mm  $\times$  150 mm). A HeNe laser (Melles Griot, 05-LLR-811) with cavity length of 20 cm is used as the reference since it is low in cost and has well-defined wavelength ( $\lambda_{HeNe} = 632.9908$  nm in vacuum ) [50]. The short cavity ensures that only two longitudinal, orthogonally polarized modes may be excited simultaneously. The plane mirrors M1 and M2 are replaced with cornercubes to make the system insensitive to changes in the orientation of the reflector as it is moved.

The HeNe beam (dot-dashed red line) is collimated by using optical lenses consisting of an achromatic doublet (AD, focal length  $f_1 = 10$ ) and a Plano-convex lens (PD, focal length  $f_2 = 50$ ) and subsequently reflected by mirror M1 and splitted at the 50/50 nonpolarizing beamsplitter (BS). The transmitted beam reflects off M2 and then strikes the cornercube (CC1), which sends the beam back parallel to its original path with some transverse displacement. The beam reflected from BS travels via M3, M4 and M5 to the corner cube CC2, where it also is reflected back parallel to its original path. The two HeNe beams, one coming from CC1 and the other from CC2, converge at the beamsplitter and produce two output beams. One beam is deflected by a prism mirror (M6) and led into a photodiode (D1 in Fig. 25a); OSI Optoelectronics, UDT-455, model: TO-5) to detect the interferences, whereas the other beam is used as a tracer beam to align the second laser. The second laser (in our case the TDL) is aligned antiparallel to the beam emitted from the wavemeter and thus, travels a path exactly the reverse of that travelled by the HeNe beam. The beams of the TDL is likewise deflected by M6 and its interferences are detected with a photodiode (D2 in Fig. 25a); OSI Optoelectronics, UDT-455, model: TO-5). Interference filters (IF in Fig. 25a) are placed in front of the detectors for the suppression of extraneous light.

The tracer beam is very convenient for alignment, but it might destabilize the TDL laser. The HeNe laser exhibits two longitudinal modes with opposite polarizations due to its short cavity length of 20 cm. Therefore, a polarisation prism is placed in front of the HeNe laser to select the mode, which is perpendicular to the linear polarized laser from the TDL to solve this problem.

Smooth motion of the cornercube reflectors along the track is crucial to the operation

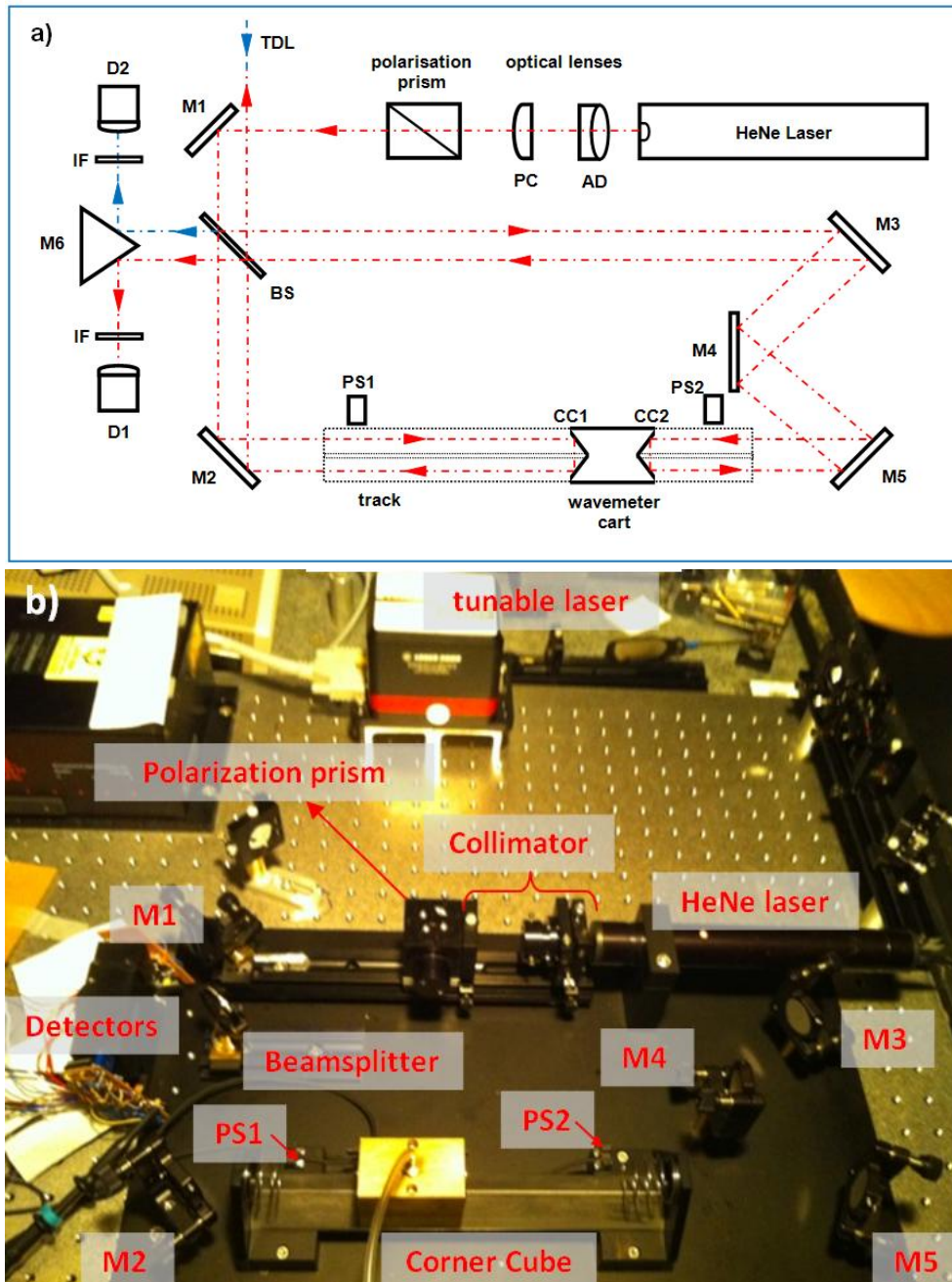


Figure 25: a) Schematic setup of Michelson interferometer. M1-M5: front-aluminized mirrors, M6: aluminum-coated prism mirror, BS: nonpolarizing beamsplitter, AD: achromatic doublet ( $f_1=10$ ), PC: plano-convex collimator lens ( $f_2=50$ ), CC1,2: glass cornercube prisms in the cart, IF: interference filters, D1,2: photodiode (UDT-455). The red arrows show the beam propagation within the Michelson interferometer for the reference HeNe laser. The blue arrows show the tunable diode laser beam, which travels exact the reserved path of the HeNe beam. b) Experimental setup of the Michelson interferometer.

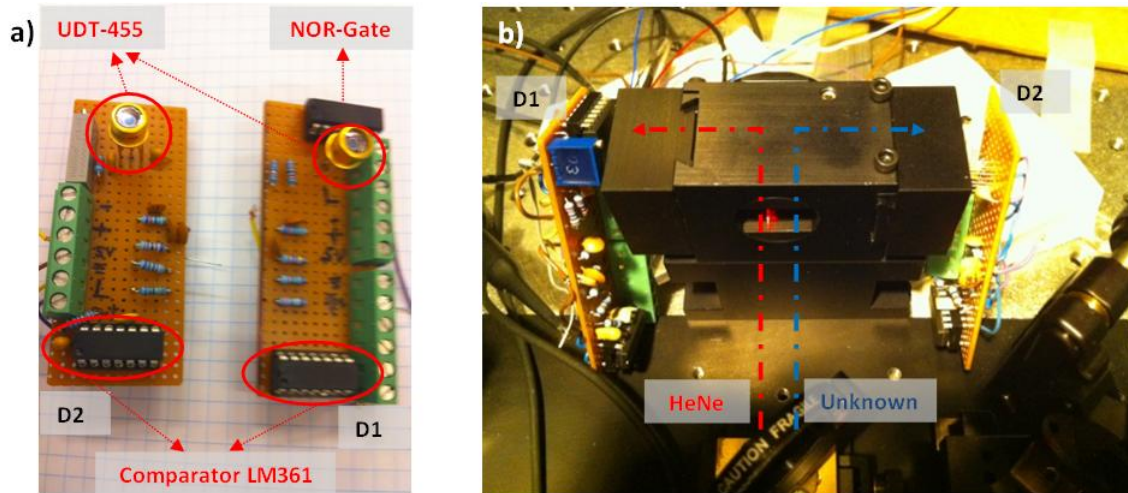


Figure 26: a) Silicon photodiodes (UDT-455) and b) integrated in the Michelson Interferometer.

of the wavemeter. It is particularly important that any vibrations are so small that they do not add or subtract any interference fringes. Therefore, the two cornercubes are mounted on an air bearing, which is a simple device that consists of a cart through which compressed nitrogen flows. The nitrogen is fed into the cart through a rubber hose suspended above the device and flows out through small holes in the bearing face of the cart. The rubber hose is mounted to a motor, which moves the cart smoothly on the track. In addition, springs are mounted at both ends of the track, which allow the cart to change the direction of motion smoothly (see Fig. 25b).

Furthermore, two photoelectric sensors (PS1 and PS2 in Fig. 25b; SunX Panasonic, PM-series) are mounted at both ends of the track. Thereby, the fringes from the HeNe laser und TDL are only counted for the distance between the sensors as the cart is moved on the track. The fringes, which are produced when the cart is at the end of the track and changes its direction, are not included since they are distorted and may affect the wavelength measurement. Whenever the cart has moved the whole distance between the two sensors (either moving from PS1 to PS2 or vice versa), the fringes from the HeNe laser ( $N_R$ ) and TDL ( $N_U$ ) are counted and the wavelength of the TDL is calculated by using eqn (54) with  $\lambda_{HeNe} = 632.8306$  nm (in air: at 94 kPa, 21 °C and 33% RH).

#### 4.2.2 Design of the detectors

The interference fringes are detected by using two silicon photodiodes (OSI Optoelectronics, UDT-455, model: TO-5), which operate in the photoconductive mode (biased) to reduce the response time. A photodiode signal is measured as a current, which must be converted to voltage using a integrated transimpedance pre-amplifier. The sinusoidal voltage signals is converted to TTL pulses with a comparator (National Semiconductor, High Speed Differential Comparators, LM361), and then fed to the multifunction data

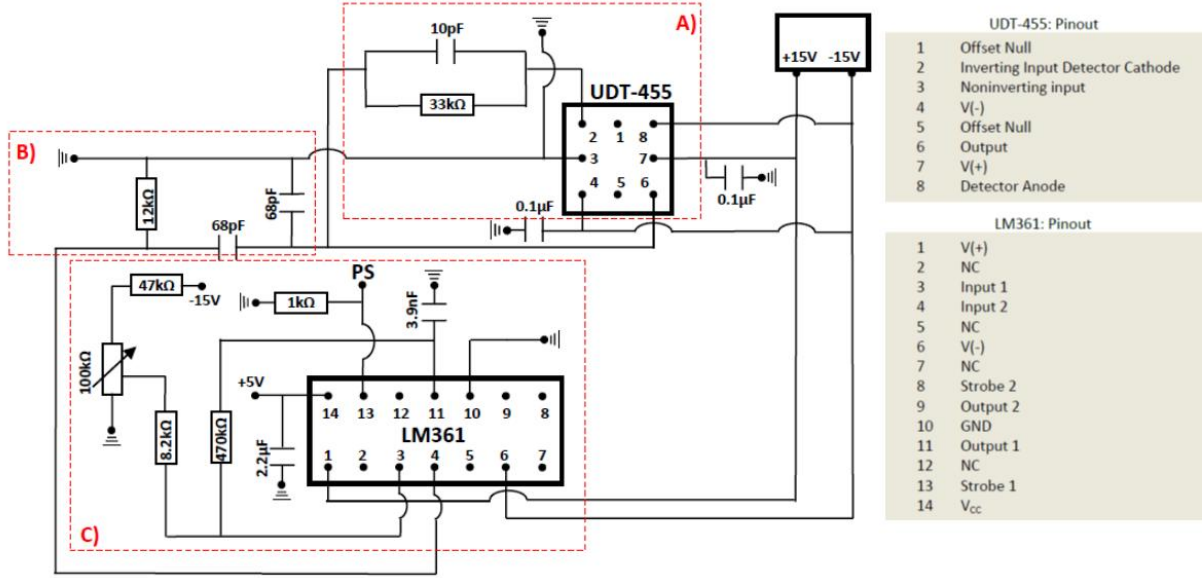


Figure 27: Configuration of the silicon photodiode (UDT-455) operating in the photoconductive mode and the comparator (LM361) to convert TTL pulses.

acquisition board (DAQ) for fringe-counting. The photodiodes are shown in Fig. 26.

Fig. 27 shows the configuration of the detectors. The setup of the detectors can be split in three parts (denoted by red dotted boxes and capital letters), which will be discussed in this section.

**A) Setting of the pre-amplifier:** In order to detect the fringes effectively, it is crucial to configure the pre-amplifier of the photodiode (UDT-455) such, that the output voltage is maximized and the frequency response (of the photodiode / amplifier combination) is optimized for the count rate of the fringes, which is typically 430 kHz - 460 kHz. These two characteristics are given by

$$V_{OUT} = I_P \times R_F \quad (55)$$

$$f_{3dB} = \frac{1}{2\pi C_F R_F}, \quad (56)$$

where  $I_P$  is the light intensity,  $R_F$  feedback resistor and  $C_F$  the feedback capacitor. With  $R_F = 33 \text{ k}\Omega$  and  $C_F = 10 \text{ pF}$ ,  $V_{OUT}$  is typically 200 mV for HeNe laser and 2-3 V for TDL, and  $f_{3dB} \cong 480 \text{ kHz}$ , which exceeds the typical count rate of the fringes. With this  $R_F / C_F$  combination, the pre-amplifier is optimally configured.

**B) Low-pass and high-pass filters:** The amplified sinusoidal voltage signals pass through a low-pass filter to eliminate the high frequency noise signals (up to several MHz). The signals are subsequently AC-coupled by a high-pass filter to eliminate the

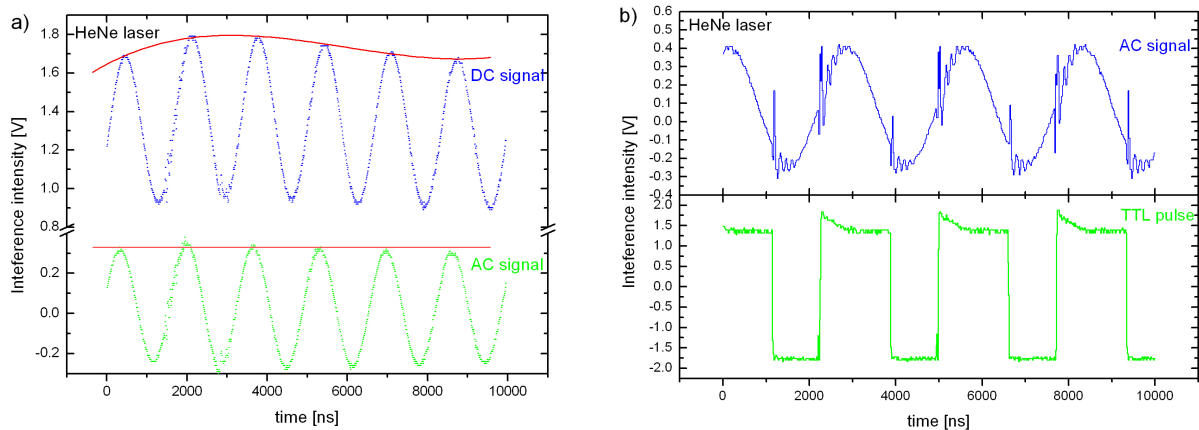


Figure 28: a) The sinusoidal interference fringes from HeNe laser, as DC (blue dotted) and AC signals (green dotted). b) The AC signal (blue line) is converted to TTL pulses (green line) using LM361 comparator. The distortion of the sinusoidal signals arises when TTL pulses are triggered.

contributions from the DC voltage and the beat, since the TTL pulses in the comparator are triggered at the zero-crossing (see box C). This is shown in Fig. 28a).

**C) Signal to TTL pulse conversion:** A comparator (LM361) is used to convert the AC signals to TTL pulses. The TTL pulses causes distortion to the primary AC signals, which may trigger secondary erroneous TTL pulses. This problem is solved by using an inverting Schmitt trigger. This circuit creates a switching band centered around zero with trigger levels  $\pm R_1/(R_1 + R_2) \cdot V_S$ , where  $V_S$  (in our configuration) is the amplitude of the TTL pulse and  $R_1$  and  $R_2$  are the resistances. Thus, the AC signals need to exceed the trigger levels to be converted to TTL pulses. The trigger level has to be adjusted in such a way, that distortions of AC signals are not converted to TTL pulses. With  $R_1 = 8.2 \text{ k}\Omega$ ,  $R_2 = 470 \text{ k}\Omega$  and  $V_S = 3.5 \text{ V}$ , the trigger level is set to 60 mV. Furthermore, a 100 k $\Omega$  potentiometer is integrated in the circuit, which allows a convenient adjustment of the trigger level. The photoelectric sensors (PS1 and PS2 in Fig. 25b) are directly connected to the strobe of the comparator to prevent TTL pulse conversion when the wavemeter cart is at the end of the track.

### 4.3 Characteristics of the Michelson Interferometer

As previously mentioned, the Michelson interferometer wavemeter measures the wavelength of the TDL about every two seconds. If the TDL is kept at fixed wavelength, the wavemeter determines the wavelength with an accuracy of 1 pm. However, if the TDL is tuned continuously during a wavelength measurement, the wavemeter produces only discrete time-averaged wavelength values, since the resolution of the wavemeter is

related to the time, which the wavemeter cart needs to move a full range of the track to perform a measurement. Therefore, the accuracy of the wavemeter decreases as the tuning speed of the TDL increases due to the limited time resolution of the wavemeter, which is typically 1.5 s - 2 s.

Section "4.3.1 Wavelength determination" explains how the wavelength of a continuously tuned TDL is retrieved from the discrete wavelength measurements. In section "4.3.2 Accuracy and precision", the accuracy and precision of the wavemeter are analyzed by performing Rubidium spectroscopy, since the Rubidium absorption lines are known very accurately [51, 52]. The TDL is focused on a Rubidium cell and tuned to the Rubidium absorption lines to observe the fluorescences, which only occur if the wavelength of the TDL match with the absorption lines. Simultaneously the wavelength of TDL is measured and compared with the literature values. A more detailed explanation of this method is given in section "4.3.2.1 Rubidium Spectroscopy".

Furthermore, the discrete wavelength measurements show an untypical behaviour at first sight, if the TDL is tuned. As the laser is tuned from 765 nm - 781 nm, one would expect steadily increasing wavelength outputs from the Michelson interferometer. However, the wavelength outputs are alternately slightly shifted to lower and higher values compared to the expected linear outputs (*e.g.* Fig. 29a und 33). The shift depends on the scan speed of the TDL and the speed and direction of the cart moving on the track. This characteristic is analyzed in section "4.3.3 Analysis of Tunable Diode Laser wavelength measurements at different scan-speeds".

### 4.3.1 Wavelength determination

Fig. 29a) shows the wavelength measurements of the TDL, which is tuned from 770 nm - 772 nm with 0.03 nm/s scan speed. The MI wavemeter output (violet line) and the analog output from the TDL (green line) are plotted versus time. As the TDL is tuned continuously, the analog output increases continuously as well. However, the MI measurement show only distinct (averaged) values due to the time needed to measure the wavelength, *i.e.* the time which the wavemeter cart needs to move a full range of the track (typically 1.5 s - 2 s). In order to obtain continuous wavelengths from the MI, the wavelength outputs are linearly fitted (light blue line in Fig.29b). Thereby one has to take into account, that the MI output and the effective wavelength of the TDL are shifted by the time needed to perform one measurement. Therefore, the linear fit needs to be shifted back in time by the amount, which is needed to perform one measurement (denoted by dark blue line). As mentioned above, one notices the unexpected behaviour of the wavelength measurements (*i.e.* the alternating shifting to lower and higher values compared to the expected linear outputs), which is discussed in section "4.3.3 Analysis of Tunable Diode Laser wavelength measurements at different scan-speeds".

This example shows a remarkable difference between the analog output of the TDL and the MI wavelength measurements. The resolution of the analog output of the TDL is limited to few tenths of a nanometer, whereas the MI wavemeter reaches a resolution of

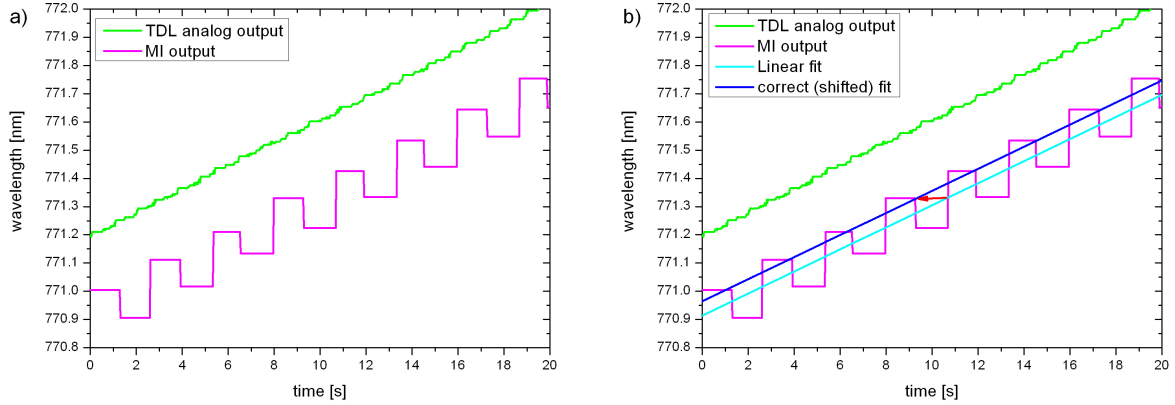


Figure 29: a) MI wavelength measurement with TDL tuned from 770 - 772 nm/s with 0.03 nm/s scan speed (violet line). The green line depicts the TDL analog output. b) A linear fit (light blue line) is applied to wavelength measurements to obtain continuous wavelengths.

few picometers. This shows the great benefit of the developed MI wavemeter. However, the accuracy of the MI needs to be tested, which is content of the next section.

### 4.3.2 Accuracy and precision

The accuracy of MI is analyzed by performing Rubidium spectroscopy [20], where the Rubidium absorption lines are well studied and given in different literatures [51, 52]. The TDL is focused on a cell containing  $^{85}\text{Rb}$  and  $^{87}\text{Rb}$  and tuned to the Rubidium absorption lines to observe the fluorescences, which only occur if the wavelength of the TDL match with the absorption lines. Simultaneously the wavelength of TDL is measured and compared with literature values. The experimental setup to perform accuracy measurements and the required background knowledge are briefly discussed in the following subsection "4.3.2.1 Rubidium spectroscopy".

The accuracy of MI is determined using different scan speeds (typically to perform "High resolution Mie resonance spectroscopy") to excite the Rubidium absorption lines. The conclusions are shown the the subsection "4.3.2.2 Accuracy and precision: results".

**4.3.2.1 Rubidium Spectroscopy** Rubidium is a alkali metal with natural isotope-mixture of 72%  $^{85}\text{Rb}$  and 28%  $^{87}\text{Rb}$  and melting temperature of 39 °C. Thus, the Rubidium atoms confined in a glass cell are gaseous.

Fig. 30a) shows a extract of the energy level scheme of  $^{85}\text{Rb}$  and  $^{87}\text{Rb}$ . The ground state of a Rb atom is 5S. The first excited state is called 5P and split into a  $5P_{1/2}$  and a  $5P_{3/2}$  level due to the spin-orbit interaction (fine structure). To investigate the  $D_1$ -line, *i.e.*

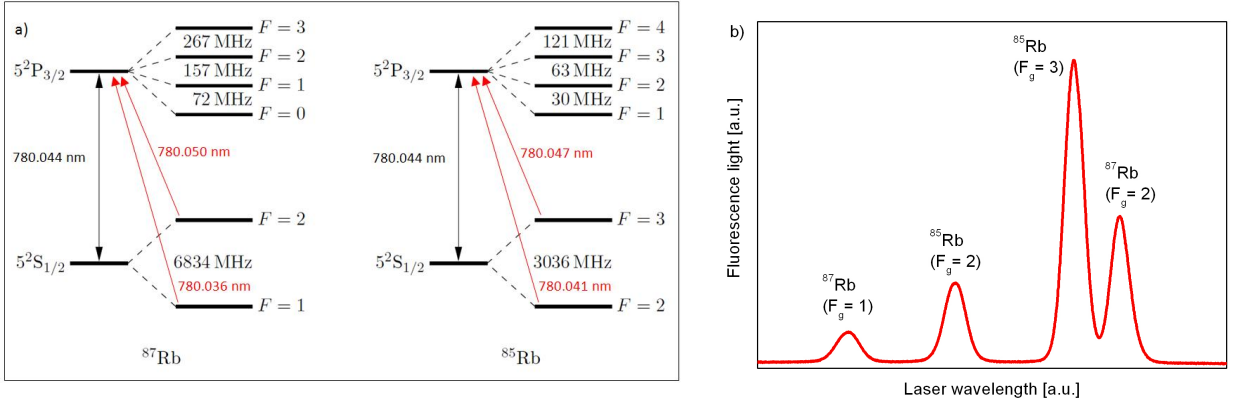


Figure 30: a) Extract of the energy level scheme of  $^{87}\text{Rb}$  and  $^{85}\text{Rb}$  [53]. The red arrows indicate the transitions (D<sub>2</sub>-line) measured in the Rubidium spectroscopy. b) Fluorescence spectrum of the D<sub>2</sub>-line of  $^{87}\text{Rb}$  and  $^{85}\text{Rb}$ .

the transition from  $5\text{S}_{1/2}$  to  $5\text{P}_{1/2}$ , a laser with wavelength of 795 nm is necessary. Since the tunable range of our TDL is limited to 764 - 781 nm, only the D<sub>2</sub>-line (transition from  $5\text{S}_{1/2}$  to  $5\text{P}_{3/2}$ ) is investigated.

Since the total angular momentum  $\vec{J}$  of the shell electrons couple with the nucleus spin  $\vec{I}$ , the fine structure energy levels  $5\text{S}_{1/2}$  and  $5\text{P}_{3/2}$  is further split due to hyperfine structure splitting (denoted by the F-levels in Fig. 30a). The energy splitting of the hyperfine structure is given as [53]

$$\nu_F = \nu_J + \frac{AC}{2} + \frac{B \left[ \frac{3C(C+1)}{4} - I(I+1)J(J+1) \right]}{2I(2I-1)J(2J-1)}, \quad (57)$$

where  $C = F(F+1) - J(J+1) - I(I+1)$  with  $|I-J| \leq F \leq |I+J|$ , and  $A$ ,  $B$  are the hyperfine constants. Since  $^{85}\text{Rb}$  and  $^{87}\text{Rb}$  exhibit different nucleus spin, *i.e.*  $I = 5/2$  ( $^{85}\text{Rb}$ ) and  $I = 3/2$  ( $^{87}\text{Rb}$ ), the energy splittings of the two isotopes are different as well. The splitting of  $5\text{P}_{3/2}$  is so small, that it can not be measured in our experiment. Therefore, only the transitions from the hyperfine structure levels of  $5\text{S}_{1/2}$  to the fine structure level  $5\text{P}_{3/2}$  are measured (denoted by red dashed line in Fig. 30a). The fluorescence spectrum of the D<sub>2</sub>-line of  $^{85}\text{Rb}$  and  $^{87}\text{Rb}$  is shown in Fig. 30b). The wavelengths (in air) of the laser needed to excite the transitions are given in table 3.

Fig. 31 shows a schematical setup of our Rubidium spectroscopy. The TDL is split into two beams by a 50/50 beamsplitter. One beam is focused into the Rubidium glass cell, whereas the other beam is deflected to the Michelson interferometer to perform wavelength measurement. A photodetector (New Focus Visible Femtowatt Photoreceiver, model 2151) is used to detect the Rubidium fluorescence light. The fluorescence signal and the wavelength measurements are simultaneously fed into a computer, where the

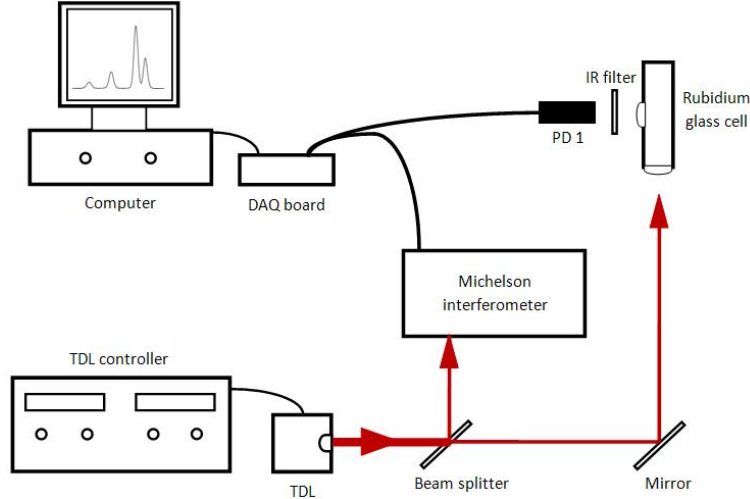


Figure 31: Schematical setup of Rubidium spectroscopy. The TDL is focused into the Rubidium glass cell to excite the  $D_2$ -line. The fluorescence light is detected by using a Photodetector PD1. A infrared filter is placed in front of the detector to suppress background signal caused by the TDL. The fluorescence signal and the MI measurement are fed into a computer by means of multifunction data acquisition (DAQ) board (National instruments, model PXI-6220) for accuracy determination.

fluorescence can be assigned to the wavelength of the laser, which is needed to excite the appropriate transition. Thereby, different scan speeds are used to excite the transitions. The measured wavelengths are compared with literature values and shown in the next subsection.

Rb $D_2$ transition	wavelength (vacuum)	wavelength (in air)
$^{87}\text{Rb}$ ( $F_g = 1$ )	780.232 nm	780.036 nm
$^{87}\text{Rb}$ ( $F_g = 2$ )	780.246 nm	780.050 nm
$^{85}\text{Rb}$ ( $F_g = 2$ )	780.238 nm	780.041 nm
$^{85}\text{Rb}$ ( $F_g = 3$ )	780.244 nm	780.047 nm

Table 3: Literature wavelengths to excite the  $D_2$  transitions [51, 52]. The wavelengths in air are calculated using the following conditions: air temperature 21.3 °C, atmospheric pressure 942.2 HPa, air humidity 33% RH.

**4.3.2.2 Accuracy and precision determination: results** The accuracy of the MI is investigated using different TDL scan speeds: 0.0004 nm/s, 0.01 nm/s, 0.03 nm/s, 0.05 nm/s and 0.10 nm/s. Thereby, the MI shows the best performance, if the TDL is piezoelectrically fine-tuned with 0.0004 nm/s scan speed. It can be shown, that the accuracy of MI decreases with increasing scan speeds.

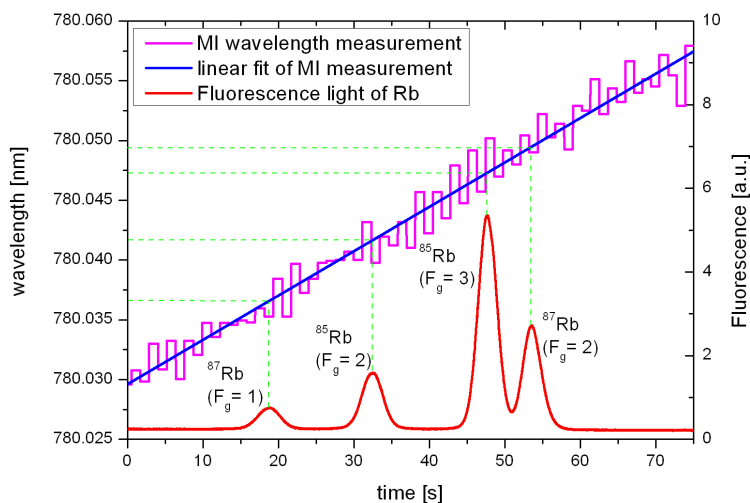


Figure 32: Rubidium spectroscopy using TDL piezoelectrically tuned from 780.030 nm - 780.060 nm with 0.0004 nm/s scan speed. The red line depicts the fluorescence light intensity and the violet line the MI wavelength measurement. The green dashed lines denote the measured wavelengths needed to excite the  $D_2$  transitions.

Fig. 32 shows an example, how the accuracy of the MI for 0.0004 nm/s TDL scan speed is obtained. The red line depicts the fluorescence and the violet line the MI wavelength measurement, which are simultaneously plotted *versus* time. The blue line depicts the linear fit of the MI measurement. The wavelengths at the top of the fluorescence peaks correspond to the wavelengths to excite the  $D_2$  transitions (denoted by the crossings of the green dashed lines with the blue line). For each scan speed, 10 measurements are performed to determine its repeatability (precision).

The determined wavelengths and its deviations from the literature values are listed in table 4. The accuracy and precision of the wavemeter are conservatively estimated. The mean deviation from the literatures within a scan speed is assumed to be the accuracy and the mean standard deviation within a scan speed the precision. The accuracy and precision of the MI for the used scan speeds are summarized in table 5.

Rb D <sub>2</sub> transition	measured wavelength	deviation from literature
<i>0.0004 nm/s scan speed</i>		
<sup>87</sup> Rb (F <sub>g</sub> = 1)	780.037(±0.001) nm	0.001 nm
<sup>87</sup> Rb (F <sub>g</sub> = 2)	780.050(±0.001) nm	0.000 nm
<sup>85</sup> Rb (F <sub>g</sub> = 2)	780.042(±0.001) nm	0.001 nm
<sup>85</sup> Rb (F <sub>g</sub> = 3)	780.048(±0.001) nm	0.001 nm
<i>0.01 nm/s scan speed</i>		
<sup>87</sup> Rb (F <sub>g</sub> = 1)	780.038(±0.001) nm	0.002 nm
<sup>87</sup> Rb (F <sub>g</sub> = 2)	780.056(±0.001) nm	0.006 nm
<sup>85</sup> Rb (F <sub>g</sub> = 2)	780.044(±0.001) nm	0.003 nm
<sup>85</sup> Rb (F <sub>g</sub> = 3)	780.055(±0.001) nm	0.008 nm
<i>0.03 nm/s scan speed</i>		
<sup>87</sup> Rb (F <sub>g</sub> = 1)	780.040(±0.002) nm	0.004 nm
<sup>87</sup> Rb (F <sub>g</sub> = 2)	780.061(±0.002) nm	0.010 nm
<sup>85</sup> Rb (F <sub>g</sub> = 2)	780.045(±0.002) nm	0.004 nm
<sup>85</sup> Rb (F <sub>g</sub> = 3)	780.058(±0.002) nm	0.011 nm
<i>0.05 nm/s scan speed</i>		
<sup>87</sup> Rb (F <sub>g</sub> = 1)	780.042(±0.004) nm	0.006 nm
<sup>87</sup> Rb (F <sub>g</sub> = 2)	780.061(±0.003) nm	0.010 nm
<sup>85</sup> Rb (F <sub>g</sub> = 2)	780.047(±0.004) nm	0.006 nm
<sup>85</sup> Rb (F <sub>g</sub> = 3)	780.059(±0.003) nm	0.012 nm
<i>0.10 nm/s scan speed</i>		
<sup>87</sup> Rb (F <sub>g</sub> = 1)	780.041(±0.008) nm	0.005 nm
<sup>87</sup> Rb (F <sub>g</sub> = 2)	780.062(±0.008) nm	0.011 nm
<sup>85</sup> Rb (F <sub>g</sub> = 2)	780.047(±0.008) nm	0.006 nm
<sup>85</sup> Rb (F <sub>g</sub> = 3)	780.060(±0.008) nm	0.013 nm

Table 4: The measured wavelength of the TDL to excite the D<sub>2</sub> transitions and their deviation from the literature wavelengths.

scan speed	accuracy	precision
0.0004 nm/s	0.001 nm	0.001 nm
0.01 nm/s	0.005 nm	0.001 nm
0.03 nm/s	0.008 nm	0.002 nm
0.05 nm/s	0.009 nm	0.004 nm
0.10 nm/s	0.009 nm	0.008 nm

Table 5: The accuracy and precision of the MI for different TDL scan speeds.

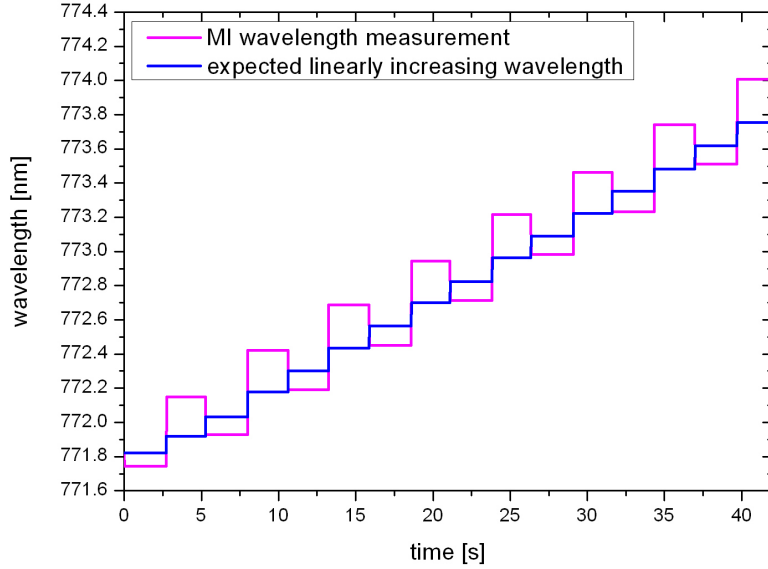


Figure 33: MI measurement with TDL tuned from 771 nm - 774 nm with 0.05 nm/s scan speed. The violet line depicts the experimental wavelength measurement and the blue line illustrates the expected wavelength outputs taking only TDL into account.

### 4.3.3 Analysis of Tunable Diode Laser wavelength measurements at different scan-speeds

As previously mentioned, all MI measurements of the TDL show an initially unexpected behaviour, if the TDL is tuned. Fig. 33 shows a MI measurement, where the TDL is tuned from 771 nm - 774 nm with 0.05 nm/s scan speed. One would expect steadily increasing wavelength outputs (blue line), as the TDL is tuned with +0.05 nm/s. However, the measured wavelengths are alternately shifted to lower and higher values compared to the expected linear output. This fact suggests, that too little respectively too many fringes are produced during a MI measurement. Furthermore, this effect is only observed if the TDL laser is tuned. This following subsection explains, how the speed and direction of the MI cart moving on the track and the TDL scan speed causes this effect.

**4.3.3.1 Fringe formation depending on the directional motion of the cart** Fig. 34 shows a simplified setup of the MI, where the cornercube is replaced by a cart containing two planar mirrors (M1 and M2). A laser beam is split at the beamsplitter BS. Both beams travel different paths ( $\overline{BS, M1}$  and  $\overline{BS, M2}$ ) and hit M1 and M2, where they are send back parallel to its original path and overlap at the observation plane C. L denotes the length of the track, which the cart passes to perform a wavelength measurement.

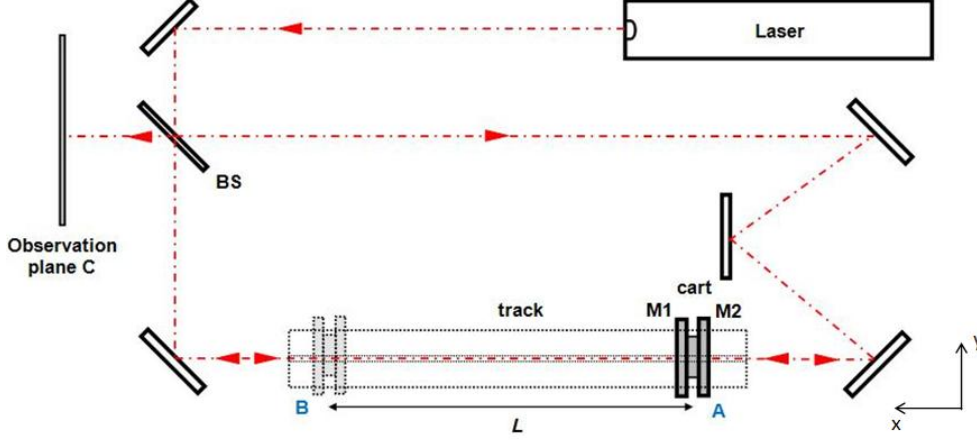


Figure 34: Simplified setup of the MI, where the cornercubes are replaced by two planar mirrors (M1 and M2).

According to eqn (50), phase difference  $\phi$  is given by

$$\phi = \frac{2\pi}{\lambda(t)} 2(\overline{BS, M1} - \overline{BS, M2}) + \Delta\phi \quad (58)$$

with  $\lambda(t) = \lambda_0 + d\lambda/dt \cdot t$ , where  $d\lambda/dt$  is the TDL scan speed. We assume  $\Delta\phi = 0$ , *i.e.* no additional phase shifts to due reflections at the BS. In our case, two positions of the cart are of particular interest (denoted by A and B). Let us assume, that a wavelength measurement is performed where the cart moves with direction from A to B. In this case,  $\phi_+$  is given as

$$\phi_+(t) = \frac{2\pi}{\lambda(t)} (\Delta s_0 + 2vt) \quad (59)$$

where  $\Delta s_0 = 2(\overline{BS, M1} - \overline{BS, M2})$  is the optical path difference  $v$  and the cart speed. The phase difference  $\phi_+$  at A and B are given as

$$A: \quad \phi_+(t=0) = \frac{2\pi}{\lambda_0} \Delta s_0 \quad (60)$$

$$B: \quad \phi_+(t=T) = \frac{2\pi}{\lambda(T)} (\Delta s_0 + 2vT), \quad (61)$$

where  $T$  is the time, which the cart needs to travel distance  $L$  (*i.e.* time to perform one wavelength measurement). Correspondingly, if the cart travels in the opposite direction from B to A,  $\phi_-$  is given by

$$\phi_-(t) = \frac{2\pi}{\lambda(t)} (\Delta s_1 - 2vt) \quad (62)$$

with  $\Delta s_1 = \Delta s_0 + \Delta s_M$  and  $\Delta s_M = 2(2L)$ , where  $(2L)$  takes into account that the mirrors of both arms are moved simultaneously. In this case, the phase difference  $\phi_-$  at A and B are given as

$$B : \quad \phi_-(t=0) = \frac{2\pi}{\lambda_0} \Delta s_1 \quad (63)$$

$$A : \quad \phi_-(t=T) = \frac{2\pi}{\lambda(T)} (\Delta s_1 - 2vT). \quad (64)$$

According to eqn (52), the time-averaged intensity  $\bar{I}$  in the observation plane C is proportional to the cosine of  $\phi$ . One fringe is counted if a full period of the cosine has passed, *i.e.*  $\cos(2\pi) \cong$  one fringe. Therefore, if the cart starts at A and ends at B, the number of fringes  $(\#fringes)_+$  counted is given by

$$(\#fringes)_+ = \frac{\phi_+(t=T) - \phi_+(t=0)}{2\pi}, \quad (65)$$

whereas for the other case (from B to A) the number of fringes counted in C is given by

$$(\#fringes)_- = \frac{\phi_-(t=T) - \phi_-(t=0)}{2\pi}. \quad (66)$$

The total difference of fringes  $\Delta fringes$  due to the directional dependent movement of the cart (*i.e.* A to B, B to A) is given as

$$\Delta fringes = |(\#fringes)_+ - (\#fringes)_-| \quad (67)$$

$$= \left| \frac{\phi_+(t=T) - \phi_+(t=0)}{2\pi} - \frac{\phi_-(t=T) - \phi_-(t=0)}{2\pi} \right|. \quad (68)$$

By inserting eqn (60,61,63,64),  $\Delta fringes$  can be expressed as

$$\Delta fringes = \left| (2\Delta s_0 + \Delta s_M) \left( \frac{1}{\lambda(t=T)} - \frac{1}{\lambda(t=0)} \right) \right|. \quad (69)$$

As one can see,  $\Delta fringes$  depends on the optical path differences  $\Delta s_0$  and  $\Delta s_M$ , TDL scan speed  $(d\lambda/dt)$  and the cart speed  $v$  (expressed as  $T = \Delta s_M/2v$ ). Eqn (69) shows, that the effect diminishes ( $\Delta fringes = 0$ ) if  $(d\lambda/dt) = 0$  (*i.e.* fixed wavelength), since  $1/\lambda(t=T) - 1/\lambda(t=0) = 0$ . If  $\Delta s_0$  and  $\Delta s_M$  are known,  $\Delta fringes$  can be predicted accurately for different TDL scan speeds by measuring  $T$ . This is the content of the next subsection.

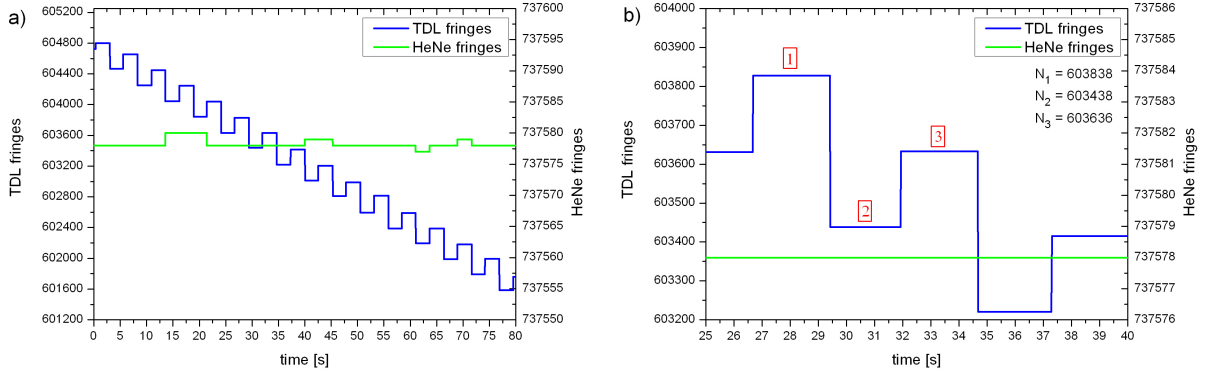


Figure 35: a) MI measurement with TDL tuned from 772 nm - 776 nm with 0.05 nm/s scan speed. TDL and HeNe fringes are plotted *versus* time. b) enlarged section of panel a).

**4.3.3.2 Analysis of  $\Delta$ fringes at different cart speeds and TDL scan speeds** Fig. 35a) illustrates how  $\Delta$ fringes is obtained from a MI measurement. This example is performed using TDL tuned from 772 - 776 nm with 0.05 nm/s scan speed and 0.09 m/s cart speed. The TDL (blue line) and HeNe fringes (green line) are plotted *versus* time. As the TDL is tuned with +0.05 nm/s scan speed, the TDL fringes decreases overall. As one can see, the HeNe fringes are not affected by this effect because of its fixed wavelength and thus, exhibit a constant value. However, small fluctuations of HeNe fringes are possible due to misalignment of the MI. Fig. 35b) shows an enlarged section of Fig. 35a), where three measurements are considered more closely (denoted by red numbers). The number of TDL fringes of the considered measurements are displayed in the Figure ( $N_1$ ,  $N_2$  and  $N_3$ ). Measurements 1 and 3 are performed, where the cart moves from A to B (according to Fig. 34), whereas in measurement 2 the cart moves from B to A.

The difference of fringes between the measurements 1 and 2 is equal to  $\Delta N_{12} = N_2 - N_1 = -400$  fringes. Thereby,  $\Delta N_{12}$  contain two contributions. The first contribution is  $\Delta$ fringes due to the effect described above. The second contribution is due to the fact, that the TDL is tuned with +0.05 nm/s scan speed, which causes a reduction of the produced fringes,  $\Delta$ tuning. +0.05 nm/s scan speed corresponds to a loss of about 40 fringes per second. Since the time  $T$  to perform one wavelength measurement in this example is 2.5 s,  $\Delta$ tuning = -100 fringes. With

$$\Delta N_{12} = \Delta \text{fringes} + \Delta \text{tuning}, \quad (70)$$

$\Delta$ fringes is -300 fringes in this example. The minus sign implies that measurement 2 has counted 300 fringes less than measurement 1 due to the effect described above. The same procedure holds for  $\Delta N_{23} = N_3 - N_2 = 198$  fringes, with same  $\Delta$ tuning. In this

case,  $\Delta fringes$  is +298 fringes, where the plus sign concludes that measurement 3 has counted 298 fringes more than measurement 2.

According to eqn (69), the optical path lengths  $\Delta s_0$  and  $\Delta s_M$  must be determined to predict  $\Delta fringes$  for different combinations of cart speed and TDL scan speed. Since the wavelength of the HeNe laser is known very precisely [50],  $\Delta s_M$  can be accurately determined by using eqn (53). For our setup of the MI, eqn (53) is modified to

$$N_{HeNe} = \frac{2(2L)}{\lambda_{HeNe}} = \frac{\Delta s_M}{\lambda_{HeNe}}. \quad (71)$$

With  $\lambda_{HeNe} = 632.8306$  nm and  $N_{HeNe} = 737578$  fringes, one obtains

$$\Delta s_M = 23.3380964143 \text{ cm}. \quad (72)$$

To determine  $\Delta s_0$ , measurements with three different TLD scan speeds at four different cart speeds are performed with five repetitions. The  $\Delta fringes$  are extracted from each measurement and illustrated in Fig. 36 (colored points). The measured  $\Delta fringes$  are fitted with eqn (69), which yields the best value for  $\Delta s_0$ :

$$\Delta s_0 = 44.690(\pm 0.865) \text{ cm}. \quad (73)$$

With (72) and (73),  $\Delta fringes$  is predicted as denoted with the violet line in Fig. 36. The accurate agreement of the measured with the calculated  $\Delta fringes$  shows that the effect described above can be reliably explained with eqn (69). It can be shown, that at a fixed cart speed,  $\Delta fringes$  increases with increasing scan speeds. Conversely at a fixed scan speed,  $\Delta fringes$  decreases with increasing cart speed.

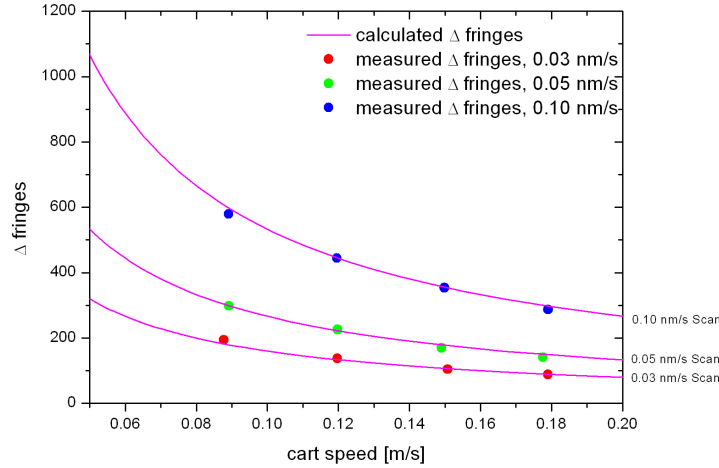


Figure 36: Measurement and prediction of  $\Delta fringes$  at different cart and TDL scan speeds.

## 5 Glassy sucrose experiment

As previously mentioned in section "1.3 Preliminary results", Zobrist *et al.* (2011) showed that organic aerosol particles in the atmosphere might be in the glassy state and thus, cause the water uptake respective release of these particles to be impeded or completely inhibited. This is reflected in an impeded growth and shrinking of the particle as the relative humidity changes (see Fig. 2b, solid colored lines). Furthermore, Zobrist *et al.* developed a spherical shell diffusion model (eqn (1) and (2)), which calculates the experimental results very accurately (red dotted line in Fig. 2b). This diffusion model predicts that the concentration within the sucrose particle is radial inhomogeneous (see Fig. 2d). However, direct experimental evidence for these radial diffusion profiles were missing.

Due to a previous study by Ray and Nandakumar (1995), the shift of the Mie resonances with growth are different comparing a homogeneous to an inhomogeneous particle. For a homogeneous particle which grows, the shift of these resonances with size change are the same for the TM and TE resonances, whereas for a core shell structured sphere the shift for the TM mode differs from the one of the TE mode [54]. This is illustrated in Fig. 37. If sucrose particles under atmospheric conditions were really glassy and thus radial inhomogeneous in concentration like the diffusion model predicts, it should be reflected in different shifts of the TE and TM resonances of a growing sucrose particle. In order to prove the validity of the diffusion model and the existence of a radial inhomogeneous profil of the glassy sucrose, first experimental data of sucrose particles obtained by using "High resolution Mie resonance spectroscopy" are provided in this master's thesis.

The general course of the experiment is described in section "5.1 Preparation and raw data". LED spectra obtained by using "White light Mie resonance spectroscopy" are used to estimate the initial radius of the sucrose particle and its change during the experiment. Knowledge about the temperature and relative humidity in the EDB are used to model the growth of the particle and compared with the experimental results. This is given in section "5.2 LED spectra analysis". TDL spectra are recorded by using "High resolution Mie resonance spectroscopy" and discussed in section "5.3 TDL spectra analysis". A summary of the experiment can be found in "5.4 Summary of the experiment".

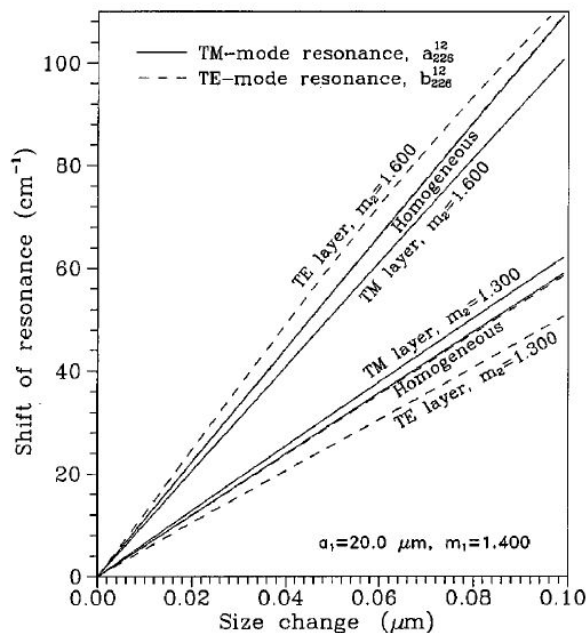


Figure 37: Calculated spectral shifts of TE and TM mode resonances (*i.e.* differences between their initial and their final positions in wave numbers) as functions of size change that is due to homogeneous growth and layer formation (*i.e.* inhomogeneous growth) on a homogeneous droplet of size  $a_1 = 20.0 \mu\text{m}$  and refractive index  $m_1 = 1.400$ . For the upper set of curves, the size change occurs because of the addition of a component of refractive index  $m_2 = 1.600$ , whereas for the lower set  $m_2 = 1.300$  [54].

## 5.1 Preparation

Sucrose ( $\text{C}_{12}\text{H}_{22}\text{O}_{11}$ ) was purchased from Acros organics (Belgium) with purity  $\geq 99.7\%$ . Deionized water purified in a Milli-Q water purification apparatus (Resistivity  $\geq 18.2 \text{ M}\Omega \text{ cm}$ ) were used to prepare an aqueous solution with 5 wt% sucrose, which was injected into the EDB with the particle generator.

In order to obtain a highly homogeneous sucrose particle containing little water, it has been slowly dried at room temperature ( $T = 291 \text{ K}$ ) from 78% RH down to 0% RH in 15 hours and then kept at this experimental conditions for 3 days. Previous experiments performed by Zobrist *et al.* (2011) have shown, that the particle is then in a glassy state and contains only little water under this experimental condition [1]. To observe a slow inhomogeneous growth of the glassy particle upon humidification, it is cooled down to 234 K where the actual experiment starts.

Panels a) and b) of Fig. 38 show the raw data of the drying of the particle at room temperature ( $T = 291 \text{ K}$ ) and the subsequently cooling to  $T = 234 \text{ K}$ . The sudden rise of the temperature before cooling is due to the switch from the Julabo thermostat to

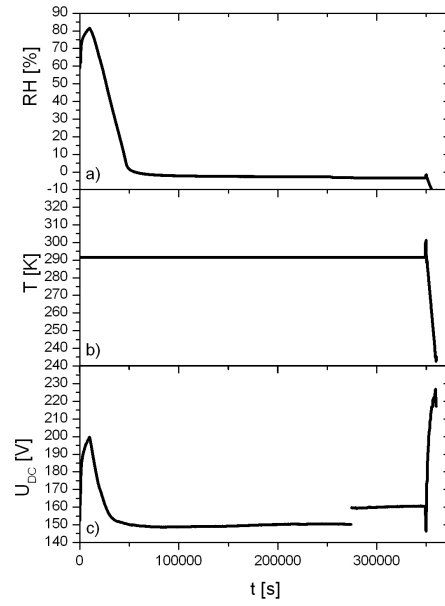


Figure 38: Preparation of the experiment. Panels a) to c) show RH, temperature and  $U_{DC}$  mass of the sucrose particle as a function of time.

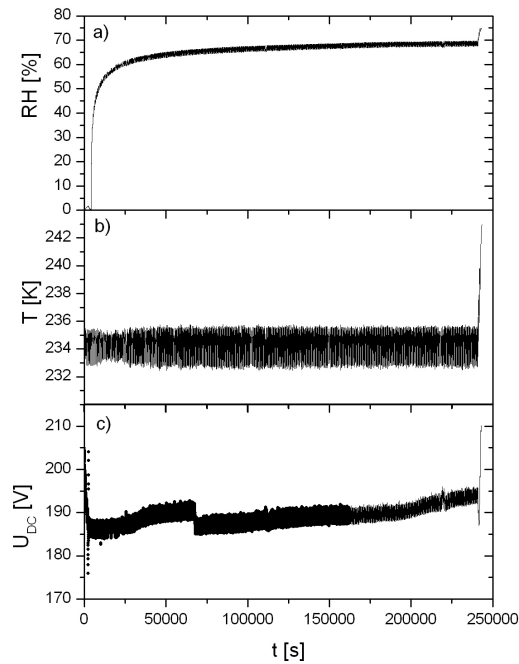


Figure 39: Course of the actual experiment. Panels a) to c) show RH, temperature and  $U_{DC}$  mass of the sucrose particle as a function of time.

the Huber thermostat to achieve subfreezing temperatures (see section "3.1.3 Cooling system"). One notices that the RH value drops below 0 RH for  $T = 234$  K, which implies that the RH sensor calibration is not valid at 234 K (see section "3.1.5 Relative humidity measurement"). Panel c) shows the  $U_{DC}$  voltage (proportional to the mass) necessary to compensate the gravitational force. As the RH is decreased ( $t = 0$  s - 50'000 s), the (liquid) particle monotonously shrinks in mass and radius until it becomes glassy and keeps a constant mass and radius ( $t \geq 50'000$  s). At  $t = 270'000$  s, the gas flow of  $N_2$  has been increased to boost the drying process, which causes a rapid rise in  $U_{DC}$ . The apparent rise in  $U_{DC}$  upon cooling at  $t = 350'000$  s is due to an increasing misalignment of the camera used for feedbacking  $U_{DC}$ .

Fig. 39 shows the course of the actual growth experiment, which lasts almost 3 days. The temperature was kept constantly at 234 K with ( $\pm 1$  K accuracy) during the whole experiment, as shown in panel a). Panel b) illustrates the humidification process. Since the RH sensor is not calibrated at low temperatures, an alternative way for humidification is used at  $T = 234$  K. the gas flow is switched from dry  $N_2$  to  $N_2/H_2O$  mixture with the  $H_2O$  partial pressure being a factor two or higher than ice saturation. Ice condenses at the surface of the inlet glass tube where it encounters the coldest temperature within the setup (see Fig. 9), locking the relative humidity inside the EDB to the vapour pressure of ice at  $T = 234$  K. RH was then calculated according to Murphy and Koop [55]. By forming a layer of ice on walls of the inlet, the gas-phase water partial pressure approaches slowly the value above ice, *i.e.* about 68% RH with respect to liquid water. From the  $U_{DC}$  measurement shown in panel c) follows, that the mass of the glassy sucrose particle increases only slightly due to the impeded water uptake, as the RH increases. At  $t = 60'000$  s, the gas flow of  $N_2/H_2O$  mixture has been decreased, which causes a sudden fall in  $U_{DC}$ . This will be discussed in section "5.2 LED spectra analysis".

## 5.2 LED spectra analysis

LED Mie resonance spectra obtained by using "White light Mie resonance spectroscopy" are recorded during the whole experiment. The spectra are typically taken every minute with 10 s exposure time. Fig. 40 shows a LED spectrum recorded at the beginning of the humidification process at  $T = 234$  K, which is smoothed by application of an FFT filter. Due to the limited resolution of the spectrograph-OMA combination (about 0.5 nm), only broad resonances (*i.e.* higher order resonances) are observed.

Since the refractive index  $m$  of sucrose is well known [56], the radius of the particle can be approximatly determined by [46]

$$r = \frac{\Delta x}{2\pi} \left( \frac{\lambda_{n+1}^l \cdot \lambda_n^l}{\lambda_n^l - \lambda_{n+1}^l} \right), \quad (74)$$

where  $\lambda_{n+1}^l$  and  $\lambda_n^l$  are wavelengths associated with two consecutive modes of resonance, which are determined directly from a resonance spectrum.  $\Delta x$  is the size parameter

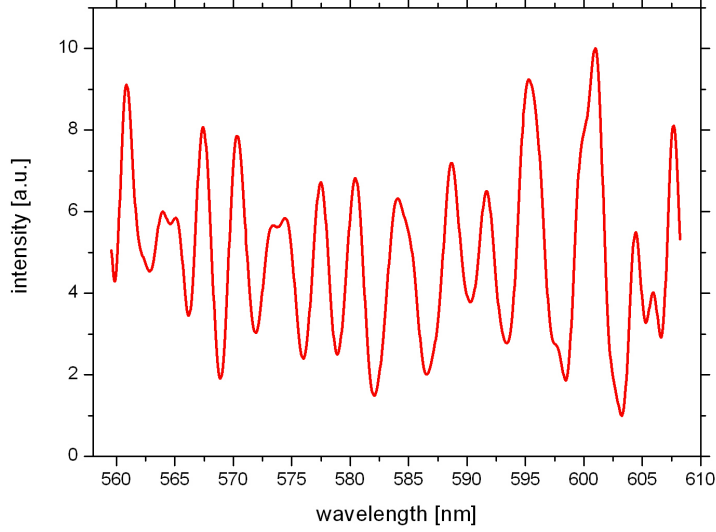


Figure 40: LED spectrum of the sucrose particle, which is smoothed by application of an FFT filter.

spacing between consecutive resonance peaks in index number  $n$ ,  $\Delta x = x_{n+1}^l - x_n^l$ , and given as a function of the refractive index  $m$  [57]:

$$\Delta x = \frac{\arctan(m^2 - 1)^{1/2}}{(m^2 - 1)^{1/2}}, \quad (75)$$

if the particle is larger than a few micrometers and only broader resonance peaks are considered [46]. Therefore, one obtains  $r_0 = 13.749 \mu\text{m}$  as initial radius of the sucrose particle (*i.e.* the radius at the beginning of the humidification process at  $T = 234\text{K}$ ).

As the particle grows upon humidification, the resonance peaks shift to higher wavelengths, which is illustrated in the resonance spectra with color-coded intensity in Fig. 41b). A maximum located at 580 nm in the first spectrum is chosen and followed during its shift (panel c). Using eqn (41), the change of radius can be calculated, if the initial radius ( $r_0$ ) is known. This is illustrated in panel d). During three days of humidification at  $T = 234 \text{ K}$ , the resonance peak located at 580 nm shifted +2.8 nm and thus, the radius increased by  $0.070 \mu\text{m}$ . The sudden rise of the radius at  $t = 67'000 \text{ s}$  is correlated to an abrupt change of the resonance spectra (see panel b),  $t = 67'000 \text{ s}$ ). Its origin is not completely investigated yet at the current state of research. A possible explanation could be that the high order resonances observed in the LED spectra become very sensitive to the inhomogeneity of the particle at this particular shell thickness at  $t = 67'000 \text{ s}$ .

In order to model the concentration profil of the sucrose particle, the spherical shell

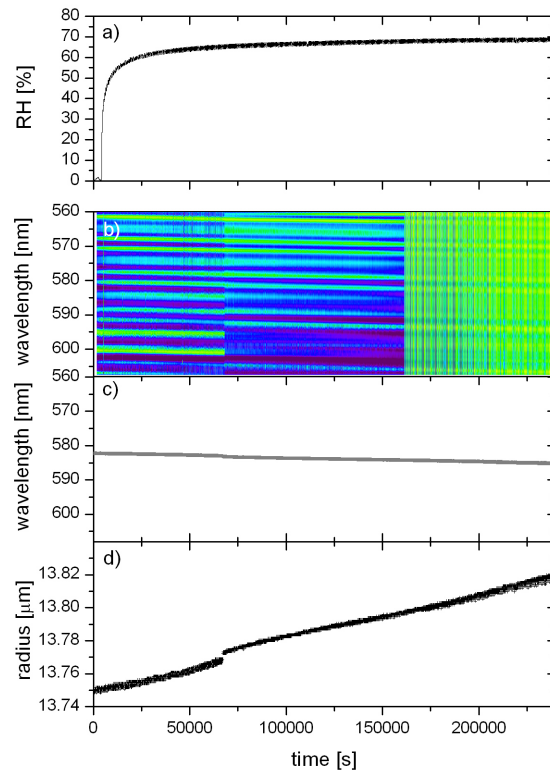


Figure 41: Temporal evolution of the sucrose experiment. Panel a) shows the RH as illustrated in Fig. 39a). Panel b) shows the corresponding resonance spectra, with color-coded intensity. The resonance spectra change abruptly at  $t = 67'000$  s due to a sudden shift of the resonances. The intensity change at  $t = 160'000$  s is due to suboptimal illumination of the sucrose particle (see section "3.2.4 White light Mie resonance spectroscopy"). Panel c) shows the tracking of the resonance peak located at 580 nm. The corresponding radius is calculated by using eqn (41) and displayed in panel d). The radius changes abruptly at  $t = 67'000$  s correlated to the abrupt change of the resonance spectra at the same time. A possible explanation is given in the text above.

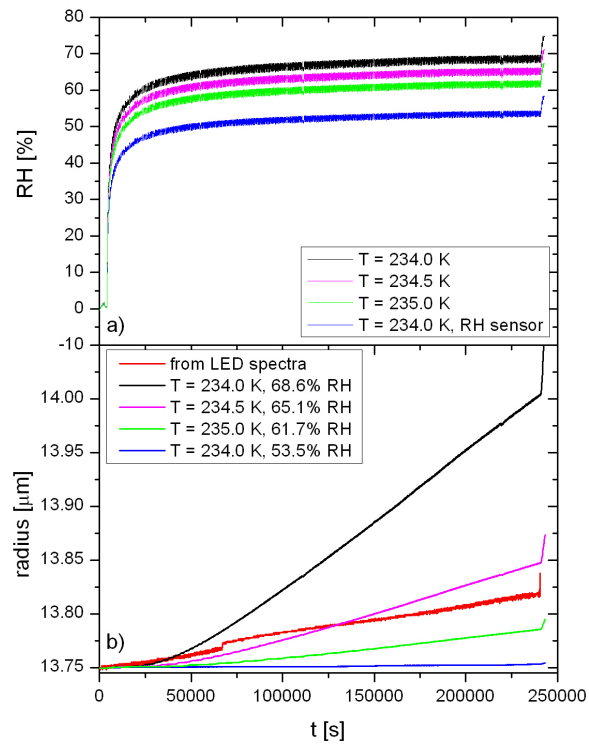


Figure 42: Radius modelling under different experimental conditions. Panel a) depicts four possible RH and temperatures in the immediate vicinity of the sucrose particle due to an inhomogeneous temperature distribution within the EDB. Panel b) shows the corresponding radius determined by using the diffusion model and compared with the radius obtained from the LED spectra (red line).

diffusion model developed by Zobrist *et al.* (2011) together with the parameterization of the temperature and humidity dependence of diffusivity of water in sucrose is used to calculate the expected change of radius during the experiment by taking the initial size of the particle ( $r_0$ ) and experimental conditions (*i.e.* relative humidity and temperature). This is illustrated in Fig. 42, where the black line depicts the modelled change of radius (at  $T = 234$  K), and the red line the change of radius obtained from the LED spectra. The predicted radius significantly exceeds the measured one. This could be due to an overestimation of the RH to which the particle is exposed. Therefore, the RH obtained from the RH sensor (note that it is not calibrated at  $T = 234$  K) is used to model the radius (blue line in panel b), which indicates no growth of the particle. This case is excluded, since the experimental result obtained from the LED clearly indicates a growth of the particle. Furthermore, previous studies on the characteristics of the EDB have shown [58], that the temperature within the EDB chamber is not completely homogeneous. Therefore, we assume that the particle may be up to 1 K warmer than

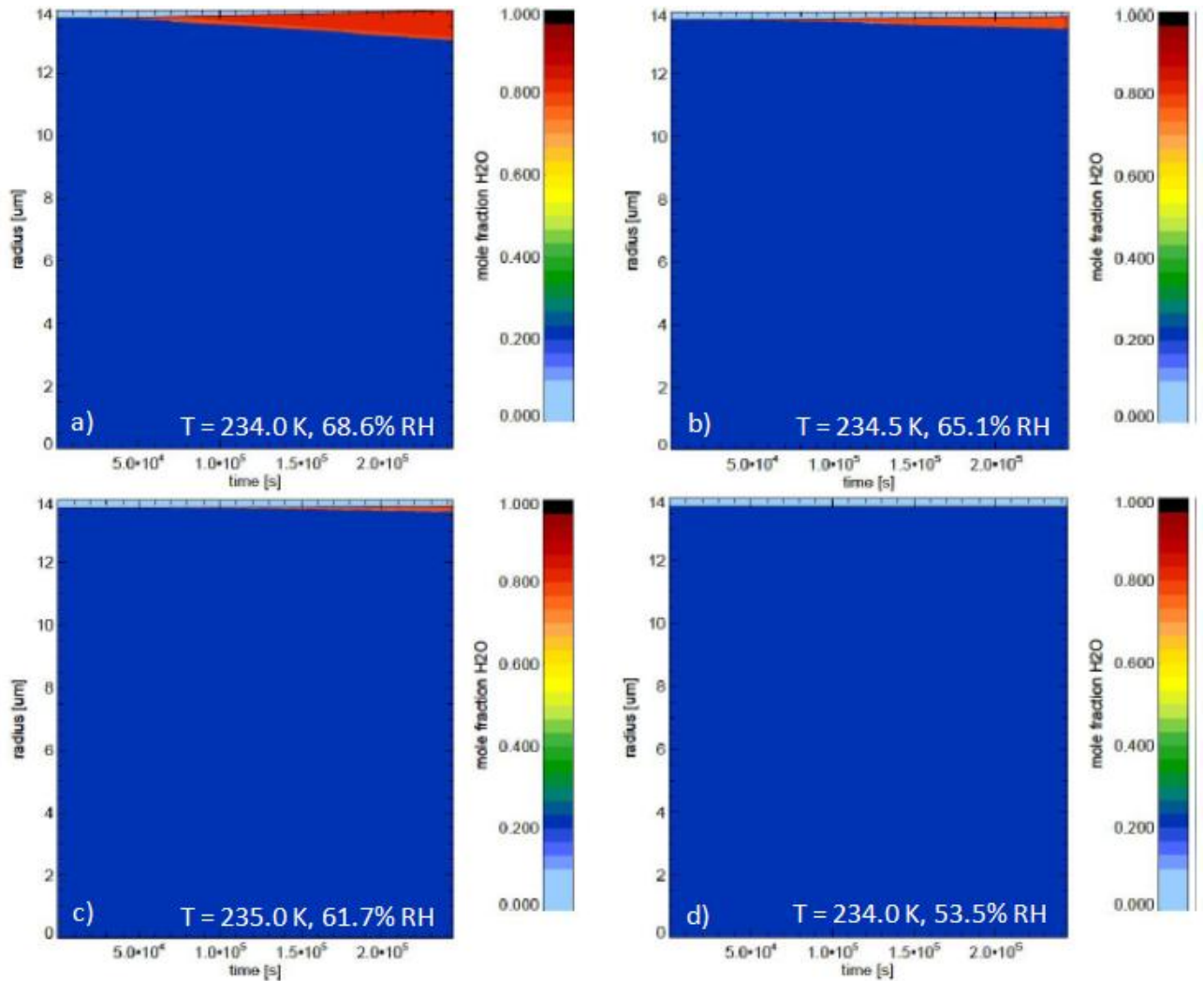


Figure 43: Modelled radial concentration profile inside the particle under the experimental conditions (*i.e.* RH and temperature) given in Fig. 42.

the temperature measured by the sensor in thermal contact to the cooling liquid. As explained, the vapor pressure inside the trap is locked to the one of ice at the temperature measured by the sensor. However, if the particle is warmer than the ice, the RH it is exposed to is lower than the one calculated above. The RH is calculated for  $T = 234.5$  K (denoted by the violet line in panel a) and  $T = 235$  K (denoted by the green line in panel a) and the corresponding radius are illustrated in panel b). The radius predicted for a particle temperature of  $T = 234.5$  K and hence  $\text{RH} = 65.1\%$  (violet line) yields the closest approximation to the radius obtained from the LED spectra.

The associated concentration profiles are shown in Fig. 43, where the particle's radial concentration profile is plotted as function of time for the considered cases. All concentration profiles illustrate a homogeneous particle containing an about 20% of amount of water (dark blue area). Panels a) to c) indicate a inhomogeneous growth of the particle

by forming a thin water layer on the surface of the particle, which grows into the particle with time depending on RH and temperature. As mentioned above, the predicted radius with  $T = 234.5$  K and  $RH = 65.1\%$  yields the best match with the measured radius. Therefore, panel b) provides the most approximate representation of the sucrose particle among the four modelled concentration profiles, under the assumption that the liquid-phase diffusion model provided by Zobrist *et al.* (2011) is valid.

Please note that the determination of the initial radius  $r_0$  and its evolution upon growing are obtained based on the assumption, that the particle is homogeneous. Consequently, small deviations from the real size are expected, if the sucrose particle is inhomogeneous upon growing. The diffusion model predicts an inhomogeneous sucrose particle upon humidification by forming a thin water layer on the surface of the particle. Whether the particle really becomes radially inhomogeneous or not, is discussed in the next section "5.3 TDL spectra analysis".

### 5.3 TDL spectra analysis

TDL Mie resonance spectra obtained by using "High resolution Mie resonance spectroscopy" are recorded during the whole humidification process at  $T = 234$  K. The TDL is tuned from 765 - 781 nm with 0.02 nm/s scan speed. Therefore, it takes about 13 minutes to record one TDL spectrum. Thereby, TDL spectra are recorded such that a spectrum shows pure TE, TM or both TE and TM resonances. This can be achieved by tuning the half-wave plate (see Fig. 18) to  $45^\circ$  (TM mode),  $90^\circ$  (TE mode) or  $67.5^\circ$  (TE and TM mode).

Fig. 44 shows the resonance spectra of TE (black line) and TM mode (red line) of the sucrose particle with initial radius  $r_0 = 13.749$   $\mu\text{m}$ . In each spectrum, resonances of three different orders (*i.e.* mode orders) are observed (denoted by violet arrows), which appear three times. At the current state of research, their mode and order number are not identified yet.

The glassy particle slowly grows upon humidification, which causes all Mie resonances to shift to higher wavelengths (according to eqn (40)). Two TE and TM resonances of low respective higher order are tracked during the growth of the particle, which are denoted by capital letters in Fig. 44. (Interestingly, we do not observe the sudden shift at about  $t = 60'000$  s seen in the LED spectra, compare Fig. 41.)

Fig. 45a) shows how the considered resonances evolve as the particle grows. The resonances shift overall almost linearly to higher wavelengths. The displacement of the resonances between  $t = 125'000$  s and  $175'000$  s occur in all observed resonances. Thus, it can be assumed that this occurrence is an artefact of the experiment. There are only few data of the low order TM resonance (denoted as C in Fig. 44), since its intensity is very weak and thus difficult to track.

Fig. 45b) shows the same data but plotted as resonance shifts relative to their initial positions at  $t = 0$  s. As one can see, the TE resonances (dark and light green dots) shift

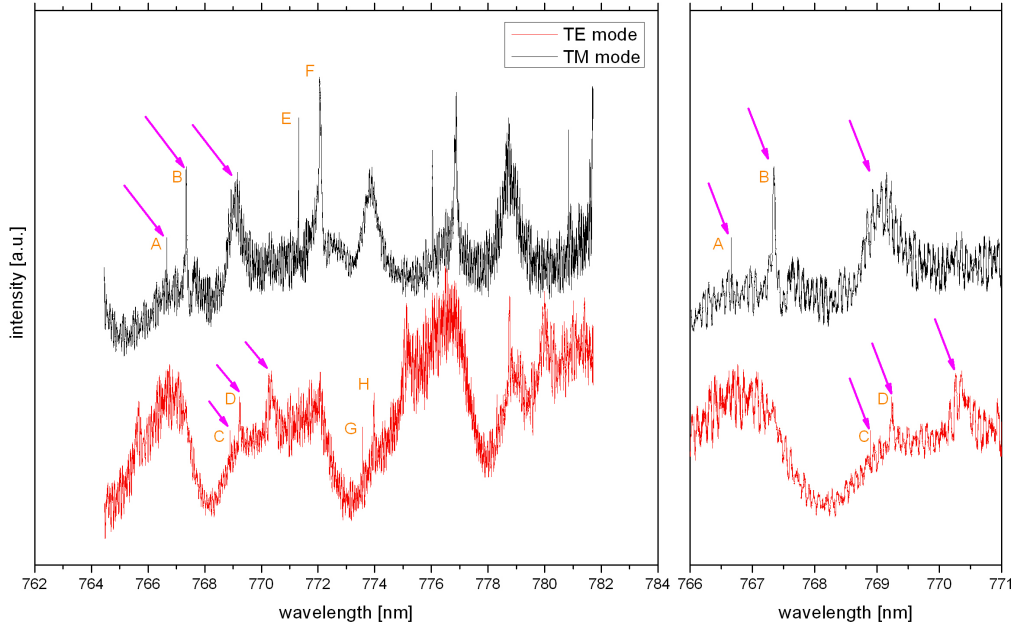


Figure 44: TDL resonance spectra of sucrose particle recorded using TDL with 0.02 nm/s scan speed. Black line shows the pure TE resonances, whereas the red line the pure TM resonances. Resonances of three different (unknown) orders are denoted with violet arrows. The capital letters denote the peaks, which are tracked as the particles grows upon humidification (see Fig. 42). Right panel shows the resonances of different orders in an enlarged view.

slightly different from the TM resonances (dark and light blue dots). The displacement of the shifts for  $t = 125'000$  s -  $175'000$  s is the same as in Fig. 42b). Moreover, the resonance shifts of TE and TM resonances merge at about  $t = 150'000$  s and differ again for  $t \geq 150'000$  s, indicating an oscillatory behaviour, which Ray and Nandakumar (1995) have predicted for increasing shell thickness [54]. This oscillatory behaviour is better illustrated in Fig. 46, where the relative shift between TE and TM resonances (violet dots and light blue crosses) and between different mode orders (dark green dots and dark blue crosses) are plotted. The relative shifts between TE and TM resonances show clearly an oscillatory behaviour, which indicates that the glassy sucrose particle grows inhomogeneously. However, relative shifts between different mode order do not show oscillatory behaviour. This suggests that the considered resonances (denoted capital letters in Fig. 45a) are not of first and second orders, since one would expect a more pronounced difference in shift between modes of first and second order [59].

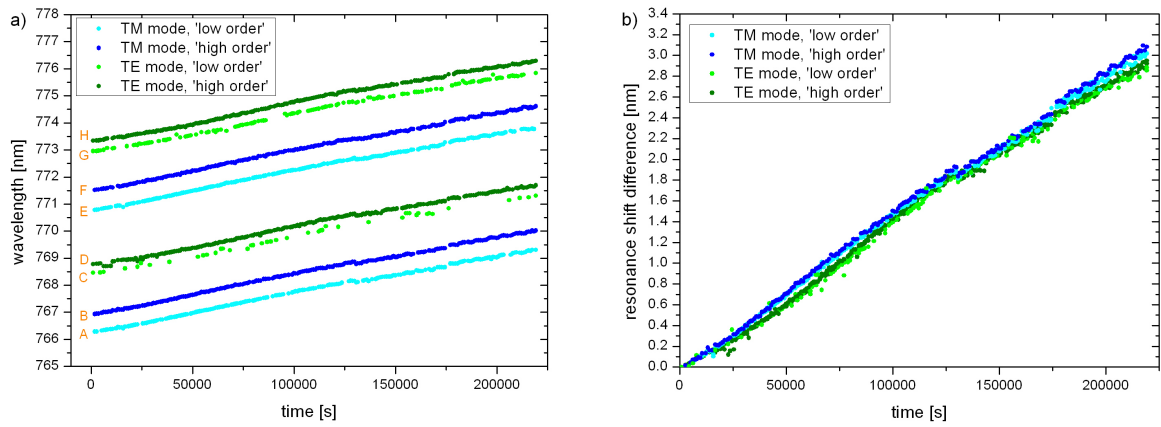


Figure 45: Resonance shift as a function of time. Panel a) shows the shift of the resonances denoted by capital letters in Fig. 44. Panel b) shows the same resonance shifts from their initial positions.

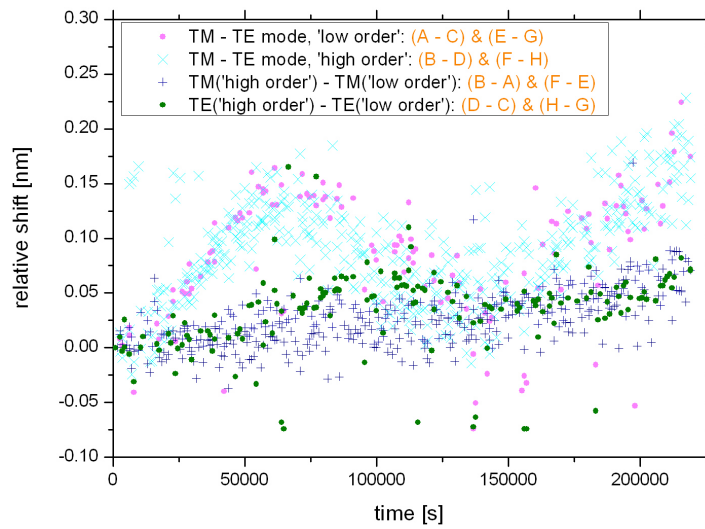


Figure 46: Relative shift between TE and TM resonances and between different mode orders. Thereby, the same resonances as in Fig. 45a) are considered.

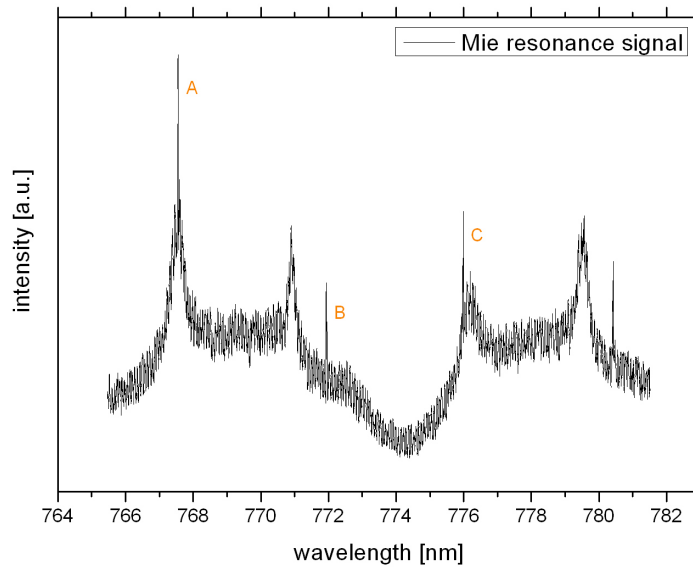


Figure 47: TDL resonance spectrum of an aqueous alpha-ketoglutaric acid particle the using TDL with 0.04 nm/s scan speed.

As one can see in Fig. 46, the spread of the TDL data recorded with 0.02 nm/s TDL scan speed is about 0.05 nm. This greatly exceeds the accuracy and precision of the Michelson interferometer at 0.03 nm/s scan speed, which is 0.008 nm (accuracy) and 0.002 nm (precision) according to table 5. In order to understand the reason of this spread, TDL spectra of an homogeneous and evaporating particle (alpha-ketoglutaric acid) at 303 K is recorded (vapor pressure at 303 K:  $5.1 \times 10^{-6}$  Pa). Fig. 47 shows the TDL Mie resonance spectrum of the particle. Six resonance peaks are observed, whereof three peaks (denoted by capital letters in Fig. 47) are tracked during the 7-hour experiment (see Fig. 48a). All resonance peaks shifted continuously to lower wavelengths. The shift is linear and arises from the shrinking of the particle due to evaporation, which is approximated by a linear fit (red line in Fig. 48a). Analogous to Fig. 46, the relative shift between the considered peaks are plotted in Fig. 48b). Since alpha-ketoglutaric acid is homogeneous, all resonances should shift in the same way and the relative shift should be within the threshold value of 0.01 nm limited by the resolution of the Michelson interferometer (see table 5). However, the spread of the TDL spectra is in the same magnitude (about 0.05 nm, denoted by red dashed line) as the one obtained from the glassy sucrose particle. Further investigations are necessary to understand the source of the spread, which are not performed in this thesis.

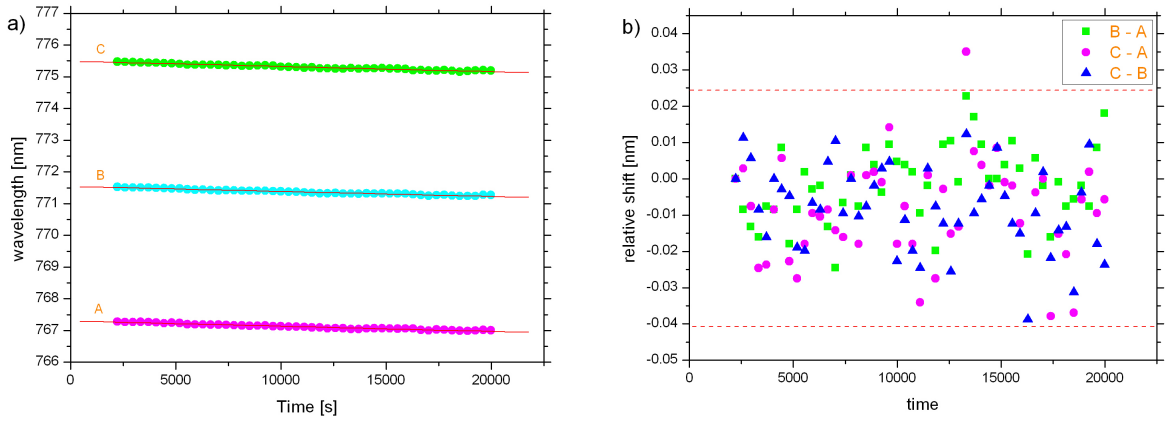


Figure 48: Resonance shift as a function of time. Panel a) shows the shift of the resonances denoted by capital letters in Fig. 47. Panel b) shows the relative shift between the resonance peaks considered in panel a).

## 5.4 Summary of the sucrose experiment

A sucrose particle stored in the EDB is investigated at (measured)  $T = 234$  K, which was dried initially at 291 K from 78% RH down to 0% RH. The particle is humidified for three days by locking the relative humidity inside the EDB to the vapour pressure of ice at  $T = 234$  K, *i.e.* about 68% with respect to liquid water.

The initial radius  $r_0$  of the particle and its temporal change is determined from the LED spectra with the assumption, that the particle grows inhomogeneous. The radius increases linearly with a abrupt rise at  $t = 67'000$  s (see Fig. 41d), which is not fully investigated at the current state of research. Furthermore, the liquid-phase diffusion model developed by Zobrist *et al.* (2011) is used to calculate the radius of the particle with known experimental conditions (*i.e.* RH and temperature), which is illustrated in Fig. 42. Thereby, RH and temperature are varied such that the modelled radius approximates the experimental obtained one the best. As a conclusion, the diffusion model predicts a inhomogeneous growth of the particle by forming a thin water layer on the particle's surface (see Fig. 43b).

During the experiment, TDL spectra are recorded and the shift of resonances are evaluated (see Fig. 45a). In agreement with the LED spectra analysis, the resonances shift linearly to higher wavelength indicating a linear increase of the particle's radius. However in contrast to the LED spectra, an abrupt change of the resonance shifts is not observed at  $t = 67'000$  s. A possible explanation could be that the high order resonances observed in the LED spectra become very sensitive to the inhomogeneity of the particle at this particular shell thickness at  $t = 67'000$ s, whereas the lower order resonances obtained from the TDL spectra are insensitive. From the TDL spectra analysis,

one obtains the first experimental evidence (see Fig. 46) that a sucrose particle at low temperature becomes inhomogeneous upon humidification, based on the comparison of the observed spectral shift with calculated spectral response as done in the study by Ray and Nandakumar (1995) [54]. Therefore, this measurement supports the statement that sucrose particles at low temperature are in a glassy state and the model of Zobrist *et al.* is able to at least qualitatively predict the inhomogeneity upon humidification. Quantitative comparison of the experimental results are awaiting Mie-calculations for a core-shell particle, which are not performed in this study.

## 6 Conclusions and outlook

In this master's thesis, the experimental methods are developed in order to study microparticles in glassy state, which are stored in an EDB. A high resolution tunable diode laser is used to perform Mie resonance spectroscopy with high resolution. Furthermore in order to assign the measured resonance peaks to wavelength and to enable comparison with Mie calculations, a Michelson Interferometer based wavemeter is built to determine the wavelength of the Tunable Diode Laser steadily. Accuracy and precision, and other characteristics of the Michelson Interferometer are analysed in detail.

First experiments on the internal concentration gradients in a sucrose particle upon humidification by using the newly developed method is performed and discussed in this thesis. Thereby, the experimental results obtained from the analysis of the TDL Mie resonance spectra indicate the development of a liquid aqueous shell on a glassy core of the sucrose particle at 234 K upon humidification. This finding supports the statement, that sucrose particles at low temperature under dry conditions are in glassy state as suggested by Zobrist *et al.* (2011) [1].

In principle, it should be possible to determine the size and refractive index, and model the concentration profil of the sucrose particle with the informations obtained from the high resolution Mie resonance spectroscopy. Therefore, it is crucial to gain informations about the mode and order number of the measured resonances, which are still unknown in the current state of research. Future investigations should allow an unambiguous assignment of the measured resonances, which would allow to size a particle and probe its concentration profil within minutes.

## 7 Acknowledgements

I would like to acknowledge all who have contributed to the completion of this thesis. Especially I would like to thank Prof. Dr. Andreas Schilling and Prof. Thomas Peter for giving me the opportunity to perform this thesis. My very special thanks go to Dr. Karl Ulrich Krieger for his experimental and theoretical support, his supervision and for his guidance for developing the Michelson Interferometer and the High resolution Mie resonance spectroscopy, and the performance of the glassy sucrose experiment. I am very grateful to Edwin Hausammann for his support in developing the Michelson Interferometer. I would like to thank Dr. Andrew Huisman, Dr. Claudia Marcolli and PhD student Daniel Lienhard for interesting and fruitful discussions and also the rest of the group for the pleasant time.

## Bibliography

- [1] B. ZOBRIET ET AL., *Do atmospheric aerosols form glasses*; Atmos. Chem. Phys., 2008, **8**, 5221-5244.
- [2] MIHÁLY PÓSFAL AND PETER R. BUSECK, *Nature and Climate Effects of Individual Tropospheric Aerosol Particles*; Annu. Rev. Earth Planet. Sci., 2010, **38**, 17-43.
- [3] B. ZOBRIET ET AL., *Ultra-slow water diffusion in aqueous sucrose glasses*; Phys. Chem. Chem. Phys., 2011, **13**, 3514-3526.
- [4] U. K. KRIEGER ET AL., *Supercooling of single H<sub>2</sub>SO<sub>4</sub>/H<sub>2</sub>O aerosols to 158K: No evidence for the occurrence of the octahydrate*; Geophys. Res. Lett., 2000, **27**(14), 2097-2100.
- [5] D. LIENHARD, *Glass Formation in Aerosols*; Master's Thesis, ETH Zürich, 2010.
- [6] U. LOHMANN AND J. FEICHTER, *Global indirect aerosol effects: a review*; Atmos. Chem. Phys., 2005, **5**, 715-737.
- [7] T. BAYNARD ET AL., *Key factors influencing the relative humidity dependence of aerosol light scattering*; Geophys. Res. Lett., 2006, **33**(6), 560-560.
- [8] A. S. ACKERMAN ET AL., *Effects of aerosols on cloud albedo: Evaluation of Twomey's parameterization of cloud susceptibility using measurements of ship tracks*; J. Atmos. Sci., 2000, **57**, 2684-2695.
- [9] A. R. RAVISHANKARA, *Heterogeneous and Multiphase Chemistry in the Troposphere*; Science, 1997, **276**(5315), 1058-1065.
- [10] F. KARAGULIAN, *The heterogeneous chemical kinetics of N<sub>2</sub>O<sub>5</sub> on CaCO<sub>3</sub> and other atmospheric mineral dust surrogates*; Atmos. Chem. Phys. Discuss., 2005, **5**, 10369-10408.
- [11] C. I. DAVIDSON, *Airborne particulate matter and human health: A review*; Aerosol Sci. Technol. **39**(8), 737-749.
- [12] J. HAYWOOD AND O. BOUCHER, *Estimates of the direct and indirect radiative forcing due to tropospheric aerosols: A review*; Rev. Geophys., 2000, **38**(4), 513-543.
- [13] L. SLADE AND H. LEVINE, *Beyond Water Activity-Recent Advances Based on an Alternative Approach to the Assessment of Food Quality and Safety*; Crit. Rev. Food Sci. Nutr., 1991, **30**(2-3), 115-360.
- [14] P. G. DEBENEDETTI AND F. H. STILLINGER, *Supercooled liquids and the glass transition*; Nature, 2001, **410**(6825), 259-267.
- [15] C. A. ANGELL, *Liquid fragility and the glass transition in water and aqueous solutions*; Chem. Rev., 2002, **102**(8), 2627-2649.

- [16] C. MARCOLLI, *Internal mixing of the organic aerosol by gas phase diffusion of semivolatile organic compounds*; Atmos. Chem. Phys. Discuss., 2004, **4**, 5789–5806.
- [17] R. E. MARSHAK, *Effect of radiation on shock wave behavior*; Phys. Fluids, 1958, **1**(1), 24–29.
- [18] C. A. ANGELL, *Formation of Glasses from Liquids and Biopolymers*; Science, 1995, **267**(5206), 1924–1935.
- [19] P. J. FOX ET AL., *A reliable, compact, and low-cost Michelson wavemeter for laser wavelength measurement*; Am. J. Phys., 1999, **67**(7), 624.
- [20] S. KRAFT ET AL., *Rubidium spectroscopy at 778-780 nm with a distributed feedback laser diode*; Laser Phys. Lett., 2005, **2**(2), 71-76.
- [21] P. W. ATKINS, *Physikalische Chemie*; Wiley company, 1996, p. 70.
- [22] D. A. MCQUARRIE, *Statistical Thermodynamics*; Harper & Row company, 1973.
- [23] G. JURA AND K. S. PITZER, *The specific heat of small particles at low temperatures*; J. Am. Chem. Soc., 1952, **74**(23), 6030-6032.
- [24] G. MIE, *Contributions to the optics of diffuse media, especially colloid metal solutions*; Ann. Phys., 1908, **25**, 377-445.
- [25] H. C. VAN DE HULST, *Light Scattering by Small Particles*; Dover Publications, 1981.
- [26] P. W. BARBER, S. C. HILL, *Light scattering by particles*; Computational Methods, World Scientific, 1990.
- [27] H. VORTISCH, *Beobachtung von Phasenübergängen in einzeln levitierten Schwefelsäuretröpfchen mittels Raman-Spektroskopie und elastischer Lichtstreuung*; Dissertation, Freie Universität Berlin, 2002, chapter 2.
- [28] W. PAUL, *Electromagnetic traps for charged and neutral particles*; Rev. Mod. Phys., 1990, **62**, 531–540.
- [29] E. J. DAVIS, *A history of single aerosol particle levitation*; Aerosol Science and Technology, 1997, **26**, 212-254.
- [30] E. J. DAVIS AND G. SCHWEIGER, *The Airborne Microparticle: Its Physics, Chemistry, Optics and Transport Phenomena*; Springer Verlag, 2002, chapter 2.
- [31] C. A. COLBERG, *Experimente an levitierten  $H_2SO_4/NH_3/H_2O$ -Aerosolteilchen: Atmosphärische Relevanz von Letovizit*; Dissertation, Eidgenössische Technische Hochschule Zürich, 2001, chapter 3.
- [32] W. PAUL AND M. RAETHER, *Das elektrische Massensfilter*; Zeitschrift für Physik, 1955, **140**, 262-273.
- [33] S. L. GLEGG AND P. BRIMBLECOMBE, *Application of a multicomponent thermodynamic model to activities and thermal properties of 0-40 mol kg<sup>-1</sup> aqueous*

- sulfuric acid from less than 200 K to 328 K*; Journal of Chemical and Engineering Data, 1995, **40**, 43-64.
- [34] T. KOOP ET AL., *Phase transitions of sea-salt/water mixtures at low temperatures: Implications for ozone chemistry in the polar marine boundary layer*; J. Geophys. Res., 2000a, **105**, pp. 26393-26402.
- [35] M. D. COHEN ET AL., *Studies of concentrated electrolyte solutions using the electrodynamic balance. 1. Water activities for single-electrolyte solutions*; J. Phys. Chem., 1987, **91**(17), pp. 4563-4574.
- [36] C. B. RICHARDSON AND T. D. SNYDER, *A study of 24 heterogeneous nucleation in aqueous solutions*; Langmuir, 1994, **10**, pp. 2462-2465.
- [37] I. N. TANG AND H. R. MUNKELWITZ, *Water activities, densities, and refractive indices of aqueous sulfates and sodium-nitrate droplets of atmospheric importance*; J. Geophys. Res., 1994, **99**, pp. 18801-18808.
- [38] L. GREENSPAN, *Humidity fixed points of binary saturated aqueous solutions*; J. Res. Nat. Bur. Stand. (U.S.), 1977, **81**, pp. 89-96.
- [39] J. DESARNAUD, 'Us patent no.: 6450026'.
- [40] C. HAAS, 'European patent no.: 1411349'.
- [41] C. B. RICHARDSON, *A Stabilizer for Single Microscopic Particles in a Quadrupole Trap*; Rev. Sci. Instrum., 1990, **61**(4), 1334-1335.
- [42] A. K. RAY ET AL., *Precision of light scattering techniques for measuring optical parameters of microspheres*; Applied Optics, 1991, **30**(27), 3974-3983.
- [43] C. BRAUN AND U. K. KRIEGER, *Two dimensional angular light scattering in aqueous NaCl single aerosol particles during deliquescence and efflorescence*; Opt. Express, 2001, **8**(6), 314-321.
- [44] U. K. KRIEGER AND A. A. ZARDINI, *Using dynamic light scattering to characterize mixed phase single particles levitated in a quasi-electrostatic balance*; Faraday Discuss., 2008, **137**, 377-388.
- [45] U. K. KRIEGER AND C. BRAUN, *Light-scattering intensity fluctuations in single aerosol particles during deliquescence*; J. Quant. Spectrosc. Radiat. Transfer, 2001, **70**(4-6), 545-554.
- [46] A. A. ZARDINI, U. K. KRIEGER AND C. MARCOLLI, *White light Mie resonance spectroscopy used to measure very low vapor pressures of substances in aqueous solution aerosol particles*; Opt. Express, 2006, **14**(15), 6951-6962.
- [47] A. K. RAY ET AL., *Precision of Light-Scattering Techniques for Measuring Optical-Parameters of Microspheres*; Appl. Opt., 1991, **30**(27), 3974-3983.
- [48] A. MICHELSON AND E. MORLEY, *On the Relative Motion of the Earth and the Luminiferous Ether*; American Journal of Science, 1887, 333-345.
- [49] W. DEMTRÖDER, *Laser Spectroscopy, Volume 1: Basic Principles*; Springer Verlag, 4th edition, 2008, chapter 4.

- [50] J. A. STONE ET AL., *Advice from the CCL on the use of unstabilized lasers as standards of wavelength: the helium-neon laser at 633 nm*; Metrologia, 2009, **49**, 11-18.
- [51] D. A. STECK, *Rubidium 85 D Line Data*: <http://steck.us/alkalidata/rubidium85numbers.pdf>.
- [52] D. A. STECK, *Rubidium 87 D Line Data*: <http://steck.us/alkalidata/rubidium87numbers.pdf>.
- [53] C. ROOS, *Hochauflösende Spektroskopie mit einem Diodenlaser. Versuchsanleitung zum FP2-Praktikum*; <http://heart-c704.uibk.ac.at/LV/F-Praktikum2/Vers119.pdf>.
- [54] ASIT K. RAY AND R. NANDAKUMAR, *Simultaneous determination of size and wavelength-dependent refractive indices of thin-layered droplets from optical resonances*; Applied Optics, 1995, **34**(33), 7759-7770.
- [55] D. M. MURPHY AND T. KOOP, *Review of the vapour pressures of ice and supercooled water for atmospheric applications*; Q. J. R. Meteorol. Soc., 2005, **131**(608), 1539–1565.
- [56] K.-J. ROSENBRUCH ET AL., *Die Temperaturabhängigkeit der Brechzahl von wässrigen Saccharoselösungen*; PTB Mitteilungen, 1975, **85**, 458-465.
- [57] P. CHÝLEK, *Partial wave resonances and ripple structure in Mie normalized extinction cross section*; J. Opt. Soc. Am., 1976, **663**, 285-287.
- [58] U. K. KRIEGER, *Private discussion with Ulrich Karl Krieger*; Institute for Atmospheric and Climate Science, ETH Zürich
- [59] D. BONES ET AL., *Private discussion with David Bones<sup>a</sup>, Jonathan Reid<sup>a</sup>, Daniel Lienhard<sup>b</sup> and Ulrich Karl Krieger<sup>b</sup>*; <sup>a</sup>School of Chemistry, University of Bristol, Cantock's Close BS8 1TS Bristol, U.K.; <sup>b</sup>Institute for Atmospheric and Climate Science, ETH Zürich, Zürich, Switzerland